Fragmentation dynamics and geometrical arrangement of diatomic molecular clusters

Vishant Kumar

To cite this version:

Vishant Kumar. Fragmentation dynamics and geometrical arrangement of diatomic molecular clusters. Physics [physics]. Normandie Université, 2019. English. NNT : 2019NORMC245 . tel-02499706

HAL Id: tel-02499706
https://theses.hal.science/tel-02499706

Submitted on 5 Mar 2020

Normandie Université

THÈSE

Pour obtenir le diplôme de doctorat

Spécialité PHYSIQUE

Préparée au sein de l'Université de Caen Normandie

Fragmentation dynamics and geometrical arrangement of diatomic molecular clusters

Présentée et soutenue par
Vishant KUMAR

Thèse soutenue publiquement le 10/12/2019
devant le jury composé de

M. ALAIN DUBOIS	Professeur des universités, Université Paris 6 Pierre et Marie Curie	Rapporteur du jury
Mme WANIA WOLFF	Professeur associé, Université fédérale de Rio de Janeiro	Rapporteur du jury
M. JIMMY RANGAMA	Chargé de recherche au CNRS, 14 GANIL de CAEN	Membre du jury

Thèse dirigée par AMINE CASSIMI, Centre de recherche sur les ions, les matériaux et la photonique (Caen)

UNIVERSITÉ
CAEN
NORMANDIE

ED 591 PSIME

CiMap

Normandie Université

THESE

Pour obtenir le diplôme de doctorat

Spécialité Physique

Préparée au sein de l'Université de Caen Normandie

Fragmentation dynamics and geometrical arrangement of diatomic molecular clusters

Présentée et soutenue par
Vishant KUMAR

Thèse soutenue publiquement le XX Décembre 2019 devant le jury composé de		
M. Alain DUBOIS	Professeur des Universités, UPMC, Paris	Rapporteur
Mme. Wania WOLFF	Professeur des Universités, UFRJ, Rio de Janeiro, Brasil	Rapporteur
M. Amine CASSIMI	Ingénieur de recherche, CEA, CIMAP, Caen	Directeur de thèse
M. Jimmy RANGAMA	Chargée de recherche, CNRS, CIMAP, Caen	Membre du jury

Thèse dirigée par Amine CASSIMI, Centre de recherche sur les ions, les matériaux et la photonique (Caen)

UNIVERSITÉ
CAEN
NORMANDIE

Contents

Introduction

1

Atomics and molecular physics generates a fundamental knowledge base for our understanding in disciplines, such as atmospheric, environmental, chemical, biomedical and even astrophysical sciences. However, it also improves our quality of life by providing for example the primary inputs necessary for developing new instrumentation and techniques for medical applications, such as computer tomography, magnetic resonance imaging, positron emission tomography, laser induced surgeries and radiation therapy for cancer treatments etc. Today, many groups around the world study gas phase biomolecular fragmentation induced by ion collision with the aim to provide an exhaustive data base for radiobiology and hadrontherapy. However, these molecules being in the gas phase is a slight concern for biologists as the role of the environment of target molecules on its fragmentation is known to be of major importance.

Over the years, the "Atoms, Molecules and Clustesr" group in CIMAP has been studying various collisional systems ranging from atoms to large molecules and clusters. Thanks to the variable range of projectiles in GANIL, our group have not only studied the primary collision processes but also the relaxation mechanisms of the target after the collision. In the recent studies the rare gas dimers in collision with three different projectiles it has been found that due to the large interatomic bond length a dimer can be considered in a first approximation as a two independent atoms during the collision. Due to very low electron mobility inside such van der Waals dimers, two specific relaxation mechanisms (Radiative charge transfer and interatomic coulombic decay) have been identified which differs drastically from the case of covalent molecules where fast electron rearrangement usually takes place before fragmentation. In a next step, increasing the complexity of the target intermediately from atomic dimers to diatomic molecular dimers or trimers will open up the possibilities to answer various questions regarding the fragmentation dynamics and geometry of such systems. As the diatomic molecular cluster consist of both van der Waals and covalent bonds, it is interesting to compare the molecular fragmentation inside the dimer with the one of an isolated molecule. Such systems offer an unique tool to investigate the transition from gas phase molecules to the condensed phase.

In this context, this thesis is devoted to an experimental study of small clusters of nitrogen (N_2) and carbon monoxide (CO) molecules. In the last decade, there had been a lot of ab-initio calculations along with several infrared spectroscopic measurement done to speculate the three dimensional geometry of such diatomic molecular clusters. Even with the constant advancement in the computational and experimental methods no definitive conclusion had been provided so far leaving it as an open question for the investigation.

The experiments presented in this thesis concern collision between low energy multiply charged projectiles and diatomic molecular clusters (dimers and trimers). Clusters of two different targets N_2 and CO were used during the experiment with an 135 q.keV Ar^{9+} projectile ions. Such highly charged ions are used to produce multiple ionized targets which then undergoes dissociation due to charge repulsion. The recording of the products from the collision system (recoil ions from the target and the scattered projectile) is ensured by a Cold Target Recoil Ion Momentum Spectroscopy (COLTRIMS) setup. The coincident detection of all fragments generated by Coulomb explosion of a multiply charged target allows the reconstruction of the three dimensional momentum vectors of each fragment. Using these momentum vectors we can indirectly deduce the initial structure of the neutral cluster. The experimental results are then compared to a Monte-Carlo based numerical simulation which computes the trajectories of three repulsing ionic fragments. Unlike rare gas dimers, the molecular dimers comprises of two different types of bond which upon cleavage can be used to investigate different fragmentation pathways. In our analysis we have thoroughly analyzed 2 and 3-body fragmentation channels from $(N_2)_2^{n+}$ and $(CO)_2^{n+}$, where $n \geq 2$. The 2-body fragmentation channel is due to cleavage of van der Waals bond only and is used to deduce the intermolecular separation in dimers. Additionally, the 3-body fragmentation channels are used for investigating the dynamics of fragmentation of a molecule in a controlled environment and different fragmentation pathways upon the cleavage of both van der Waals and covalent bond inside a dimer.

This thesis is organized as follows. The second chapter is a bibliographic summary including a general description of molecules and clusters and focusing on the geometry of N_2 and CO dimers. Then an introduction about the collision of the low energy multiply charged projectile with the dimer is presented within the framework of the Classical Over-the-Barrier Model and showing the importance of multiple electron capture in such collisional systems. A description of the Coulomb Explosion Imaging Technique is also given at the end of this section.

The third chapter consists of a presentation of the experimental setup used to perform this work. It encapsulated the features of the momentum spectrometer and description of the time of flight and position measurements of the fragments. Another part of this chapter comprises a description of the supersonic gas jet target and projectile ion beam used in this experiment. At the end, a detailed discussion about the energy calibration methods used for kinetic energy release measurements for both $(N_2)_2^{2+}$ and $(CO)_2^{2+}$ is given.

Chapter four, five and six expose all the results obtained during this work, concerning respectively the fragmentation dynamics of the N_2 and CO dimers, the three dimensional structure of these dimers and the geometry of N_2 and CO trimers.

Finally, the conclusion summarizes the work done in this thesis and presents a discussion on its relevance and future directions.

Context

2

Contents

Collisions involving ions, molecules or clusters play a key role in various gaseous and plasma environments. The study of such collisions is required for fundamental understanding and have applications in fields of astrophysics, planetary atmosphere [1], biological matter and medical treatments [2], thermonuclear fusions [3] and semiconductor industry. Ion collisions have also been studied to compare the fundamental processes from the gaseous phase to the condensed phase of atomic or molecular targets. Since the early 30's, the properties of various rare gas clusters and their relative comparison with the diatomic molecules in fundamental aspects has been investigated [4]. Since then the study of the van der Waals complexes has became an interesting tool to enhance knowledge of intermolecular potentials and therefore provides further insight in the specific properties of clusters, geometry of these complexes and their fragmentation dynamics [5–16].

The collision between an ion and a molecular target is more complex in comparison to an atomic target, due to the presence of the more degrees of freedom (vibration and rotation of the molecule) in the former system and also due to the dependence of the collision process with the orientation of the molecule with respect to the ion beam. Very recently, the multiple electron capture probability as a function of the impact parameter in the case of two rare gas dimers have been studied with a Monte-Carlo based classical over the barrier model [17]. A brief introduction of this model and its relevance with our target system will be discussed in later in this chapter.

Finally, the investigations of atomic and molecular clusters have grown enormously and become possible especially with the spectacular developments and advancement in the spectroscopic techniques as well as computational methods. Among the state-of-the-art experimental methods, Coulomb explosion imaging technique allows to investigate the initial structure of the molecules and clusters as well as the relaxation mechanisms leading to the fragmentation thanks to the coincident detection of all emitted particles.

A brief review of the existing data about the geometry of N_2 and CO dimers using various theoretical and experimental methods is presented in this chapter. In addition, a compilation of the work done on the molecular fragmentation using Coulomb explosion imaging technique is also discussed at the end of this chapter.

2.1 Structure of molecular clusters

The history of atomic and molecular clusters dates back to very early times in 1930's [4]. These clusters serve as a bridge between the independent study of atoms or molecules in gas phase to the condensed phase. This thesis is devoted to the study of molecular dimers and trimers. Such systems are composed of two or three covalently bound molecules (N_2 or CO in our case) which are weakly interacting thanks to the van der Waals forces.

Chemical systems such as molecules or clusters are held together by different types of forces and only the valence electrons (electron from the outermost shell) take part in the binding process. Several types of bonding exist depending on the nature and the electronic structure of the constitutive atoms. They are classified in four categories: the covalent bond, the ionic bond, the van der Waals bond and the hydrogen bond. In the following, we will describe only the covalent and van der Waals bonds as well as the structure of the N_2 or CO dimers.

2.1.1 Covalent bonds

The covalent bond is based on a sharing of the valence electrons of two atoms. Several bonds can be formed between the two centers depending on the number of valence electrons of each atom. Such molecules are best explained by the Molecular Orbital (MO) theory which can estimate the energies of the electrons in a molecule along with the probable location of these electrons. Unlike in valence bond theory, MO theory uses the combination of atomic orbitals to yield molecular orbitals which are delocalized over the entire molecule rather than being localized on the corresponding atoms.

For example, the N_2 molecule has three bonds (triple bond) because the nitrogen atom lacks three valence electrons to complete its outer shell. The potential energy curve (PEC) of the ground state of the neutral N_2 is shown in figure 2.1.1 (a). The N_2 molecule has a triple bond leaving one lone pair of electrons. The equilibrium bond length (R) of N_2 molecule is 1.1 Å and its bond dissociation energy (BDE) is about 9.8 eV. Being homonuclear this molecule has no permanent dipole moment.

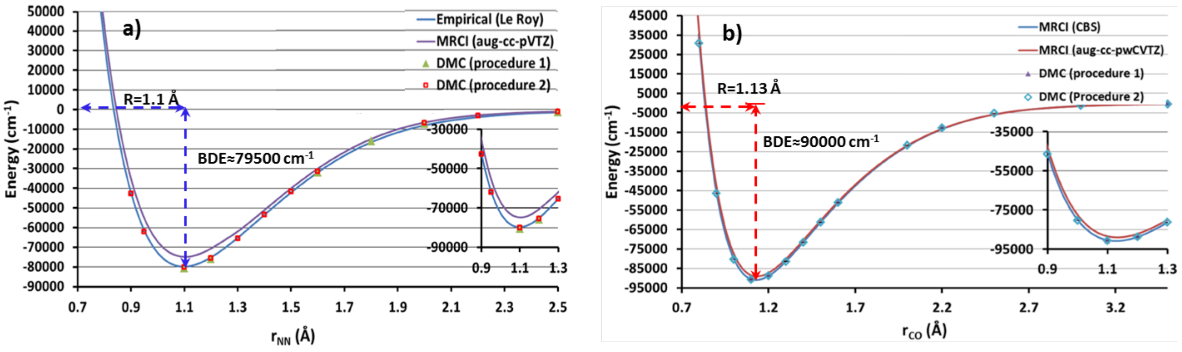

Figure 2.1.1 : *Potential energy curves of the ground state of N_2 and CO molecules [18]. (1eV = 8100 cm^{-1})*

Usually each atom provides one electron for a single covalent bond, however it is not true necessarily. If one of the atom is more electronegative in the covalent bond then the electron density is partially shifted towards the more electronegative atom. This generates a polarity making the covalent bond polar as it is the case for CO. Due to this polarity the molecule attains a permanent dipole. CO also has the same number of valence electrons as N_2. It also makes a triple bond with one lone pair of electrons. However, the one pair of shared electrons are provided from the oxygen atom. Oxygen being more electronegative the electron density is shifted towards it causing a permanent dipole moment of 0.11 D. The PEC curve of the ground state of CO is shown in figure 2.1.1 (b) showing the bond length of about 1.13 Å with a BDE of 14.5 eV making it the strongest bond in neutral molecules.

2.1.2 van der Waals bonds

In rare gas dimers the MO theory predicts that there is no possibility of covalent bonds between the atoms because they have a full outer shell of valence electrons. The binding is then only possible via van der Waals bond. Due to its polarizability, an atom or molecule may have a permanent or induced electrostatic dipole moment (μ). In presence of another atom or molecule, a dipole-dipole attraction may create a weak bond between the two atoms or molecules. This bond is known as van der Waals bond and is not chemical in nature as there is no participation of electrons although the polarization from the electron cloud.
A dipole-dipole interaction could result from a permanent or induced dipole interaction inside the atoms or molecules. A dipole may interact with its electrostatic environment, including other dipoles, and the strength of these interactions depends directly the nature of the neighbor. As we can see in the figure 2.1.2 the arrangement of dipole due to presence of another dipole.

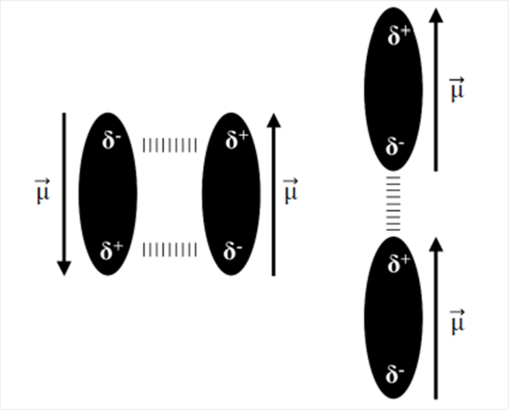

Figure 2.1.2 : *Alignment of dipole due to the presence of the other dipole in vicinity. On the left is an anti parallel configuration and on the right is a co-linear configuration.*

In the case of rare gas dimers, the bonding results from an induced dipole interaction as the atoms do not have a permanent dipole moment. Figure 2.1.3b shows the comparison between the absolute bond strength and bond length of all the rare gas dimers [19]. The van der Waals bonds have a much smaller binding energy and longer bond length than covalent bonds. Typical binding energies are about 10 meV and bond length are 3 or 4 Å. Due to its low binding energy, the van der Waals bond can exist wherever there is no possibility of other bond formation. An example of comparison between bond strength of covalently bonded N_2 and van der Waals bonded $(N_2)_2$ is shown in the figure 2.1.3a [18, 20]. The covalent bond is upto 650 times more stable as the van der Waals bond and the repulsive bond length differs by a factor of about 4.

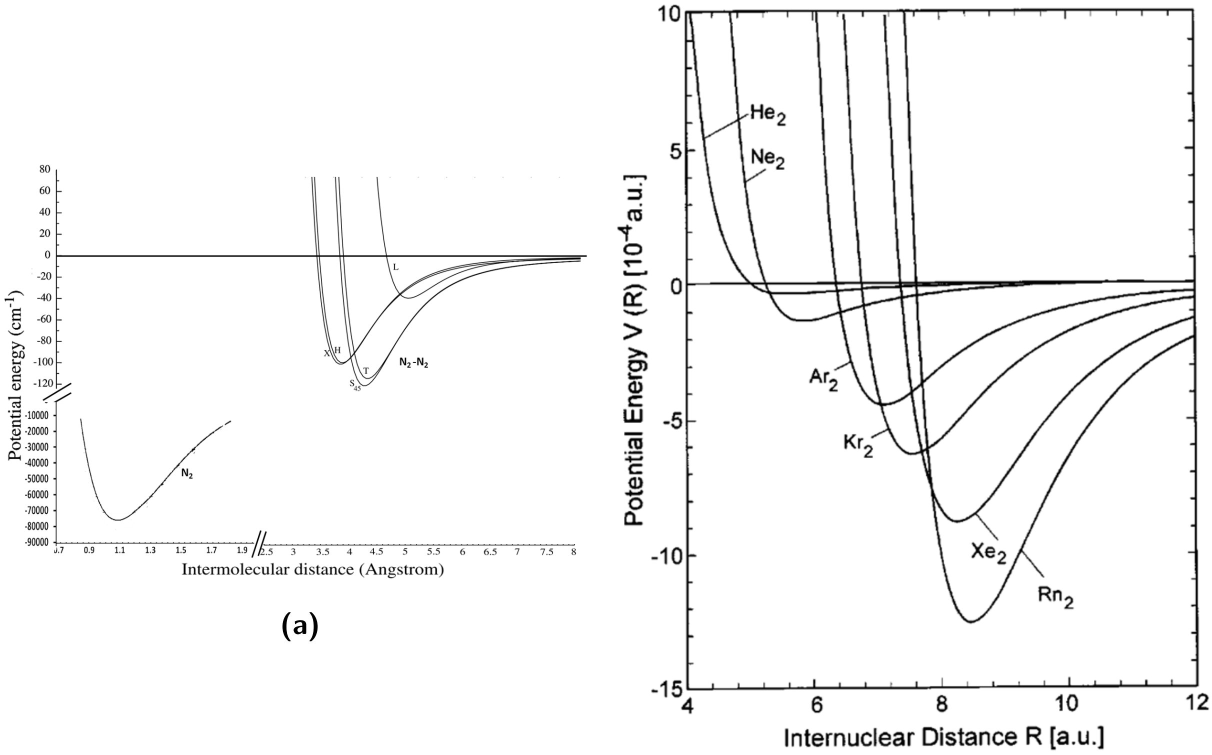

(a)

(b)

Figure 2.1.3 : *a)A comparison of potential energy curves of covalent bond between $N - N$ inside N_2 molecule and the van der Waals bond between $N_2 - N_2$ inside the $(N_2)_2$ dimer. In this case the covalent bond is upto 650 times stable than its van der Waals bond. The diagram has been modified using the work of Powell in [18] and Gomez in [20] to give an qualitative comparison between the strength and separation of the two bonds. b) Potential energy curves of all the rare gas dimers [19].*

The general shape of the PEC for the van der Waals bonding can be described by the Lennard-Jones potential which is shown in equation 2.1.1 below:

$$V = \varepsilon\left\{\left(\frac{\sigma}{R}\right)^{12} - 2\left(\frac{\sigma}{R}\right)^{6}\right\} \tag{2.1.1}$$

where ε is the depth of the potential well located at the distance σ and R is the interatomic/intermolecular distance. However, the precise calculation of the potential energy in the molecular dimers is quite complex as it depends on various other factors including the three dimensional geometrical arrangement of the molecules inside the dimer.

2.1.3 Geometry of molecular clusters

One of the main topic of this thesis is the geometry of the N_2 and CO dimers and trimers. There have been many theoretical works done to predict the geometry of these molecular dimers.

2.1.3.1 N_2 dimers

The first studies of the geometry of N_2 dimer are dated back in the early 1970's, where Long et al. used infrared (IR) spectroscopy to comment over the intermolecular distance and its geometry [5]. Earlier, the same team studied the van der Waals complexes of $Ar-N_2, Ar-O_2$ and found that equilibrium geometry is a "T" configuration where the N_2 (or O_2) molecule is oriented perpendicular to the dimer axis (see figure 2.1.5 (d)). The similar conclusion had been made for the N_2 dimer. The infrared spectrum was also used to predict the intermolecular distance and was found to be 3.7 Å. In conclusion from this work they felt the need of new theoretical models for such complexes in order to conclude on the geometry. In another study conducted by Carnavole et al. using the photoelectron spectroscopy of (N_2) dimer [21], the author suggested an "X" shaped (see figure 2.1.5 (b)) configuration with a dimer bond length of 3.8 Å.

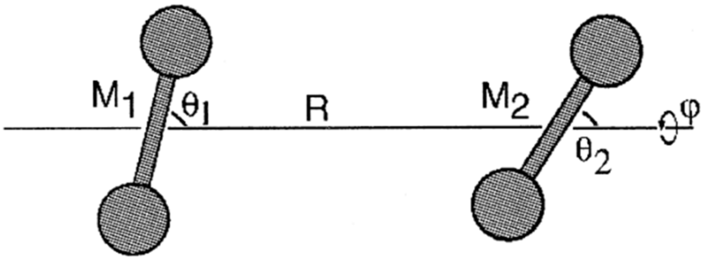

Figure 2.1.4 : *General representation for a dimer of two diatomic molecules [22]. R is the distance between the center of mass of the two monomers M_1 and M_2. θ_1 and θ_2 are the angles between the molecular axis of M_1 or M_2 and the dimer axis. ϕ is the dihedral angle between the two monomers M_1 and M_2.*

Since then there have been several works on the geometry of (N_2) dimer [20,22–27], which predict five possible three dimensional geometries. These three dimentional structures can be described using the "internal" parameters ($(R, \theta_1, \theta_2, \phi)$, see figure 2.1.4) introduced in [22]. Several ab-inito calculations were performed in order to determine the global minimum of the potential energy surface of the neutral N_2 dimer [23,24]. A summary of the different predicted structures is shown in figure 2.1.5. For "H" and "X" geometries the intermolecular distance is in the range of 3.6-3.8 Å, for "Z" and "T" shapes this distance varies between 4-4.1 Å and the linear "L" configuration is always predicted above 4.3 Å. However, the "Z" and "T" configurations are found to be the most stable in most of the calculations [20,22,25–27].

Figure 2.1.6 shows the PEC's for all the five possible geometries studied in the work of Gomez et al. [20]. On the basis of intermolecular distance there are three main configurations where, "H" and "X" are centered around 3.6 Å, "T" and "Z" are around 4 Å and "L" is at 4.6 Å. As the predicted difference between the intermolecular distances of the "H" and "X" shapes is very low, therefore it will be necessary to access the torsional angle ϕ in order to distinguish between the two configurations ("H" corresponds to ϕ=0° and "X" corresponds to ϕ=90°).

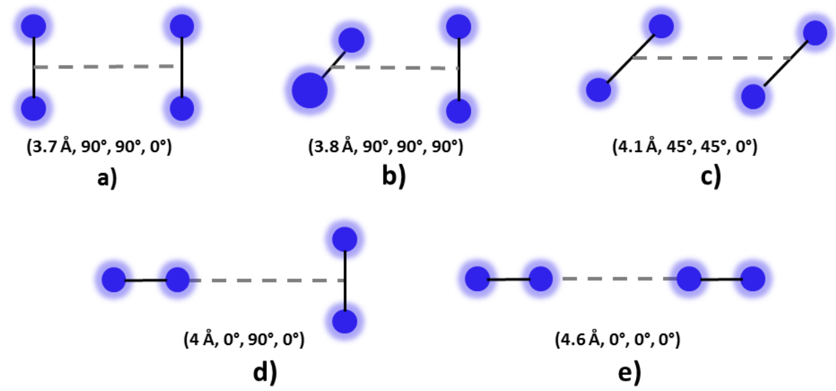

Figure 2.1.5 : *Summary of the five structures of* (N_2) *dimers predicted in various theoretical studies [20, 22–27]. a)Planar "H" shaped, b) non planar "X" shaped, c) canted parallel "Z" shaped, d) "T" shaped and e) linear "L" shaped. The corresponding "internal" coordinates are indicated in brackets.*

Contrarily, the "T" and "Z" configurations differs from their (θ_1,θ_2) angles and are expected to be more easily distinguished in our experiments. These predicted geometries will be used as reference and compared to our experimental results in the Chapter 5.

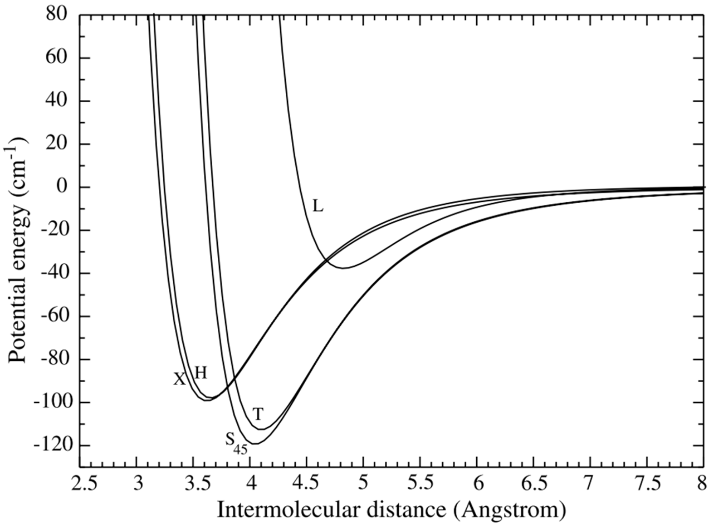

Figure 2.1.6 : *Potential energy curves of* $(N_2)_2$ *dimer calculated in [20] for all the five predicted geometrical configurations.*

2.1.3.2 CO dimers

The carbon monoxide being an heteronuclear molecule, CO dimer makes itself a good target to be studied with IR spectroscopy. The three dimensional geometry of CO dimers is also described using the "internal" parameter as introduced for N_2 dimers. However, a geometry where the carbon atoms of the each molecule are oriented toward the center of the dimer is now called "C-bonded" (For eg. θ_1=135° ,θ_2=45°). Similarly, a "O-bonded" geometry correspond to the case of two "inner" oriented oxygen atoms (For eg. θ_1=45° ,θ_2=135°). In last two decades, there have been several IR spectroscopic measurements [28–31] done to determine the geometry of the CO dimer. In the work by Brookes et al. the CO dimer IR spectrum in the 2139-2152 cm^{-1} region has been studied, showing the presence of two possible different overlapping isomers of CO dimer. The author suggested two different configurations both corresponding to the "T" shape, C-bonded and O-bonded with intermolecular distance of 4.4 Å and 4 Å(see figure 2.1.7 (c) and (d)). However, not so later in 2003 Surin et al. [32] observed the millimeter wave spectrum and still could not differentiate between the two isomers due to the low energy difference between them. Another group from South Africa used a Fourier transform interferometer to record the IR spectrum of CO dimers trapped in nitrogen and argon [29,30]. In parallel they have also performed theoretical calculation for five distinct possible structures, shown in figure 2.1.7. From the agreement between experimental and calculated dimer-monomer wave number shifts they highly suggest an "T" shaped O-bonded configuration with intermolecular separation of around 4 Å. Although, due to very small energy difference in the minima of various configuration in potential energy surface (PES), they suggest not to completely excluded the C-bonded isomer with separation around 4.4 Å. In another work done very recently by Rezaei et al., the existence of the slipped anti-parallel configurations have been reported [31].

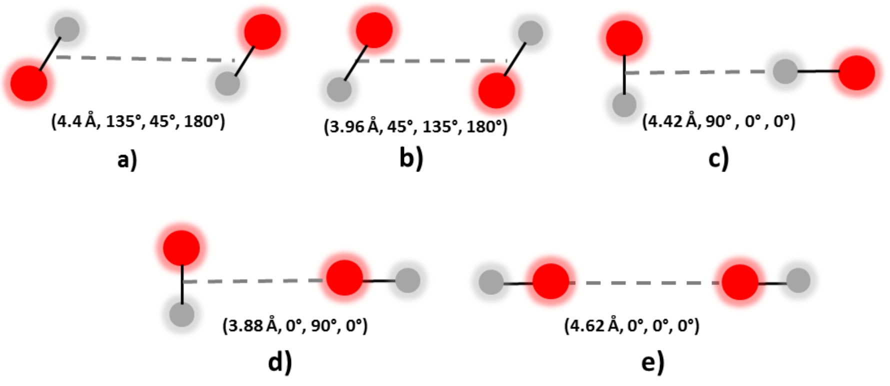

Figure 2.1.7 : *Representation of all the possible geometries predicted using the IR or millimeter wave spectroscopy and PES calculations in [14, 28–35]. Five most favorable geometries are a) slipped anti-parallel C-bonded b) slipped anti-parallel O-bonded c) "T" shaped C-bonded d) "T" shaped O-bonded and finally e) O-bonded linear shaped.*

Over the time the need of much accurate PES for CO dimer became of high importance. In parallel to all the IR and millimeter wave spectroscopy, the advancement in the PES and rovibrational calculations were reported by various groups [14, 32, 33]. Up to the begining of

2000, the calculation conclude to the existance of both C and O-bonded, slipped anti-parallel and "T" shaped isomers. But the confirmation of a slipped anti-parallel configuration became more evident with the most recent PES calculations in [34, 35]. In contrast, the two most favorable predictions for geometry of CO dimer are: a C-bonded antiparallel geometry with $\theta_1 \approx 135°$, $\theta_2 \approx 45°$ and bond length R= 4.4 Å, and an O-bonded antiparallel geometry with $\theta_1 \approx 45°$, $\theta_2 \approx 135°$ and a bond length of R= 4 Å.

For both the N_2 and CO dimers a detailed comparison of proposed geometries and the experimental data using a numerical simulation is explained in chapter 5.

2.2 Collision with Low Energy Highly Charged Ion (LE-HCI)

In the past, atomic and molecular complexes have been studied experimentally using various ionisation or excitation processes: photoionization using synchrotron radiation [36–38], electron [39–43], laser [44–46] and multiply charged ion beams [47–58]. In this thesis we will only focus on the ion-molecule/cluster collision leading to charge and energy exchange between the collision partners via three elementary processes: electron capture, excitation and ionization. The importance of these processes depends on the comparison of the projectile velocity (v_p) with the classical orbital velocity of valence electrons (v_e) of the target [48] and also on the collision asymmetry which is the ratio between projectile and target atomic numbers (Z_p/Z_t) [59]. Combined together they give the collision strength parameter $\kappa = (v_e/v_p) \times (Z_t/Z_p)$. If the $\kappa \gg 1$ the electron capture will be the most probable process and for $\kappa \ll 1$ ionization and the excitation dominates. In certain cases where $Z_p \geq Z_t$, these dominant processes can be categorized just by the energy of projectile. In our case for Ar^{9+} at 15 q.keV colliding with N_2 or CO targets, $\kappa \sim 2.7 \gg 1$ implying the electron capture as the most probable process during collision.

The interaction time is another point of interest in the ion induced dissociation of molecular and dimer targets. As we use the Coulomb explosion imaging technique to measure the initial structure of the neutral target, the interaction time has to be much smaller than the nuclear or molecular motion in order to obtain a reliable measurement. As an example, it has been shown that using too long laser pulses to measure the geometry of triatomic molecules D_2O results in a deviation from the expected values [60]. Here the time scale of ionization was comparable to the time scale of the molecular dynamics which allows the ions to move from their initial position after ionization and causing the deviation. Although, in the case of the low energy ion collisions (few tens of keV range) the ionization time is less than 1 fs. For example in our case, we use Ar^{9+} with a velocity of 8 Å/fs (0.37 a.u.), the target dimer bond length is of around 4 Å and the capture radius for first valence electron of N_2 is about 7 Å (13 a.u.). This gives an interaction time of about $\frac{7+4}{8}$= 1.4 fs in the worst case possible. This value is much shorter than the time scale of molecular vibration (10 fs) and rotation (1 ps) [47]. Due to this time difference, the nuclear motion is considered as frozen during the collision leading to excitation through vertical transition in the Frank Condon region (see figure 2.2.1) and validate our approach using Coulomb explosion imaging technique.

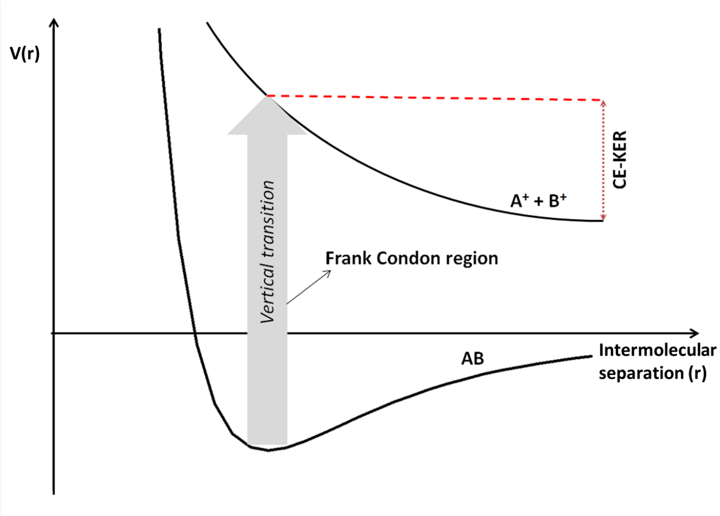

Figure 2.2.1 : *Schematic representation of the transition from the initial ground state to a dissociative state of the ionized and/or excited dimer and then its dissociation into two ionic fragments. The vertical transition due to the collision takes place in the Franck Condon region.*

For many years, theoretical and experimental investigations of collision mechanisms involving ionic projectiles and neutral gas phase targets (atom, molecule or clusters) have became of prime importance. In the case of molecule and cluster as targets, there is a huge dependency of bond type of the target on the primary and relaxation mechanisms. In case of a diatomic covalent molecule in collision with the ionic projectile, the total charges of the transient molecular ions are generally shared among the dissociating atomic fragments [61]. This is due to the delocalization of the valence electrons through out the molecule. On the other hand for a van der Waals dimer for example Ar_2, this rearrangement of charge is weak due to the long interatomic distance. In addition a highly sensitive orientation dependence has been found in this Ar_2 dimer for asymmetric channels [53, 54]. In a previous thesis in our group, it was found that for asymmetric fragmentation channels, due to low charge mobility between the two atomic sites of dimer, the projectile is scattered in the direction of the most charged fragment [55]. This indicates that the projectile mainly capture electron to the atom closest to its trajectory. Furthermore, new relaxation mechanisms were also observed in comparison to covalent molecules due to the asymmetric distribution of charges in a dimer: Radiative Charge Transfer (RCT) and Interatomic Coulombic Decay (ICD) [53, 56]. These mechanisms involve either the electron transfer or the energy transfer to the neighbour neutral atom from the ionized atom. For further investigation of the electron capture mechanism a theoretical approach has been designed which is detailed in the section below [17].

2.2.1 Electron capture in dimers

For a case of low energy ion (400 eV/amu≈ 0.13 a.u.) atom collision, the first Classical Over-the-Barrier Model (COBM) was developed by several groups based on the idea that the electrons can transfer from target to projectile at a given internuclear distance [62–65]. At this distance the potential barrier between the two nuclei is lower than the Stark shifted binding energy of the transit electrons. After the successful agreement in case of low energy ion atom collisions, a similar approach is used for molecular targets. A three center COBM has been developed to understand the asymmetric charge distribution in Coulomb explosion of N_2 with upto 100 eV/amu Kr^{8+} ions [66]. A similar approach was later used to update this model for rare gas dimers which is one of the basis of the COBM approach used in [67]. In this approach to perform a complete treatment of collision, the model was divided into two steps, the way-in and the way-out. This was one of the adaption from the model of Niehaus for atomic targets [65]. Additionally, a Monte Carlo approach is used to account for the different orientations of the dimer and impact parameters and aid the comparison between simulation and experimental data.

In this model, the projectile approaches slowly the target and the potential barrier of the target is lowered by the proximity of the incoming highly charged projectile ion. This leads to the creation of quasi-molecular state, where projectile and target are sharing electrons. In this quasi-molecular state, the electrons can move from the target to the projectile. In the way-out (when the projectile is getting away from the target) the electron can be captured by the projectile or go back to the target. The probability of capturing depends on the impact parameter, the projectile charge state and ionization energies of the target.

In figure 2.2.2, a schematic of an ion-atom collision is shown as described in this model. In 2.2.2 (a) a projectile A^{q+} with a charge state of $q+$ is approaching the neutral target atom B, at different instances the internuclear distance between the two is presented as R_i^{in} (for way-in step) and R_i^{out} (for way-out step). The final state of the projectile is represented as $A^{(q-q')+}$, where q' is the number of electron stripped from the atom at the way-out. Much detailed understanding of this model and its agreement with the experimental results can be found in the corresponding publication [67].

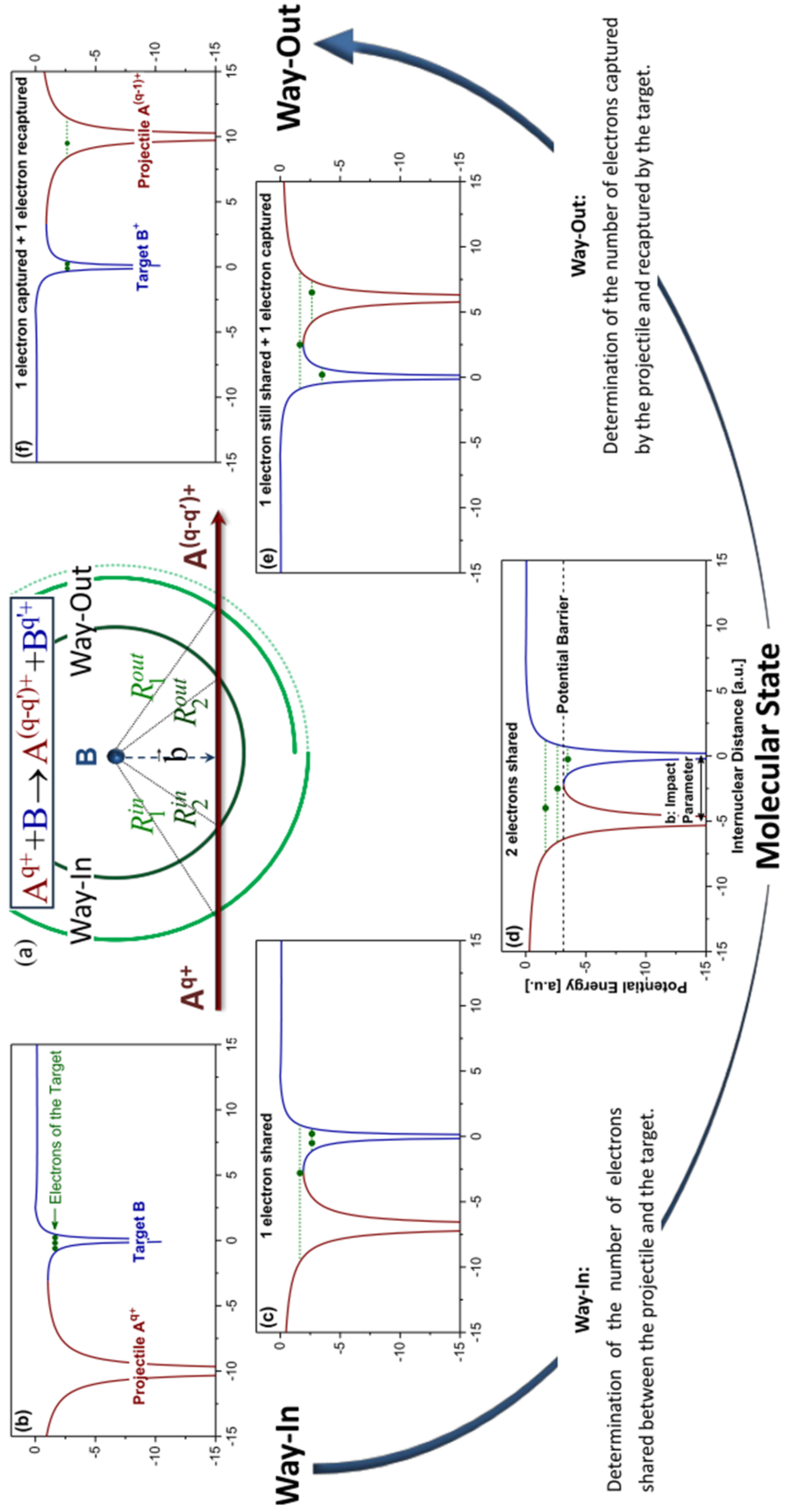

Figure 2.2.2 : *Schematic representation of the ion (A^{q+}) and target atom (B) collision along with the evolution of potential barriers in the way-in and the way-out of the collision [67]. See details in the text.*

Further, this MC-COBM model has been extended to the case of a van der Waals rare gas dimer where the dimer is approximated by two quasi independent atoms. Now the similar approach as in the case of the atomic target can be used with both the atoms separately considering two independent collisions but during which the effective projectile charge state may change because of electron capture on each site of the dimer. Indeed, for highly charged ions the capture radii are larger than the van der Waals bond and electrons can be captured from the two sites of the dimer depending on the impact parameter.

Figure 2.2.3 represents the two steps of collision where step 1) shows the collision between a projectile A^{q+} and a $(M)_2$ dimer. Following electron capture, the system can be represented as: $A^{q+} + (M)_2 \rightarrow A^{(q-(x+y))+} + M^{x+} + M^{y+}$. Once the target is ionized it may relax via fragmentation due to the repulsive Coulomb force acting between the M^{x+} and M^{y+}.

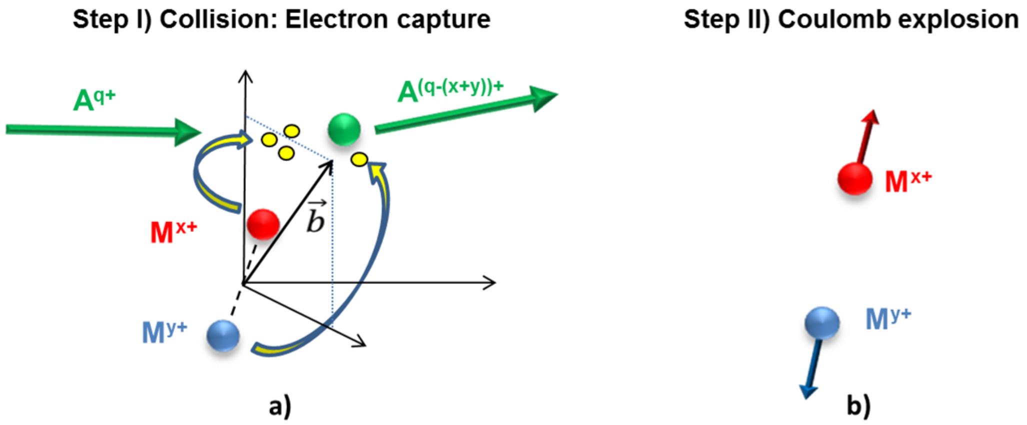

Figure 2.2.3 : *(a): Representation of the collision between a low energy projectile ion (A^{q+}) and a dimer target ($(M)_2$) in a 3-Dimensional Cartesian system,(b): Relaxation of ionized target via fragmentation due to Coulomb explosion.*

Figure 2.2.4 shows the relative intensities of the different fragmentation channel observed in the $Ar^{9+}+Ar_2$ collision system. The MC-COBM (in gray) reproduces the measured yield and validates the hypothesis that the dimer can be in first approximation considered as two independent atoms. In particular, the dominance of asymmetric fragmentation following quadruple electron capture is explained by an higher probability of asymmetric electron capture and by the slow electronic rearrangement between two atomic sites.

The projectile impact parameter has been shown to play a crucial role on the electron capture probabilities from both sites of the dimer. These capture probabilities depend on the ionisation energies and capture radii of the target. Table 2.2.1 shows a comparison between the successive capture radii for Ar atom and for N_2 and CO molecules. Since, the first, second and third ionization potential of both N_2 and CO molecules are very close to that of argon atom, therefore the capture radii for Ar^{9+} projectiles are also found similar for all targets. Note that

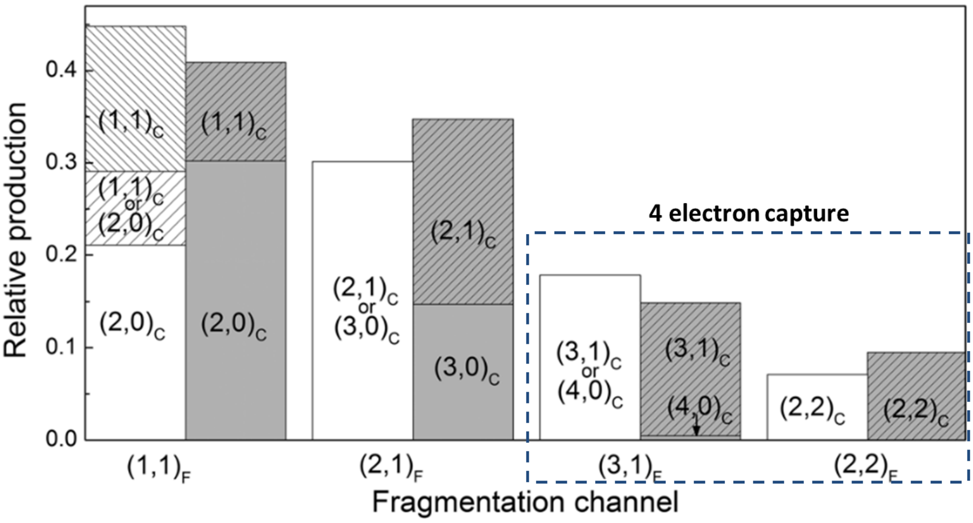

Figure 2.2.4 : *Relative yields for the different electron capture and fragmentation channels (from $Ar^{9+}+Ar_2$ collision system) extracted from the experimental data (white) and results from MC-COBM calculations (gray) [55].*

due to unavailability of third ionization potential for both the N_2 and CO molecules, we have used the third ionization potential of nitrogen atom to have a fair approximation of capture radii.

Table 2.2.1 : *Estimation of the capture radii for one, two or three electrons capture from Ar, N_2 and CO targets using the Ar^{9+} as the projectile. IP_i represents the ionization potential for i^{th} electron and R_i^c is the capture radius for that electron using COBM model.*

Target	IP_1 (eV)	R_1^c (Å)	IP_2 (eV)	R_2^c (Å)	IP_3 (eV)	R_3^c (Å)
Ar	15.8	6.39	27.6	5.46	40.7	4.73
N_2	15.6	6.46	27.2 [68]	5.55	47.4	4.06
CO	14.5	6.95	27 [69]	5.59	-	-

Moreover, the equilibrium intermolecular distance for both N_2 and CO dimer are of the same order of interatomic distance of Ar_2 dimer, which is around 4 Å. As the size of these dimers is smaller than the capture radii for Ar^{9+}, this implies that the multiple electron capture may occur on each site of the molecular dimers. Depending on the number of electrons captured on each molecular site of the dimer, molecular fragmentation may also occur in addition to the cleavage of the weak van der Waals bond. This leads to the existence of various fragmentation channels of the multi-ionized molecular dimers.

2.2.2 Fragmentation pathways

This thesis focuses on ion collision with diatomic molecular clusters (dimer and trimer). Such polyatomic targets comprise both covalent and van der Waals bonds. Until now we have established that multiple electron capture may lead to various fragmentation channels because of the Coulomb repulsion between the monomers. For a collision system:
$A^{q+} + (M)_2 \rightarrow A^{(q-(x+y))+} + M^{x+} + M^{y+}$
where A^{q+} is the projectile ion, M is the diatomic molecule and x, y are the number of electrons captured from each site of the $(M)_2$ dimer. From here several fragmentation channels can be expected depending upon the value of x and y.

Case 1: If both x and y are equal to 1, this corresponds to the case where one electron has been captured on each monomer. Consequently, the dimer fragments via a 2-body channel where two singly charged M^+ ions are emitted. In this case, the $M^+ + M^+$ dissociation follows a pure Coulomb law and the intermolecular bond length can be deduced from the kinetic energy released (see 2.3.1 for more details).

Case 2: If $x \geq 2$ and $y=1$. For a simplest case lets consider $x=2$ and $y=1$, where two electrons are captured from one site/molecule of the dimer. In such a case, a molecular dication is produced inside the dimer. Although this triply ionized dimer may fragment via a 3-body fragmentation channel where both the van der Waals and covalent bond breaks. However, this fragmentation of the molecular dication (covalent bond cleavage) inside the dimer depends on the presence of metastable states in the molecule. For example in the case of N_2^{2+} and CO^{2+} the lifetimes of the electronic states are totally different. The lower excited states of the N_2^{2+} dication are short lived as the density of metastable states is very low. On the other hand, the CO^{2+} dication have abundance of such metastable vibrational states. Figure 2.2.5 (a) shows the potential energy curves of four lowest lying electronic metastable states of CO^{2+}, they are $A^3\Sigma^+$, $b^1\Pi$, $a^1\Sigma^+$ and $X^3\Pi$. The lifetimes of all the metastable states in these four states are depicted in 2.2.5 (b). There are at least more than 70 metastable vibrational states associated to these electronic states having lifetimes longer than 1 ps [70]. Due to the presence of these long lived states the CO^{2+} dication, the dimer trication $(CO)_2^{3+}$, might induce two distinct dissociation mechanisms direct and sequential. Direct fragmentation corresponds to a synchronous cleavage of the van der Waals and covalent bonds and is associated to lifetimes of the dication shorter than 1 ps. Sequential fragmentation refers to the case where the van der Waals bond explodes followed by the cleavage of the covalent bond in the molecular dication because of the presence of the metastable states with lifetimes larger than 1 ps. Finally, if the lifetime are larger than few μs, the experiment will record a 2-body $M^+ + M^{2+}$ channel.

If $x \geq 3$ and $y=1$, this would also result in a 3-body fragmentation channel. However, there will be mostly the participation of pure dissociative states in the fragmentation of the molecular trication. Therefore, sequential fragmentation is not expected to occur in this case.

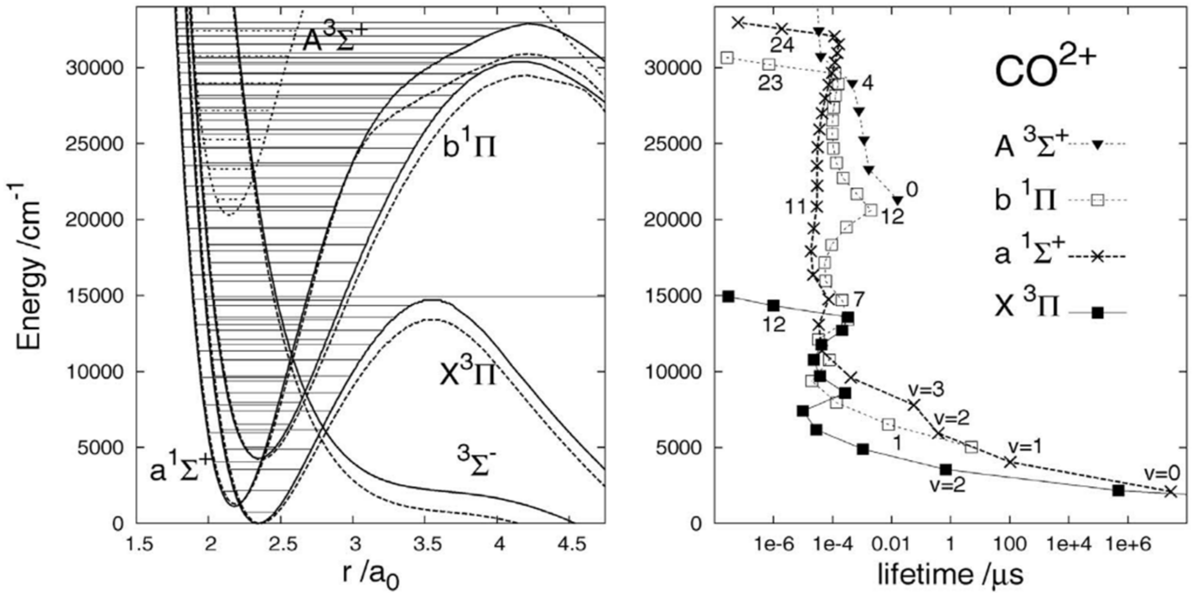

Figure 2.2.5 : *(a): Representation of the potential enery curves of four lowest electronic states of CO^{2+}, (b): life times of all the metastable vibrational states inside the potential well of the four lowest lying electronic states of CO^{2+} [70].*

Such 3-body fragmentation channels are used to investigate the effect of a charged environment on molecular fragmentation (see chapter 4). These channels are also used to reconstruct the initial structure of the molecular dimer using the Coulomb explosion imaging technique (see 2.3.1, 2.3.2 and chapter 5).

Case 3: If both x and $y \geq 2$. In this case, we expect a 4-body fragmentation channel with breaking of the van der Waals bond along with both covalent bonds on both sites of the molecular dimer. The production cross section and absolute detection efficiency of this channel make these 4-body channels hard to investigate experimentally. Even if these 4-body channels have an direct application in determination of the three dimensional geometry of the diatomic molecular dimers, they will not be discussed in this thesis due to the very low statistics.

2.3 Coulomb explosion imaging technique

Until now various instrumental advancements have been carried out to collect the required information needed to describe the collisions and fragmentation with details. In general this requires to measure the charge, mass and the velocity of the emitted particles. A review of such detectors used in the spectroscopic measurements is given in the article by Medhe [71].

Coulomb explosion technique were first introduced in 1980's for determining the stereochemical structure of molecular ions accelerated to energies of about 1 MeV. These ions were send through a foil and the exiting multiply ionized molecule then undergoes Coulomb explosion. Its initial structure is deduced from the energy and angular shifts measurement of the emitted fragments [72, 73]. At the same time the new developments in the spectroscopic techniques had also been carried to collect all the ions and electrons produced during collision with the best resolution possible [74, 75]. These are known as recoil ion spectroscopy, recoil ion momentum spectroscopy (RIMS) or cold target recoil ion momentum spectroscopy (COLTRIMS). The first measurement performed on RIMS was to observe projectile deflection in terms of scattering angle from an atomic target [76]. Several teams together have contributed in developments to achieve the most efficient spectroscopic instrument for measuring the kinematics of projectile and target collisions [74, 75, 77, 78]. The kinematically complete measurements in COLTRIMS involves, the detection of the projectile ions, along with the recoil ions (fragments) and electrons in multiple coincidence with a 4π solid angle collection efficiency.

For highly charged low energy projectiles in few hundred keV regime the electron capture is the dominant process and may lead to multiple electron capture. For molecular or dimer targets, electron can be captured from both sites resulting in a Coulomb explosion of the target. Collection of these recoil ions and measurement of their momentum vectors to access the initial geometry is known as Coulomb imaging technique. As explained in the previous section, the rapid ionization of the target is a key requirement in the Coulomb explosion imaging (CEI) technique to ensure that the nuclear motion before explosion is negligible. Recently, it has proven to be a powerful tool in investigation of the fragmentation dynamics of covalent molecules [57, 60, 79–81].

Ideally, the complete determination of the three dimensional structure of diatomic molecular dimers would require the full atomisation of the target i.e. the detection of the four constitutive atomic fragment ions. However,we will show in chapter 4 that a partial information on this structure can be deduced from the 2-body and 3-body fragmentation channels.

2.3.1 van der Waals bond cleavage

Molecular van der Waals complexes are dedicated polyatomic systems for enhancing our knowledge of intermolecular potentials, which helps in understanding fragmentation dynamics, environmental perturbation inside clusters and the geometry of these clusters. As already established, the collision between slow (low energy) highly charged projectile ion and a dimer can be explained in 2 steps where the first step is the capture process and the second step is the relaxation process.

For direct transitions from the fundamental state to a dissociative state, in which the projectile removes one electron from the two centres of the dimer, the doubly charged dimer will fragment via the $(M_2)^{2+} \rightarrow M^+ + M^+$ channel. This process is called Coulomb explosion. Because of the large intermolecular distance ($\geq$ 2.1 Å), the $M^+ + M^+$ dissociating curve can be fairly approximated by a pure Coulomb curve [82]. The sum of the kinetic energy of each fragment called Kinetic Energy Release (KER) can then be calculated using the Coulomb potential:

$$KER = 14.4 \times \frac{q_1 q_2}{R},$$

where the q_1=1 and q_2=1 are the charges on each fragment and R is the intermolecular separation. Experimentally, the position of the KER peak for such a 2-body channel will be used to derive the intermolecular distance.

2.3.2 Fragmentation of molecules and dimers

Previously in our group in CIMAP, the fragmentation of diatomic and triatomic molecules have been studied with both low energy and high energy ionic projectiles [83, 84]. The work done in the thesis of M. Terisien studies the dependence of the projectile velocity (11.4 MeV/u O^{7+} and 4 keV/u O^{7+}) on the population of excited states of CO^{2+} [51].

Multiple ionization followed by Coulomb dissociation has been extensively studied for molecules and dimers under intense laser fields [45, 57, 79, 81, 82, 85–87], pulsed electron beam [88] and ionic projectiles [57, 80]. Here is a brief review of various experimental results obtained using the Coulomb explosion imaging technique. In a study concerning the vibrational states of O_3 using two laser pulse duration, short 9 fs and long 40 fs, with an intensity of 2×10^{15} W/cm^2, it has been found that the nuclear dynamics are induced in the longer pulse duration [79]. The triply ionized O_3 molecule has shown stretching along all the three vibrational coordinates including anti symmetric stretching among all coordinates.

Using a triatomic molecule such as CO_2, the many body structure increases the internal degrees of freedom as well as the number of fragmentation pathways. In 2010, Neumann et al. used 3.2 keV/u Ar^{8+} projectiles to collide with a CO_2 target jet [80]. The 3-body fragmentation channel from the CO_2^{3+} trication had been investigated and three different fragmentation pathways were observed: synchronous direct fragmentation, sequential fragmentation and asynchronous fragmentation. The asynchronous fragmentation arises from the molecular bending and asymmetric stretching. Similar distinction between sequential and non sequential fragmentation have been observed by the Wu et al. using femtosecond laser [82] and Wong et al. using pulsed electron beam [88]. For another triply ionized polyatomic molecule OCS, the separation of direct and sequential fragmentation has been provided using the intermediate CO^{2+} or CS^{2+} rotation before its unimolecular fragmentation [81]. Note that all these experiments use the KER measurement as a tool to distinguish between the different fragmentation pathways.

There had also been several studies on molecular and mixed clusters using the CEI technique, all of them have used phase controlled femtosecond laser with intensity varying between 10^{14}-10^{15} W/cm^2. In 2014 Xie et al. studied the CO_2 dimer, trimer and tetramer by using the KER distribution for all the 2, 3 and 4-body channel respectively. They found that the $(CO_2)_3$ trimer has essentially an equilateral triangular geometry and the $(CO_2)_4$ has a regular tetrahedral geometry. Moreover, it has been found out that the intermolecular distance is the same in all the three clusters [86]. Such properties have already been reported for rare gas clusters $Ar_{n\leq 4}$ and $Ne_{n\leq 4}$ [85, 87]. These similarities between rare gas and non-polar molecular CO_2 clusters seem to indicate that the internal structure of the constituents plays a minor role on the geometry of the clusters. The structure of mixed cluster N_2Ar have also been determined using 2 and 3-body channels of the van der Waals complex [89]. The N_2 molecule is found to make an angle of 90° with the dimer axis at an intermolecular distance of around 3.7 Å. Similary, a T-shaped geometry was observed for $ArCO$ dimer [45].

In this thesis, we used a similar CEI technique to access the information about fragmentation dynamics and geometry of diatomic molecular clusters induced by collision with slow highly charged ions. Our experimental setup and the results will be detailed in the next chapters.

Experimental Technique and Calibration

3

Contents

We use a COLTRIMS (COLd Target Recoil Momentum Spectroscopy) [74] setup to measure in coincidence the charged fragments emitted following the collision of a molecular cluster target and slow highly charged ions (HCI). In this chapter, I will present the whole experimental technique and briefly describe the different parts of our experiment. It includes the low energy HCI projectile beam provided by the GANIL's (Grand Accelerateur National d'Ions Lourds) ARIBE (Accelerateur de Recherche avec les Ions de Basse Energie) facility. In the next section, preparation of the target jet beam is discussed followed by characterization of this jet with the help of a quadrapole mass selector (QMS). After this, I will briefly introduce our spectrometer along with the details about the detectors used in our setup and give an introduction to our new digital acquisition system. At the end, time of flight (TOF) and position calibrations will be discussed to support the confidence in our measured data.

3.1 General description

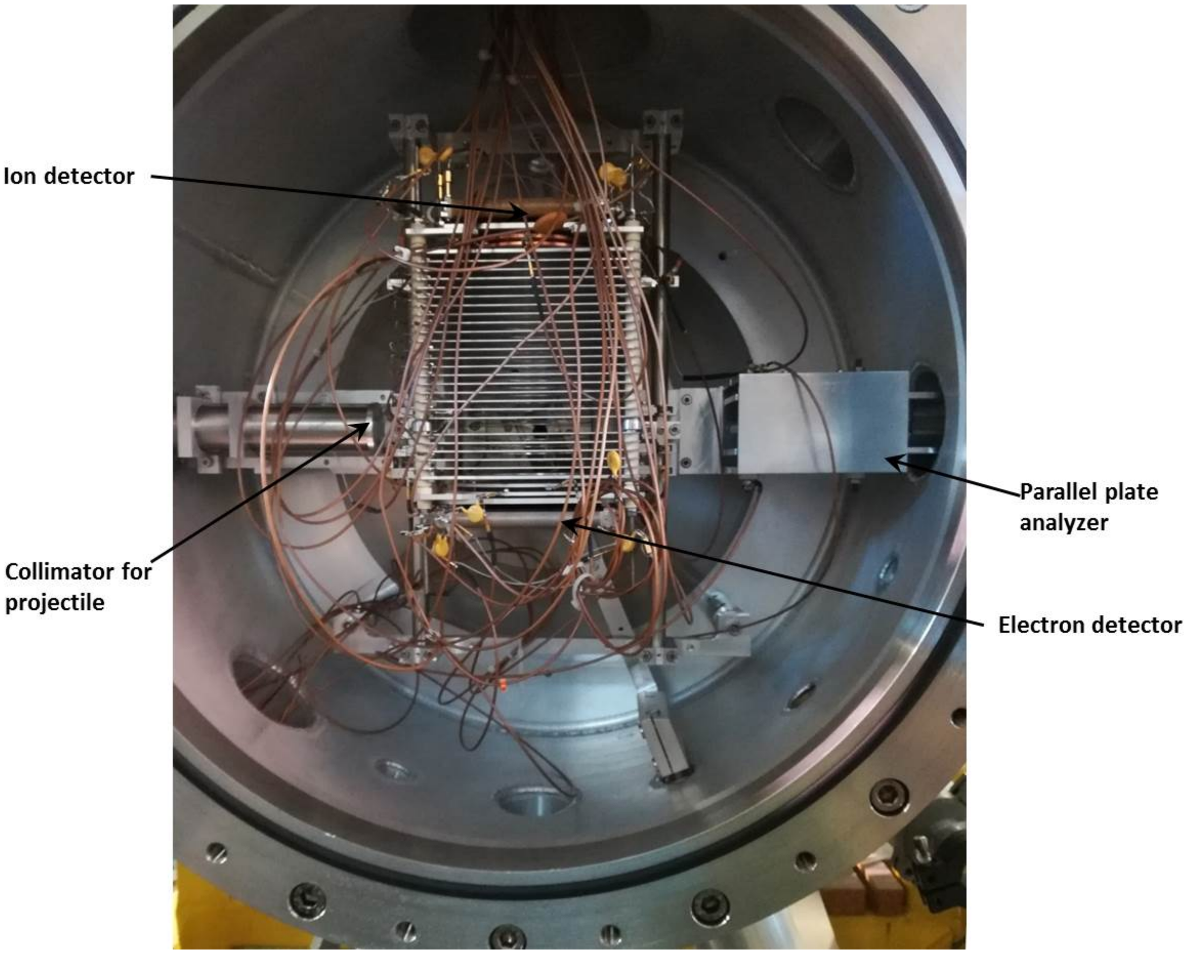

Figure 3.1.1 : *Recoil Ion Momentum Spectrometer in its chamber with highlighted sections, the target jet is in the plane perpendicular to figure*

The figure 3.1.1 is a picture of our spectrometer placed inside the chamber showing the spectrometer as well as the detectors for the recoil ions and electrons. On the left side there is a cylindrical tube with a collimator of 600 μm, through which the projectile ions enter the chamber. The projectile used are Ar^{9+} and Xe^{20+} of 15 qkeV energy, produced by an 14.5 GHz ECR ion source of the very low energy facility of GANIL. Once the projectile enters the collision region of the spectrometer, it collides with the target beam produced by a supersonic gas jet. We can see the collision region in figure 3.1.2 where the target molecule/cluster get ionized by the projectile, mainly through electron capture, followed by fragmentation of the target. These fragments (as seen in the figure 3.1.2) are then extracted using a homogeneous electric field of 40 V/cm towards a position sensitive detector (PSD) for recoil ions. In addition, after collision the projectile may have different charge states (q_o-1, q_o-2, q_o-3 etc) which are analyzed using a charge state analyzer consisting of a parallel plate analyzer (PPA) and a PSD detector located about 1.25 m away from the center of the collision region. As soon as the projectile reaches its PSD, it gives the START signal for the TOF measurements. Moreover the final charge state of the projectile is deduced by its impact position (X,Y) on this detector. TOF is measured in coincidence and calculated as the difference between the detection of the projectile and the detection of a recoil ion; each ion detection acts as a STOP signal. The electron detector was not used during the experiment performed during my thesis so it will not be discussed in the manuscript.

Although the relevant TOF is the time required for ions to fly from collision region to the ion micro channel plate (MCP). Note that the flight time of the projectile from the collision region to its detector is about 1-2 μs (depending on its mass and the kinetic energy of the projectile). This time is long in comparison to TOF therefore it can not be neglected. Further discussion about this time delay is done in TOF calibration later in this chapter.

Using the TOF and position coordinates we compute the 3D momentum vectors of each fragment using the equation of motion in the homogeneous electric field. Moreover, a data selection is applied using the conservation of momentum law, see Annex A. Once we have the desired set of 3D momentum vector for each and every ion, we can calculate the associated kinetic energy.

3.2 COLd Target Recoil Ion Momentum Spectroscopy

COLTRIMS; is a momentum spectroscopy technique which enables to measure 3D momentum vectors of recoil ions with high resolution and 4π solid angle, making it good for the coincidence measurements [37]. Mainly in this section I will discuss about the spectrometer's design, as well as a description of the recoil ion detector used for TOF and position measurement using Micro Channel Plate-Delay Line Detector. Although MCP detector will be discussed later in

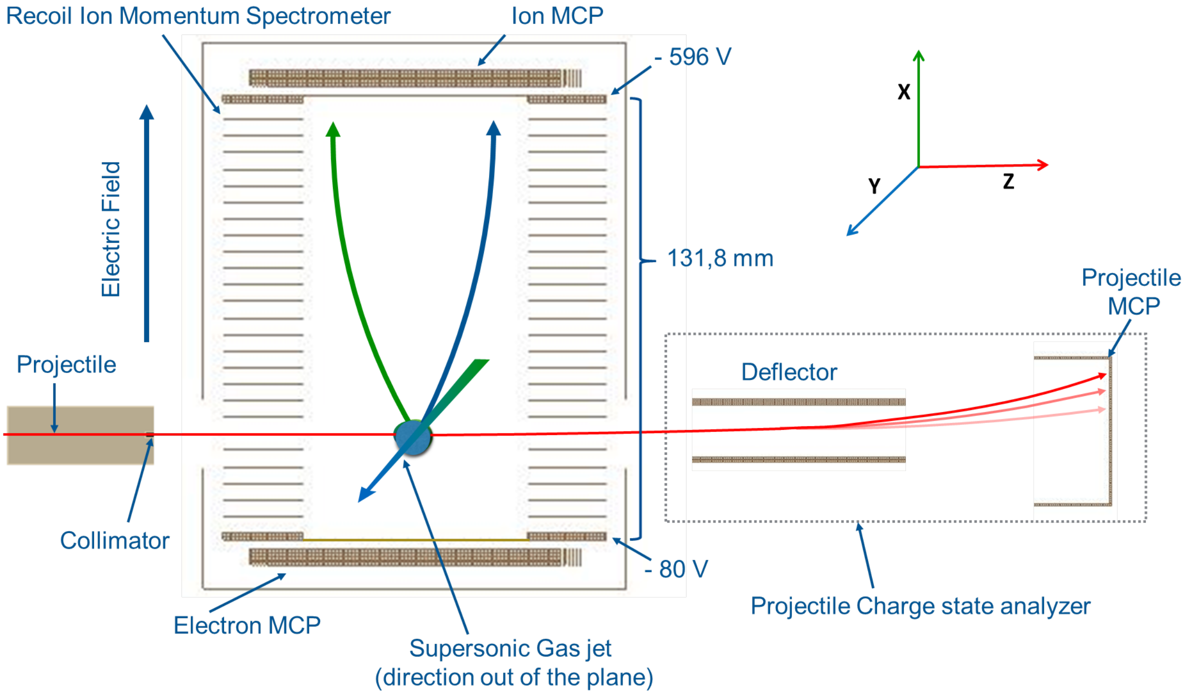

Figure 3.1.2 : *Schematic of experimental setup highlighting the reference axis, X=Extraction axis, Y=Supersonic gas jet axis, Z=Projectile axis. Typical voltages applied to both grids before detector are also shown. A resistor chain ensures a constant voltage difference between each electrode of the detector resulting in an homogeneous electric field inside the spectrometer volume.*

this chapter. Figure 3.1.2 also shows the mechanical aspect of the spectrometer used in our experiment. The region where the projectile and target are crossing is 10 mm gap between two electrodes. Starting from the center of collision region and moving up towards recoil ion PSD, we have a set of 19 equidistant electrodes of 1 mm thickness with a 4 mm separation between them using ceramic spacers. To have a uniform electric field across the extraction region, there is 2.75$M\Omega$ resistance between each electrode. In this region the uniform electric field gives an acceleration to recoil ions to reach the ion MCP detector. The two upper and lower electrodes (in front of the ion and electron detectors) are 2 mm thick and had a 90% transmission grid to ensure the homogeneous field. This provides the total length of our extraction region (for Ions) as $L_d \cong 100mm$ from the center of the collision region to detector.

Following the collision of the projectile and the molecular or cluster target, positively charged fragment ions are accelerated towards the ion detector. During the experiment the electric field is set to a minimal value which is calculated by taking the maximum kinetic energy of fragment to be detected [84]. For a spectrometer of length L_d using a homogeneous electric field of strength E and a detector of diameter ϕ_d, one can demonstrate that 100% collection is achieved for recoil ions of charge q and maximum kinetic energy K_{max} using relation below:

$$K_{max} = \frac{q.E}{16} \times \frac{\phi_d^2}{L_d}. \tag{3.2.1}$$

In our case, using L_d= 100 mm, E= 40 V/cm and ϕ_d=80 mm, we find a limit of 16 q.eV using equation 3.2.1. All these ions have characteristic TOF under the influence of uniform electric field which depends on the mass and charge, $TOF \propto \sqrt{\frac{m}{q}}$. The TOF also depends on the velocity component of the ion fragment in the X direction (v_{ox}) of the spectrometer (see figure 3.1.2). After the extraction region between the front side of the MCP and the top grid is the post acceleration region, the voltage on the MCP front in nearly equal to -3000 V to ensure the maximum detection efficiency of ions with $\frac{m}{q}$<28 [90].

3.3 Target Preparation

3.3.1 Cold Target

The "COLT" in COLTRIMS refers to the cold target, that is the other section of our experiment setup used to prepare the neutral target beam. This target beam could be monomer (atom/molecule), dimer, trimer or higher order cluster. For preparing this neutral beam we use a supersonic gas jet which has a nozzle of few tens of microns diameter. Since the 70's many studies have been done to determine the relationship between jet properties and the experimental parameters. [91–94]. Mostly in past, supersonic jets were used to cover the studies of translational, rovibrational and even electronic relaxation, atomic and molecular spectroscopy, scattering processes in gas (target) and projectile (photon, laser, ions) and physics in van der Waals complexes or clusters [95]. There were many other application in field of surface interaction, nuclear fusion, aerospace studies etc. In most of these important applications, it is of interest to obtain, narrow velocity spreads (or very low temperatures) in the jet, high density, and a variable kinetic energy from the thermal to the electronvolt range [96]. In our case, the supersonic jet is used to achieve the velocity spread much lower than the fragmentation velocity so that the maximum possible momentum resolution can be achieved. Secondly, this technique also allows the formation of small molecular clusters in the supersonic expansion of the molecular gas.

3.3.1.1 Supersonic gas jet

The supersonic jet is obtained by adiabatic expansion of the target gas which is initially under high pressure P_0 and move in a low pressure region [91]. Different gases can have different jet characteristics depending upon experimental parameters, such as temperature of the nozzle (T_0), inlet pressure (P_0), backing pressure (P_1) and few other physical adjustment which will be mentioned in the next section.

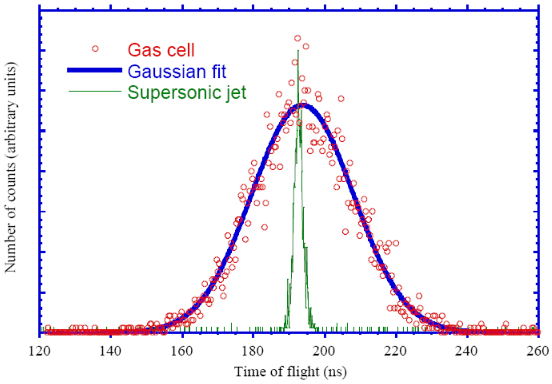

Figure 3.3.1 : *Comparison of velocity components according to the axis (TOF axis) of extraction between a gas cell (with Gaussian fit in blue) and a supersonic jet of Argon [83]. The TOF of Ar^+ is directly proportional to the v_{ox} component of the recoil ions. The width of these peaks is due to the initial thermal motion of the Ar atoms, therefore slow initial velocity spread of supersonic gas jet provides good momentum resolution.*

The gas is allowed to expand through an orifice nozzle of diameter D, in such a way that equation 3.3.1 is followed:

$$\frac{\lambda_0}{D} \ll 1 \tag{3.3.1}$$

where λ_0 is the average mean free path of a gas atom or molecule under pressure P_0. Due to multiple collisions the flow along the nozzle converts the random thermal agitated movement into a directed translational flow along the jet axis.

When gas expands in the low pressure region the thermal agitation becomes so weak that molecule start to lose the velocity component perpendicular to jet axis. Due to transfer of this thermal energy in the final velocity of the jet we have a high velocity jet (more than sonic, Mach number $M > 1$) which is almost monokinetic. This eventually brings the translational tempuratures down to 10^{-2}K (see figure 3.3.1 [83]). For the case of polyatomic molecules we have more degrees of freedom in form of the rotational and vibrational energies. It has been shown that the vibrational and rotational degrees of freedom are also cooled down as translational motion. Therefore, the vibrational temperature near few K could be achieved [97, 98].

Figure 3.3.2 show the schematic of different sections of the supersonic gas jet setup. After the expansion the cold beam passes from a first stage to a second stage and in this second differential chamber we use a collimator of $500\mu m$ to fix the size of the target beam before it enters the collision chamber. P_1, P_2 and P_3 represents the pressures in three different chambers from which the jet passes. In the first stage/chamber where the expansion took place, we use series of root pumps to achieve the pressure P_1 low enough down to $10^{-2} - 10^{-3}$ mbar (primary

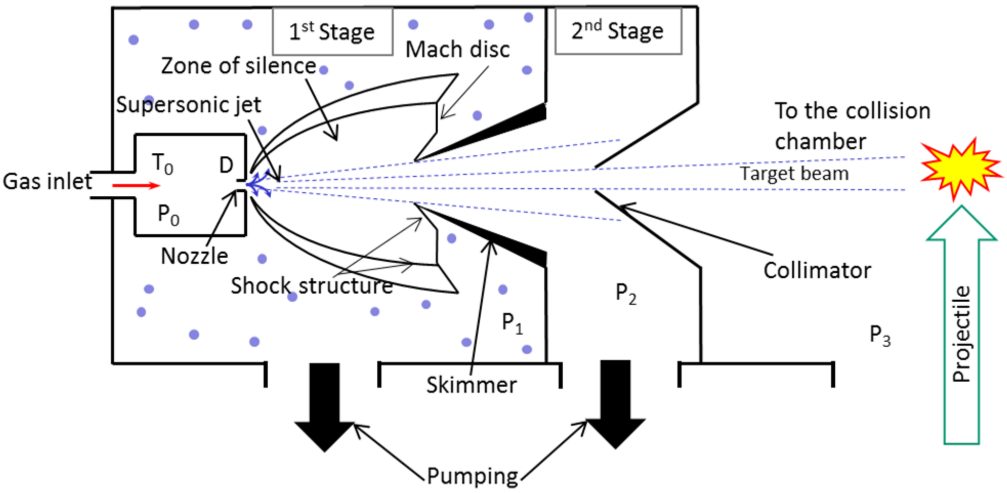

Figure 3.3.2 : *Campargue type supersonic gas jet schematic, Along the nozzle contour, a boundary layer forms, it is a thin flow layer attached to the nozzle walls that connects the high velocity flow in the volume of the flow domain with flow boundary that is immediately attached to the confining walls and therefore has zero velocity. These boundary walls are often termed as shock structure, as they shock the particle back to the flow domain. The gas jet flowed in the first stage is extracted by a sharp skimmer placed in the "zone-of-silence" without breaking its characteristics [92].*

vacuum). These pumps have pumping capacity of 40 m^3/h, 253 m^3/h and 2050 m^3/h. Then in stage 2, which is a differential pumping chamber with vacuum of the order of 10^{-5} mbar, a primary pump along with a turbo pump (capacity 400 l/s) is used. Just before the collision chamber there is valve to prevent the entry of jet before the desired vacuum is reached. Finally beam enters the collision chamber where the vacuum is of the order of 10^{-7} mbar achieved with the turbo pump and an additional liquid N_2 screen is added to achieve better vacuum conditions down to 10^{-9} mbar. Although, the primary objective of this screen is to reduce the water vapours from the background inside the collision chamber. Figure 3.3.3 shows a mechanical schematic of the supersonic gas jet setup and the pumping system for the collision chamber.

To avoid the diffusion of the jet in the collision chamber we use a beam dump with a turbo pump along jet axis. A quadrupole mass selector is also placed in the this beam dump and serves as a diagnostic to characterize the jet properties (see later).

3.3.2 Jet Parameters

Before we move to the characterization and optimization of the target jet, here we discuss very briefly about the size and the velocity of the beam. Due to the design of the setup, the diameter of the jet D_{CP} at the point of collision depends on geometrical parameters. In figure 3.3.4 we can see a schematic on how the diameter of jet and its divergence depends on the nozzle, skimmer and collimator assembly.

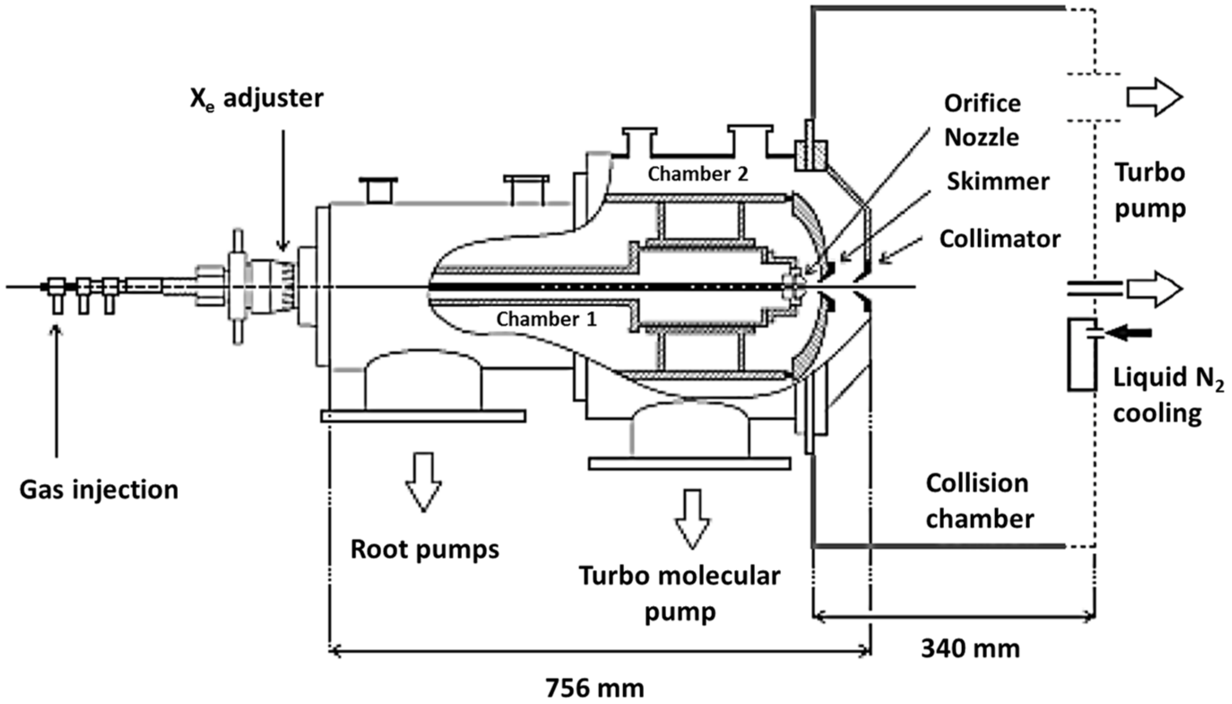

Figure 3.3.3 : *Mechanical details of the gas jet setup and the pumping system [78].*

The size of the beam at the collision region can be calculated using the parameters of our setup: an orifice nozzle of diameter $D_N \simeq 30\ \mu m$ and the distance between the nozzle and the skimmer $X_e \simeq 6$ mm. From figure 3.3.4 we can deduce the diameter of jet at the collision point from equation 3.3.2.

$$D_{CP} = \frac{\left(D_N * \left(1 - \frac{L}{d}\right) + \left(\frac{L}{d} * D_{COL}\right)\right)}{1000} = 1.5mm \tag{3.3.2}$$

The velocity of the jet also plays an important role, the average velocity of the diatomic gas jet is given by:

$$V \approx \sqrt{7\frac{RT}{M}} = 789m/s \tag{3.3.3}$$

where R is the molar gas constant, T is temperature of the gas (during entrance) and M is the molar mass of molecule in kg [83]. This value is very close to what we obtain through experimental calculations see in chapter Annex A. The velocity of the clusters inside the jet is also the same as the average velocity of the monomers because the fraction of cluster inside the jet is very low (about 1%). Therefore, the dominant monomer molecule act as a carrier gas and fixes the velocity of all particles inside the jet.

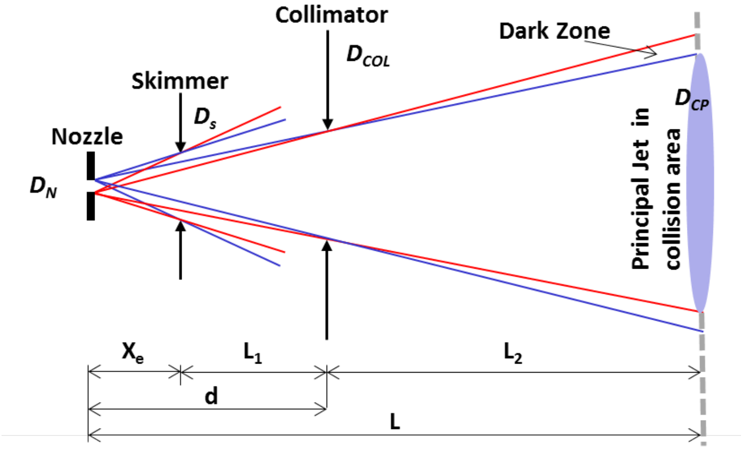

Figure 3.3.4 : *Geometrical arrangement for the gas jet setup, diameter of skimmer is* $D_S = 463\mu m$*, diameter of collimator is* $D_{cp} = 500\mu m$*, distance between skimmer and collimator is* $L_1 = 34mm$ *and collision point is situated* $L_2 = 85mm$ *from collimator.*

3.3.3 Optimization of cluster production

To obtain the improved jet properties the product of $P_0 * D_N$ should be larger than $1mbar \cdot cm$ [84]. Since the experiment for this thesis were majorly done on molecular clusters, it is important to study the dependence of these parameters on cluster formation at room tempараture, as no pre-expansion cooling or external cooling of nozzle is utilized. Most of the previous work done with supersonic jets is usually with a low temperature nozzle, which highly increases the size of cluster even at the low P_0 [38, 99–102]. We have used a nozzle with a diameter of D_N=30 μm and the P_0 can range upto 30 bars. The other controlling parameter is X_e which can be adjusted using a screw gauge type distance manipulator. We can manipulate inlet pressure and the distance X_e to achieve the best suitable condition for monomer, dimer, trimer etc. For this we have a quadrupole mass selector (QMS) placed along the jet axis but after the collision chamber; in the beam dump chamber. Our approach here is to measure the pressure reading on the P_2 and P_{Beam_Dump}. We use a small turbo pump to evacuate the gas beam, the same pump is also used to maintain a minimum vacuum $(10^{-4} mbar)$ in the QMS for its operation.

To characterize the jet we first take down initial values of P_2 and P_{Beam_Dump} and a background mass spectra from the residual gas inside the chamber. Then we start from the lowest value of P_0 and move X_e from lower to higher values. For each step we record the values of both pressures. Maximum pressure of $P_2 \simeq 5 - 7 \times 10^{-4}$ mbar and $P_{Beam\_Dump} \simeq 8 - 9 \times 10^{-5}$ mbar are limited by the pumping capacity in our setup.

The Prisma Blazer QMS can scan the mass from 1 to 200 amu. Before injecting the target

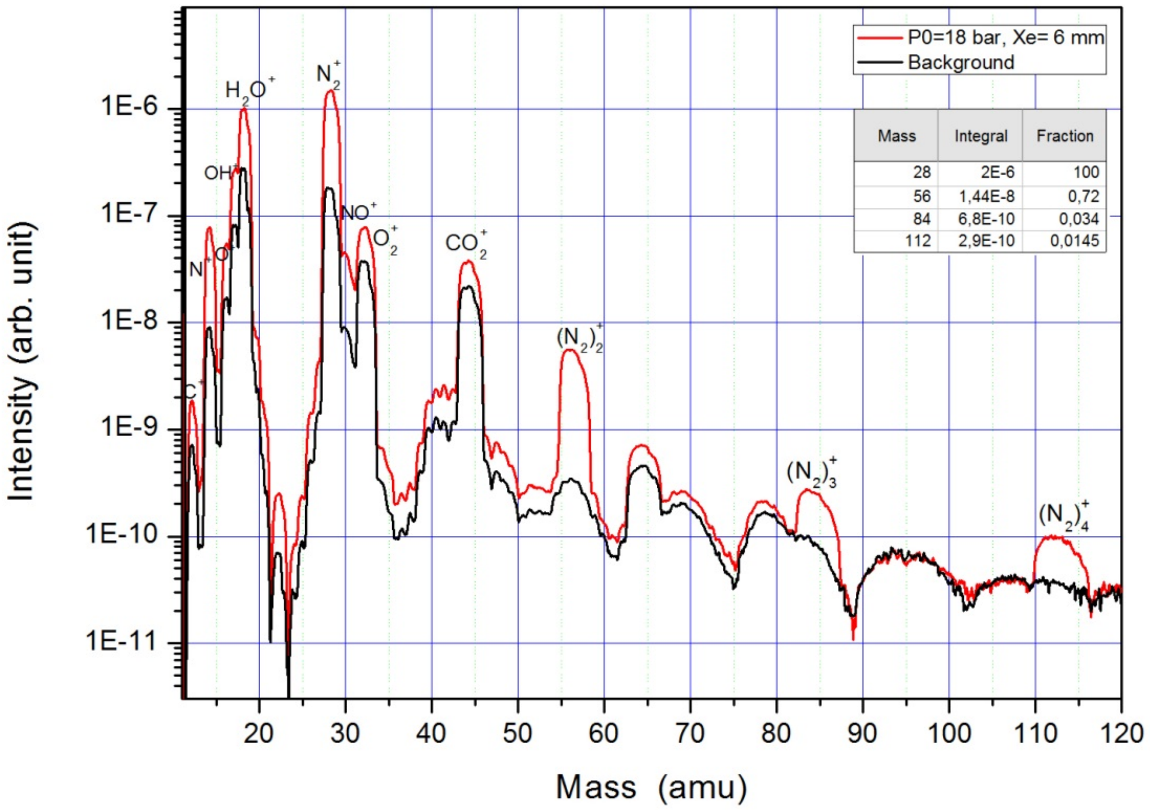

Mass	Integral	Fraction
28	2E-6	100
56	1,44E-8	0,72
84	6,8E-10	0,034
112	2,9E-10	0,0145

Figure 3.3.5 : *A mass spectra from QMS for* N_2 *gas jet and its clusters.* P_0= *18 bar and* $X_e = 6mm$

gas we make a QMS scan with only residual gas at the pressure below 10^{-5} mbar to have the background data. Figure 3.3.5 show the mass spectra for all the clusters of N_2, at the same time we can see the background spectra which is mainly composed of H_2O, O_2, N_2 and CO_2. The figure highlights the main peaks as well and in the top right corner a comparison of the dimer and trimer with respect to monomer fraction. Here the dimer is less than 1% and the trimers are about 20 times lower.

After we have values of P_2 and P_{Beam_Dump} for all P_0 from 5-25 bars with a step size of 2-3 bars, and for each value of P_0 we find the suitable X_e to have the best cluster fraction (for eg. dimer/monomer). The graphs in figure 3.3.6 gives an insight how the optimum value of X_e changes with the inlet pressure. The value of P_{Beam_Dump} indicates that the jet is localized and maximum dense beam is passing to the QMS region. Similarly when we move the nozzle far from the optimum value of X_e the jet start to get less dense, resulting the vacuum in the beam dump region go lower.

Finally, we choose the optimum values for inlet pressure and distance X_e, and then we

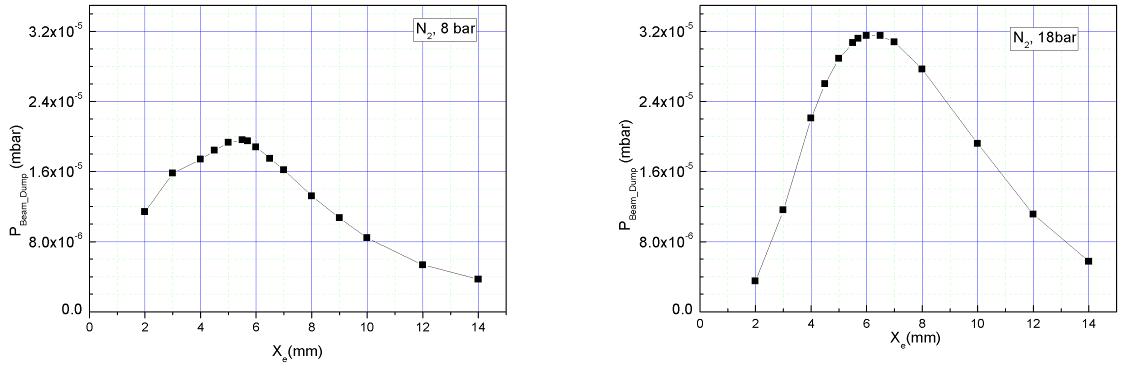

(a) **(b)**

Figure 3.3.6 : *Correlation of P_{Beam_Dump} with X_e for 2 different values of P_0 a) $P_0 = 8$ bars b)$P_0 =$ 18 bars*

record the mass spectra with the help of QMS. From figure 3.3.5, we can calculate the integral of monomers, dimers, trimers etc and then we can give a fraction on the basis of QMS data. We find that the fraction of dimer/monomer is between 0.72% to 0.8%. Few other graphs showing the dependence of the production of N_2 and CO clusters on various parameters are shown in Annex B. Note that the relative intensity of cluster given by this method is a larger limit of the real composition of the jet because a non-negligible portion of the clusters may fragment in the ionization process in the QMS.

3.4 Projectile

3.4.1 GANIL: Low energy facility ARIBE

For our experiments, we use the ARIBE facility of GANIL. This facility have five beam lines which can provide multicharged very low energy ($v_p \ll v_e, v_p$ is velocity of projectile v_e is outer shell electron's velocity) projectile ion beams [48] with the help of an 14.5 GHz ECR (Electron Cyclotron Resonance) ion source. Ion beams from He^+ upto Xe^{30+} can be produced. These highly charged ion beams have intensities upto 100 μA and they can be extracted with energies upto 25 qkeV. In figure 3.4.1 the picture shows arrangement of the ion source (in red) with the COLTRIMS setup in (in yellow) and beamline (in pink) to transport the projectile beam from the source to the experiment.

3.4.2 ECR Ion Source and Beam Line at ARIBE

A brief introduction of all the components inside an ECR ion source can be seen in the cross sectional view of GTS (GANIL Test Source) in ARIBE facility from figure 3.4.2.

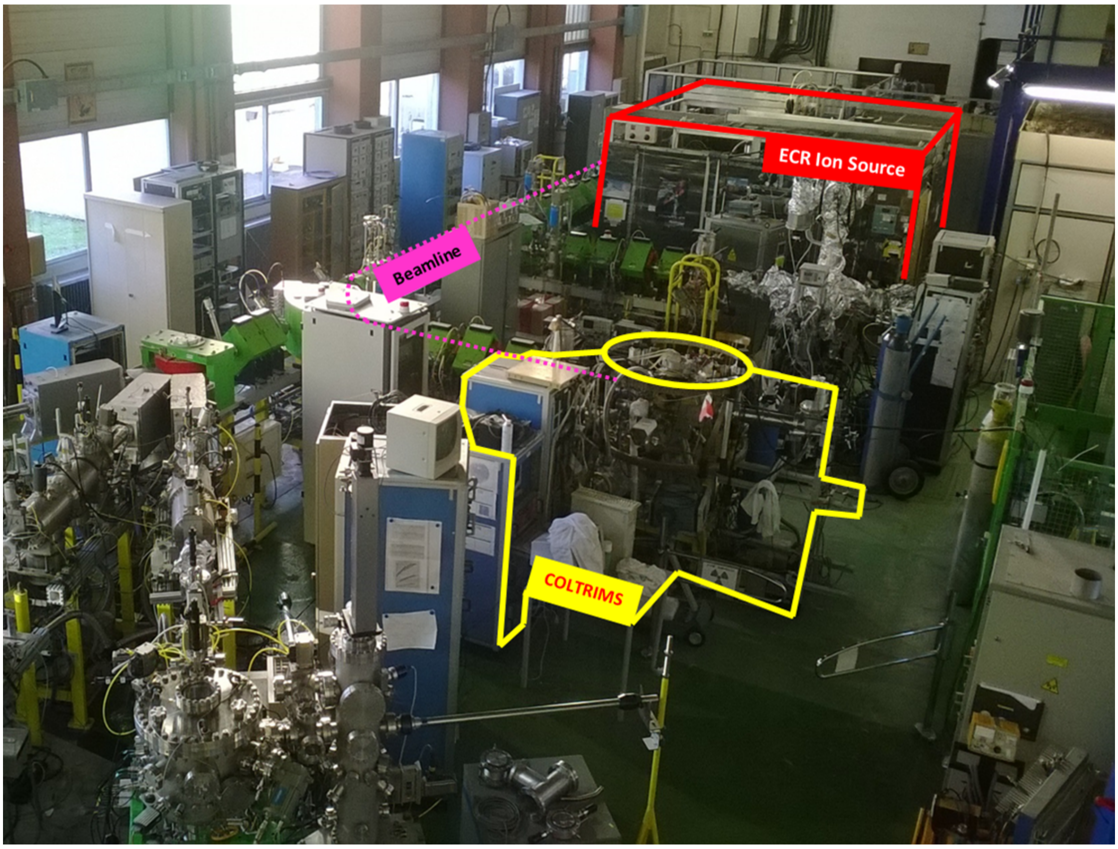

Figure 3.4.1 : *Picture showing the ECR ion source and experimental setup (COLTRIMS) with different beam lines in ARIBE facility of GANIL*

The principle of an ECR ion source is defined in many of the previous thesis from our group, so I will discuss only the characteristics of the source. The GTS ion source works at a frequency of 14 GHz and upto to 1000 W [103]. An ion of mass m and charge q is extracted from the source with a kinetic energy E_c which is equal to the product of the q by the value of the voltage difference V_s. The V_s is the voltage difference between the deck and the ground of the source.

$$E_c = q.V_s = \frac{1}{2} * m.v^2 \tag{3.4.1}$$

We used V_s = 15 kV in our experiment which gives energy of 135 keV for Ar^{9+} ion beam. From above equation we can derive the velocity for the ions from its :kinetic energy:

$$v = \sqrt{\frac{2 * E_c}{m}} = \sqrt{\frac{2 * q * V_s}{m}} \tag{3.4.2}$$

For Ar^{9+} at V_s= 15 kV, the velocity is around $0.807 \times 10^6 m.s^{-1}$. In atomic units it is equals to 0.369 a.u.. This velocity is less than 1 a.u. thus called low energy and electronic capture is

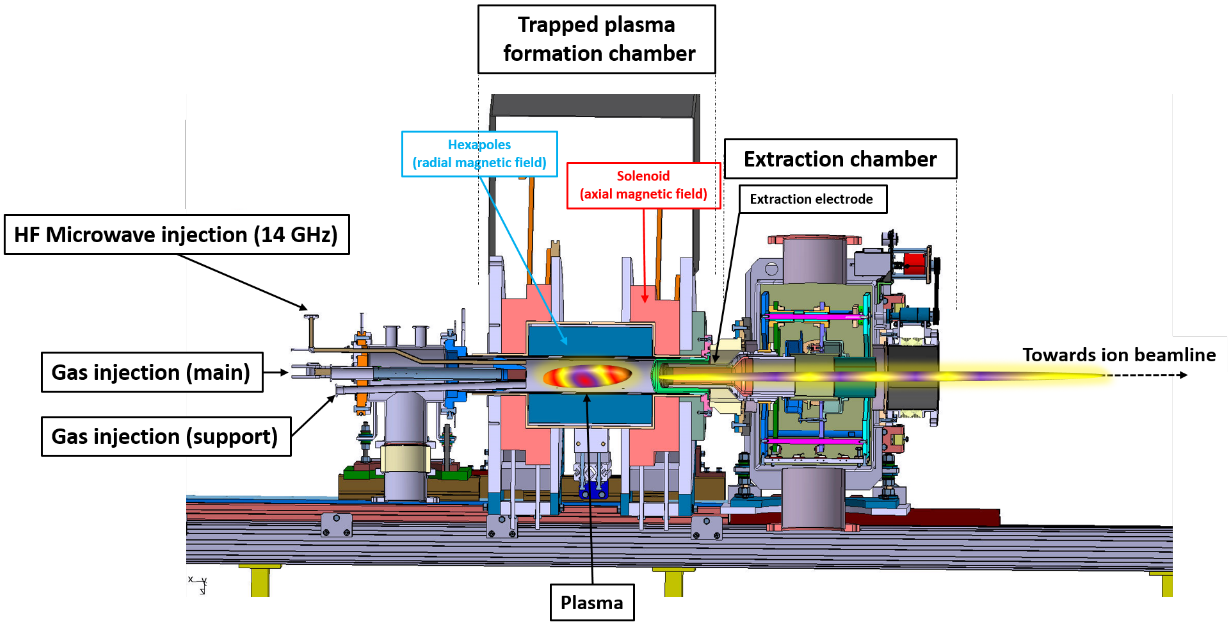

Figure 3.4.2 : *Cross-section view of the ECR*

the dominant interaction process during collision (see chapter 2).

After extraction of the ions from the source, they are selected according to their $\frac{m}{q}$ ratio using a magnetic dipole and then guided through the beam line using dedicated magnetic ion optics. A particle charged with mass m, charge q and velocity v evolving in a uniform magnetic field $\overrightarrow{B}$ and transverse magnetic field ($\vec{v} \perp \overrightarrow{B}$) follows a circular trajectory due to the application of the Lorentz force $\overrightarrow{F}$ (equation 3.4.3),

$$m \cdot \vec{a} = \overrightarrow{F} = q \cdot \vec{v} \wedge \overrightarrow{B} \tag{3.4.3}$$

.

From equation 3.4.3 we can deduce the fact that, for a value of magnetic field B, it's possible to select projectile on basis of momentum or energy. Putting $\vec{a} = \frac{v^2}{r} \cdot \overrightarrow{u_r}$ in equation 3.4.3, and using equation 3.4.2;

$$\frac{B \times r}{v} = \frac{m}{q} \Rightarrow B \times r = \frac{m}{q} \cdot \sqrt{\frac{2 * q * V_s}{m}} = \sqrt{2 * V_s}\sqrt{\frac{m}{q}} \tag{3.4.4}$$

The product $B \cdot r$ is called magnetic ridigity of the dipole and its 0.05 T.m in our beam line and it somehow limits the choice of charge and energy of the ions [103]. A set of perpendicular slits followed by a Faraday cup (CF13) for regulating beam intensity are placed before the first dipole. During our experiment we have measured the beam intensity of around 10 μA with these slits fully open. Moreover, there are several sets of vertical and horizontal slits along the beam line to control beam intensity. For guiding and shaping of the beam there are other component such as quadrupole units for focusing and de-focusing of the beam. After the beam is delivered to the COLTRIMS we have a Faraday cup (CF42) to measure the intensity just before our setup. Typical beam intensities of 1-2 μA were measured on CF42 with all the slits fully open. This intensity were drastically reduced (about 1 nA) using the different sets of slits in order to obtain the desired count rate.

3.4.3 Collimator and parallel plate analyzer

Once the beam is delivered to the COLTRIMS it is collimated with the help of two collimators, 10 mm and 600 μm respectively (figure 3.4.3) which defines the size of the beam to about 600μm. Then it moves to the collision region, where electron capture is occurs, leaving the projectile with different charge states. These different charge states are separated by deflecting them through an electric field from a parallel plate analyser. It is an assembly of two parallel plates with a constant electric field developed between them strong enough to deviate the main beam A^{q+} from the projectile detector. The potential difference between the two plates can be varied with respect to charge state of the beam that we like to investigate. In our setup, the gap between both plates is $2.84cm$ and the voltage applied to each plate is $\pm 170V$ for 15 qkeV Ar^{9+} projectile. This gives a field of about $120V/cm$. Additionally, the vertical position of the projectile detector can be adjusted to have A^{q+} out of the detector and $A^{(q-i)+}$ on the detector.

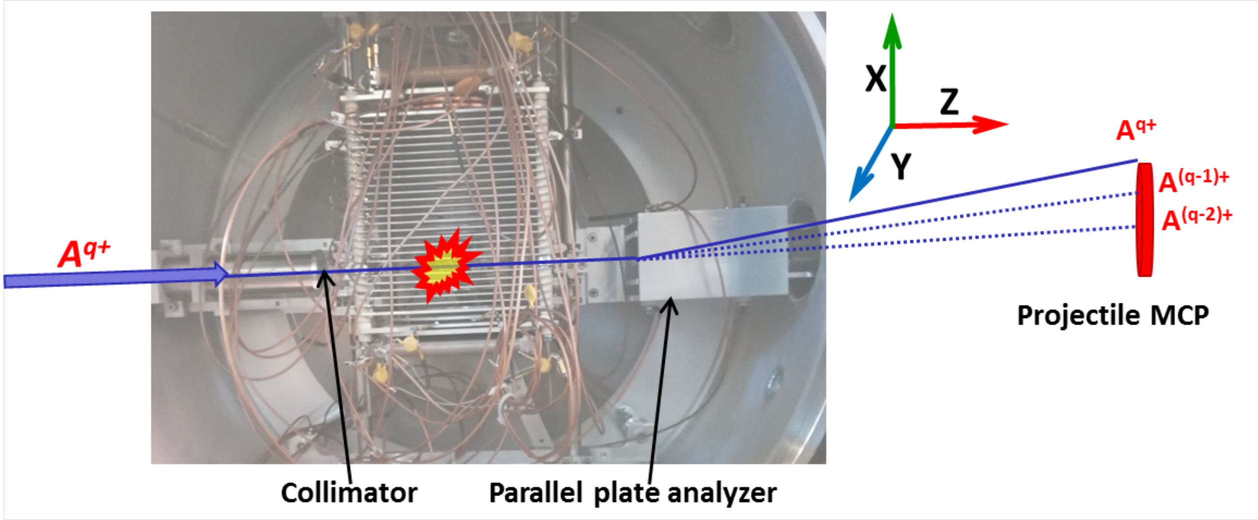

Figure 3.4.3 : *Figure showing the collimator for guiding projectile beam in the collision area and parallel plate analyzer to separate different charge state of projectile after collision*

3.5 Detection

3.5.1 Position Sensitive Detector (PSD)

Since we have to measure the 3D momentum of the positively charged ions we need the position and the TOF of the ions on the detector located at the top of the spectrometer. We use position sensitive detectors (PSD) composed of MCP and delay line anodes for the detection of these charged particles. This PSD is widely used as it is capable of detecting ions, electrons and even fast neutrals. This setup has three of such PSD , two of them ($\phi_{MCP} \approx 80mm$) mounted on each end of spectrometer for detecting positive recoil ions and electrons respectively and one to analyze the projectile charge state ($\phi_{MCP} \approx 40mm$). Since the detection of all the fragments is essential for the KER reconstruction, the recoil detector is used in multihit mode.

A MCP is a glass plate of around 1 mm thickness having closely stacked parallel pores of micron range diameter. These micro channels have a bias angle ($\approx 10°$) with the plate surface. Each of these channels has a inner wall coating of a semiconducting material having a low work function [104]. A potential difference of about 1000 V/MCP is maintained across the MCP by applying negative high voltage on incoming ion side (MCP Front) with respect to the back side (MCP Back). Each microchannel in the MCP acts as electron multiplier tube. Figure 3.5.1 shows a schematic of MCP's principle.

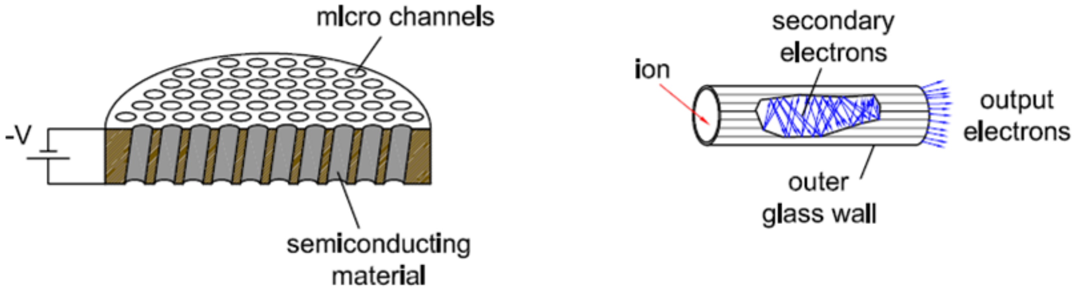

Figure 3.5.1 : *Schematic of an MCP and electron amplification in a micro channel*

When an ion hits the inner surface of a micro channel, secondary electrons are produced from the semiconducting material. These electrons are accelerated due to potential difference across the MCP and hits the wall of channel to generate a cascade of electrons thus amplifying the initial electrons signal by several orders of magnitude. Typically the amplification is of order 10^3-10^4 for a single MCP. The electron shower finally emerges out from the opposite end of the channel and is collected on a delay line anode. To increase the overall gain, it is often necessary to stack 2 or 3 MCPs together.

When two MCPs are stacked together such that the orientations of the microchannels of the plates mirror each other, it is called chevron (V-shaped) configuration. In this configuration, the electron shower from the first MCP is further amplified when it passes through the

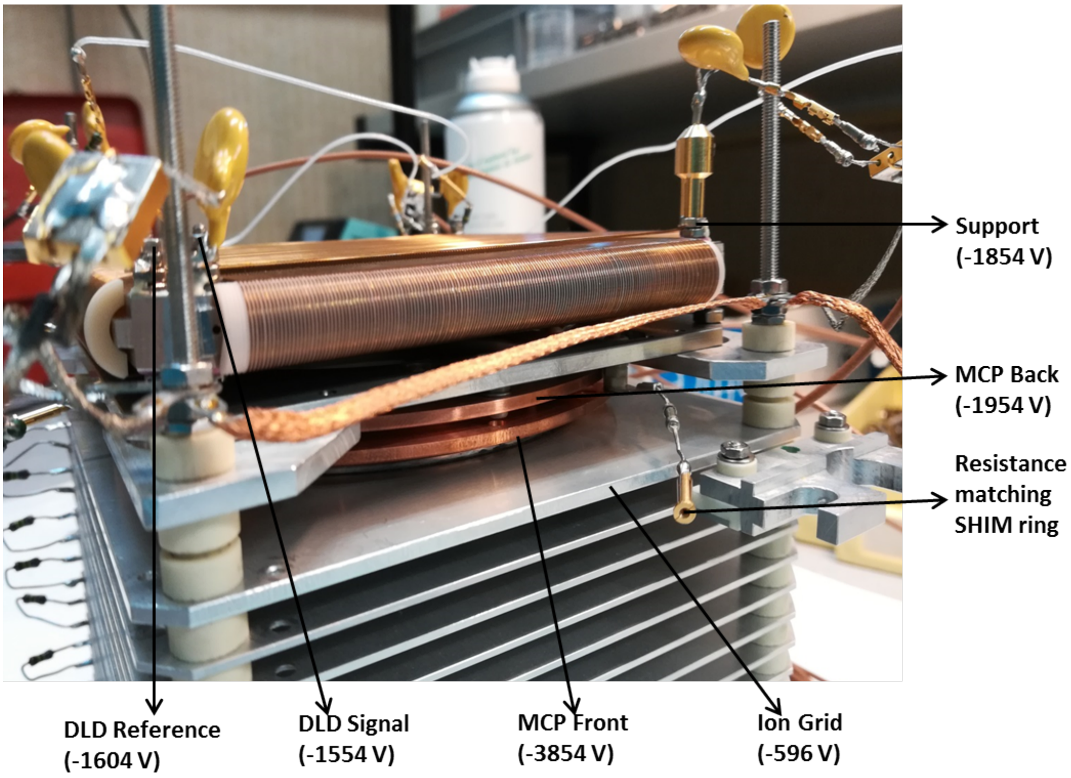

Figure 3.5.2 : *Picture of our recoil ion detector highlighting the necessary parts with respective biasing voltage to polarize the detector. All these part are purchased from Roentdek and Hamamatsu.*

micro channels of the second MCP thus increasing the overall gain. Such a chevron configuration is used in our setup and results in gain of about 10^6-10^7 for 950 V/stack polarization voltage [104]. Figure 3.5.2 gives details about the polarization of the recoil ion detector.

The position of ion on the MCP can be detected by tracing the position of the electron shower generated by the ion hit. We use a delay line anode in our setup due to its fast readout time and good position resolution for large area of detection [105]. The delay line anode comprises of bare copper wires which are wound around over an insulating ceramic support keeping a fixed gap of around 0.5 mm between the loops. There are two sets of delay lines anode (one for each axis Y ans Z) perpendicular to each other. When an electron shower falls on the delay lines, the time difference for the signals to arrive at the two ends of the wire depends on the position of the electron shower on the delay line anode. The position on our ion detector in (Y,Z) coordinates, is calculated using the propagation time of the signal from the hit point to the respective ends of the wire. In equation 3.5.2 the T1_YI and T2_YI correspond to the propagation time of the signal upto each end of the wire. Similar notations are used for the Z direction. C_{DLD} is the conversion factor of the "position/time" and corresponds to the signal propagation velocity along the delay line. The propagation of signal along the wire is about 60-70% of speed of light(about 20 cm/ns) and we can define the propagation time in the perpendicular direction ($T_\perp$) accounting for the length of one loop (200 mm for a detector with diameter of 80 mm) and the spacing between two consecutive loops (0.5 mm). This time is calculated for a single loop of wire and it is nearly 2 ns/mm [105]. Thus the transverse propagation velocity is:

$$C_{DLD} = \frac{1}{T_\perp} = 0.5mm/ns. \tag{3.5.1}$$

Finally the position is deduced from the time of arrival at both ends of the wire:

$$\begin{aligned} Y &= (T1\_YI - T2\_YI) \cdot C_{DLD}/2 \\ Z &= (T1\_ZI - T2\_ZI) \cdot C_{DLD}/2. \end{aligned} \tag{3.5.2}$$

Although this is just an approximate value but a more precise position calibration procedure will be presented in the section 2.7.

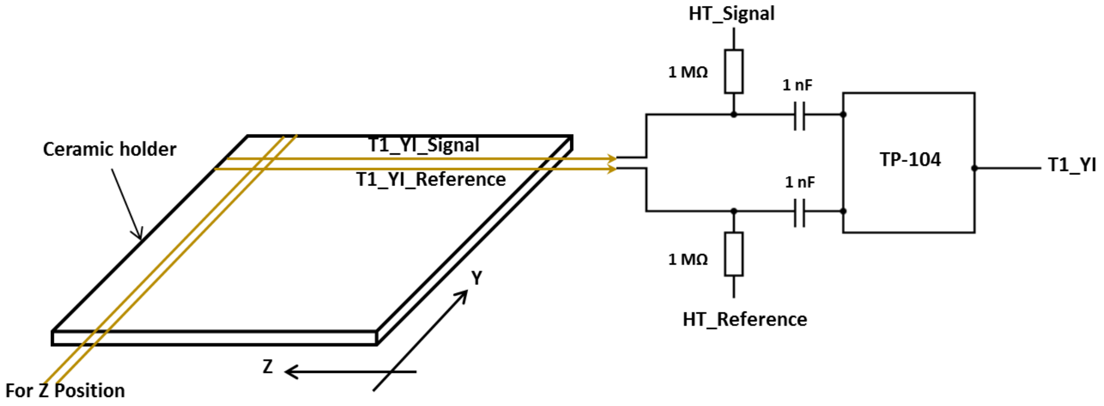

Figure 3.5.3 : *Schematic of DLD showing the electronics required to picking up the signal at both ends of the wires along the Y and Z directions.*

The signal propagation time from one end to the other of delay line is constant irrespective of ion hit position. It corresponds to the total length of the anode wire which is equal to $(T1\_YI + T2\_YI)$ for Y position, similarly $(T1\_ZI + T2\_ZI)$ for Z position. In figure 3.5.3 the electronics required for the DLD signal is shown, for each position a pair of wires are used one is biased to propagate signal and other for its reference. This arrangement allows to free itself from the noises captured by the antenna formed due to conductance of the winding of wire. It can also be used to filter out some false signal pairs generated through noises. Between the two parallel wires there is a voltage of 50 V. When the electron shower arrives close to the anode, it will preferably be captured by the 50 V polarized wire more than its neighbor. The electron signal is then located on only one of the two wires. This more polarized wire is called signal the other wire is called reference. Electromagnetic noise will induce the same noise signals on both wires at the same time. Both are fed to a RF pulse transformer "TP-104", which subtracts them and gives the final anode signal generated from electron shower. This signal is then pre-amplified before sending to the acquisition system.

3.5.2 Comparison between standard and tapered MCP

The surface covered by the open area is an intrinsic limitation for detection efficiency of MCPs. In a recent modification to improve the detection efficiency, the open area ratio (OAR) of a standard MCP is enlarged to increase the collection of incoming ion. This is achieved by tappering the edge of the microchannels (impinging end) more than usual, henceforth it is called Tapered MCP [106, 107]. The depth of the tapered area is $10\mu m$, and the cone angle is around 37° [106]. Figure 3.5.4 is a comparative image of standard and tapered MCP. The OAR is increased from 60% to 90 %.

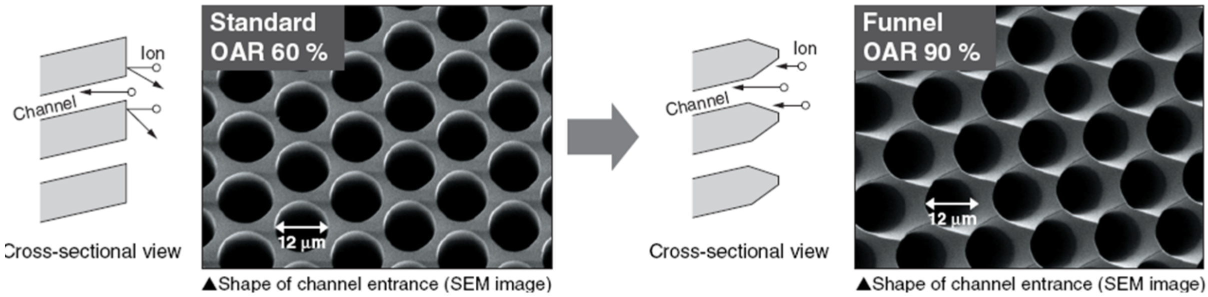

Figure 3.5.4 : *SEM image of a standard and tapered MCP showing difference in OAR to improve detection efficiency [104]*

A significant drop in the coincident multiple particle detection is observed when the detection efficiency is low. It is because the coincident detection of n fragments is proportional to the n^{th} power of the single hit detection efficiency ε [107, 108]. For example, a comparative result for upto 4-body absolute detection efficiency are mentioned in table 3.5.1.

Table 3.5.1 : *Comparison of absolute detection efficiency of standard and tapered MCP for single, double and triple hit events. The values of single hit ε are nearly equal to the OAR of each MCP respectively [107, 108].*

Number of ions (n)	n=1	n=2	n=3	n=4
$\varepsilon_{coincidence}=\varepsilon^n$	ε	ε^2	ε^3	ε^4
Standard	57%	32.5%	18.5%	10.5%
Tapered	90%	81%	73%	65.5%
Ratio	≈ 1.55	≈ 2.5	≈ 4	≈ 6

It appears from the table above that the detection efficiency for a 4-body fragmentation is expected to be upto 6 times better with tapered than standard MCP. An increase in count rate of such magnitude reduces the measuring time of the experiment or increase the statistics.

There has been some experiments in recent year to find the absolute detection efficiency of a tapered MCP [106,107]. The figure 3.5.5 below show the comparison of the absolute detection efficiency of Xe^+ and Ne^+ ions of energies ranging from $1.5-5keV$.

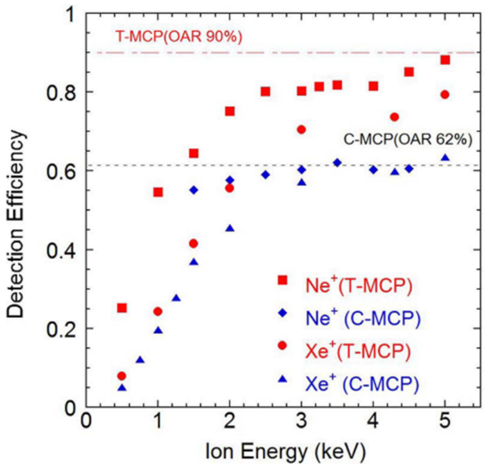

Figure 3.5.5 : *Absolute detection efficiencies of T(Tapered)- and C(Standard)-MCPs for the Ne^+ and Xe^+ as a function of the incident ion energy. The dashed-dotted and dashed lines are the OARs of the T-MCP (90%) and C-MCP (62%), respectively [107].*

The improvement in the detection efficiency can be seen for the tapered MCPs and the values of ε are very close to the OAR values for both tapered and standard MCP. In [108] work the ε is calculated from the coincident detection of H^+ ions in the fragmentation of $H_2^{2+} \rightarrow H^+ + H^+$. Measurement is performed for 3 different MCPs and it is also in agreement with the dependence of ε in a linear relation with the OAR of the MCP.

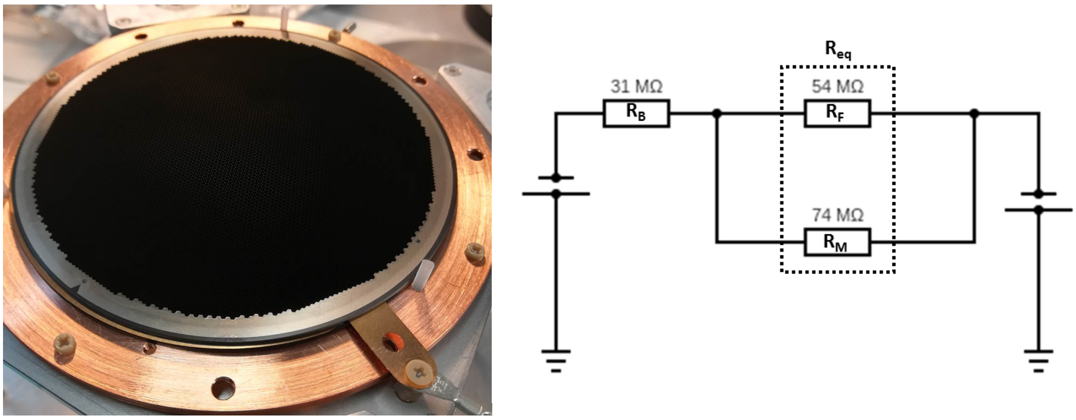

(a) **(b)**

Figure 3.5.6 : *Picture of the tapered MCP we use in our setup (Left), circuit for resistance matching(Right)*

For our experiment we have used a two stages chevron configuration MCP, the first one of them is tapered MCP (figure 3.5.6a) followed by a standard one. At the collision chamber pressure of $3 \cdot 10^{-7}$ mbar the resistance of both MCPs are $54M\Omega$ and $31M\Omega$. Since it is a big difference in the resistance so we have to use an intermediate electrode (referred to as "shim ring" on figure 3.5.2) in between the two MCPs to match the resistance and ensure the same voltage difference for each MCP. Figure 3.5.6b show the circuit diagram for resistance matching where R_F is front MCP resistance and R_B is back MCP resistance. R_M is the matching resistance that we place in parallel to front MCP to reduce the effective resistance on one side of the stack. We use R_M=$74M\Omega$.

3.6 Acquisition system

3.6.1 FASTER (Analog to Digital)

Before the begining of my thesis, the data acquisition was done using standard TDC and QDC modules from CAMAC and VME based systems. At the begining of my thesis it has been replaced fully by a digital FPGA based acquisition system called FASTER (Fast Acquisition System for Nuclear Research). FASTER is a complete digital acquisition system, developed indingenously in the Laboratory of Corpuscular Physics (LPC Caen) [109]. It aims to provide a re-programmable/re-configurable and modular digital acquisition system, for nuclear physics and interdisciplinary experiments using one to many channels of measurement. 15 channels were used in this experiment, it is enough to connect each detector, via a pre-amplifier, to the FASTER acquisition.

This system selects the information in real time, process it followed by sorting, grouping and visualizing it online, while recording it on disk for post experiment analysis (Figure C.1). The online visualization is carried out using RHB histogram Builder (ROOT histogram Builder) software, also developed by the LPC's FASTER team. It is based on the ROOT (Data analysis software) software developed by CERN (Conseil Europeen pour la Recherche Nucleaire). More technical details about FASTER and explanation of various parameters are described in the Annex C.

3.6.2 Internal clock, Trigger window

One of the most important detail about this acquisition system is its internal clock. All the independent SYROCO_ AMC motherboards are synchronized using a RF module to the main CPU of the FASTER crate. The t_0 timing signal is generated by the main CPU and all the mother FPGA's correspond to it (See figure 3.6.2). The t_0 is responsible for the synchronization of all the daughter cards to there respective mother boards and also for parallel communication between all motherboards to the main CPU of faster.

Now we will discuss how the "group decision module" works in FASTER. This module

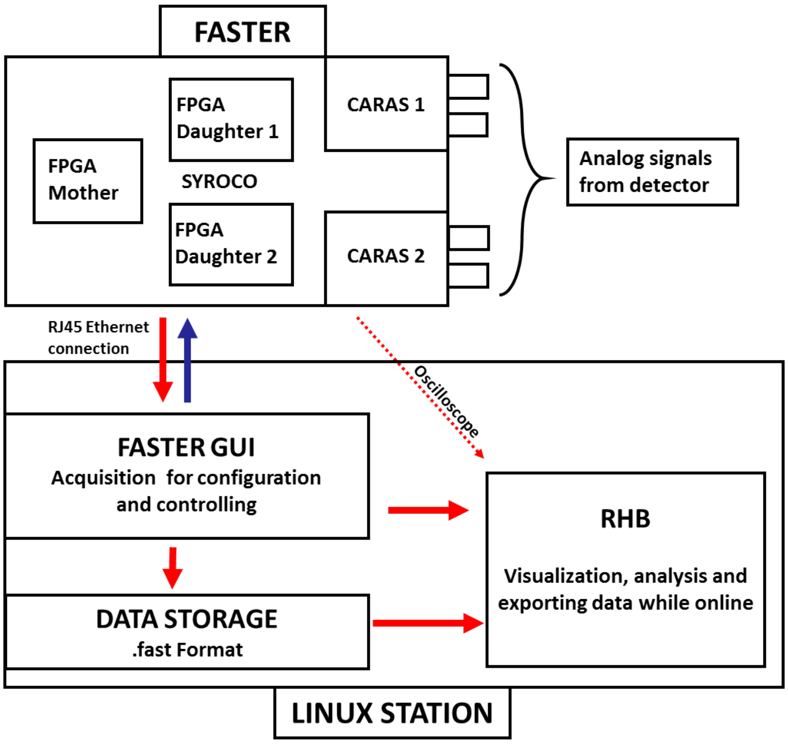

Figure 3.6.1 : *Block diagram showing of FASTER Acquisition system*

is divided into two parts: Trigger and Merger. The trigger panel can define conditions that triggers a group. We can use combinations of data labels (defined in configuration file of the FASTER acquisition system) along with the boolean expressions between different input channels in a given acceptance time window. In our experiment the trigger was defined as a coincidence between projectile and ion detector in a window of 10 μs. The projectile and ion signals are referred as T_ PROJ and TG_ DI on figure 3.6.2. Since we use a boolean AND gate it compel FASTER to make a group only when both the MCP signals (projectile and recoil ion) are present in the main window, otherwise it rejects the group. In our case the START of an event group is from the arrival of projectile MCP signal upon its arrival a coincidence window of about 10μs starts. During this window all the signals from each channel are collected, and if and only if there is at least one MCP signal from ion detector then only the group data is saved under one event. The figure 3.6.2 shows the trigger scheme of FASTER acquisition system used during our experiments.

In the merger part of the group decision module, each trigger creates a data group with a set of followers, which could be every channel of the ion and projectile MCP signals. There is also a feature of "Before Trigger Window" and "After Trigger Window", which can be used to extend the reach of data selection for a particular event.

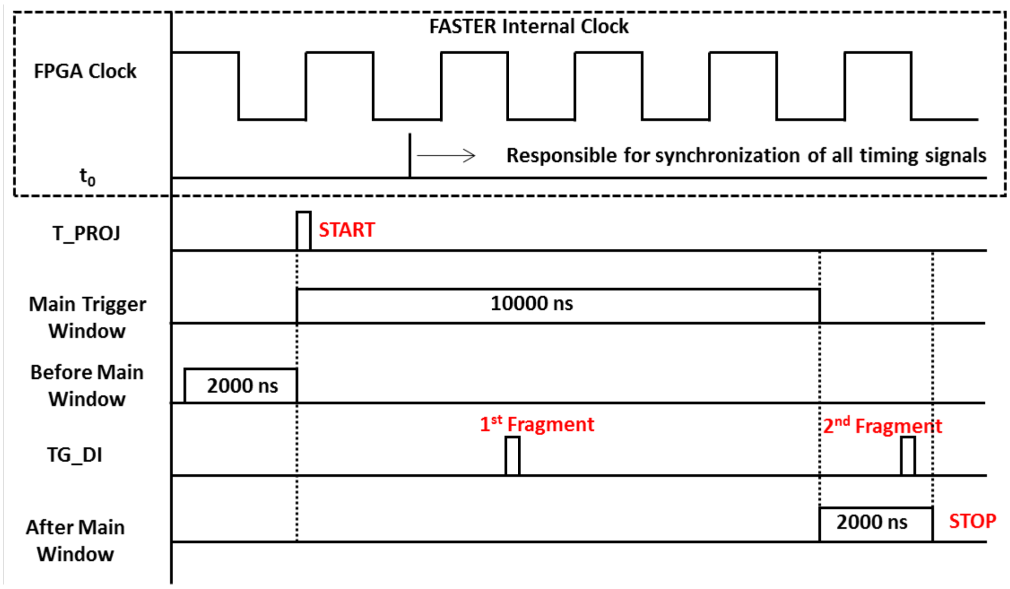

Figure 3.6.2 : *Trigger scheme for data selection available from FASTER*

3.7 Energy calibration

The experimental measurement of the intermolecular bond length in clusters using Coulomb explosion imaging technique requires a precise KER calibration. For a precise KER measurement both time and position calibration are needed because the three dimentional momemtum vector of each ion is deduced from its TOF and impact position of the detector. From the literature (see Chapter: Context), we know that the expected intermolecular distances in CO dimer (R_{CO-CO}) measured in Ford's paper are: R (O - bonded) ≈ 3.96 Å, R (C - bonded) ≈ 4.37 Å [30].

The approximate variation in both geometries is $\frac{\Delta R}{R} \approx 10\%$. Similarly, the corresponding variation in KER values for both the shapes is also expected to be about 10 %. This implicate that the distinction between both shapes is only possible if the absolute precision on the KER measurements is better than 10%.

3.7.1 TOF calibration

In our acquisition the TOF calculation is done using: $TOF_{acq} = T_{STOP} - T_{START}$, where T_{STOP} and T_{START} are the time of arrival of the recoil ion and projectile on their respective detectors. Figure 3.7.1 is a raw TOF spectrum observed from experiment with 135 keV Ar^{9+}. In the extreme left of TOF spectra a single sharp peak can be observed. This arises from photons emitted by the projectile following multiple electron capture on the molecular target. We can compare the position of this photon peak with the propagation time of the projectile from the collision region to its detector:

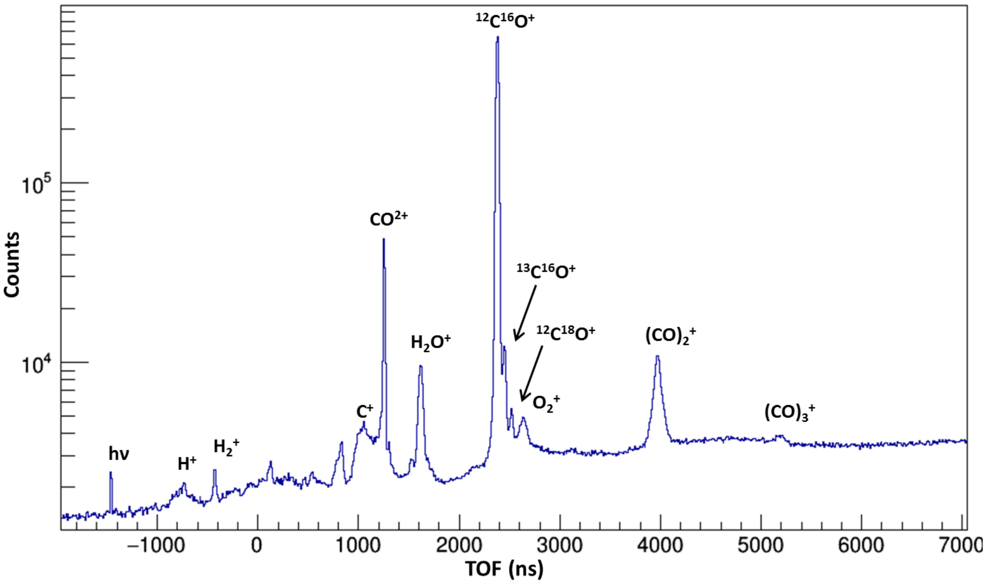

Figure 3.7.1 : *Time of flight spectra from the collision of 135 keV Ar^{9+} with CO and its clusters.*

$$\Delta t = \frac{d}{v} = \frac{1.25}{806600} s = 1550 ns,$$

where d is the distance between the collision region and the projectile detector and v is the velocity of 135 keV Ar^{9+} projectile calculated using equation 3.4.2. For rest of the ions in the TOF spectrum, each have a finite broadening due to initial momentum spread in the collision region. The sharp peaks are from non-dissociating molecular ion and the broad peaks are resulting from dissociation of the target in several charged fragments.

The photon peak position in the negative part of TOF spectra is very close to the expected arrival time of projectile from collision region to its detector. The precise value of the peak position $T_{h\nu}$= -1458 ns and thus defines our first calibration parameter in equation 3.7.1, and is used to determine actual TOF of recoil ions, hence forth $TOF = TOF_{acq} + T_{h\nu}$. The constant B in equation 3.7.1 is exactly equal to $T_{h\nu}$ if neglecting the TOF of the photons over the length of the spectrometer (L=10 cm ,TOF of photons =0.3 ns).

Moreover using four other well identified TOF peaks, the constant parameter A is determined by linear fitting using the calibration equation. Figure 3.7.2 shows the linear fitting of the TOF data from our experiment with CO jet.

$$TOF = A\sqrt{\frac{m}{q}} + B \qquad (3.7.1)$$

For a spectrometer of length L (L_{0c} used in analysis program) and a homogeneous electric field E, the parameter A is given by the following relation: $A = \sqrt{\frac{2L}{E}}$ (neglecting the post acceleration region). Using $E = 4000$ V/m and $L = 0.1$ m the theoretical value of constant A is 7.072×10^{-3} $s\sqrt{C/kg}$. The TOF calibration gives $A = 725.4083$ $ns.\sqrt{eV/amu}$, which converts

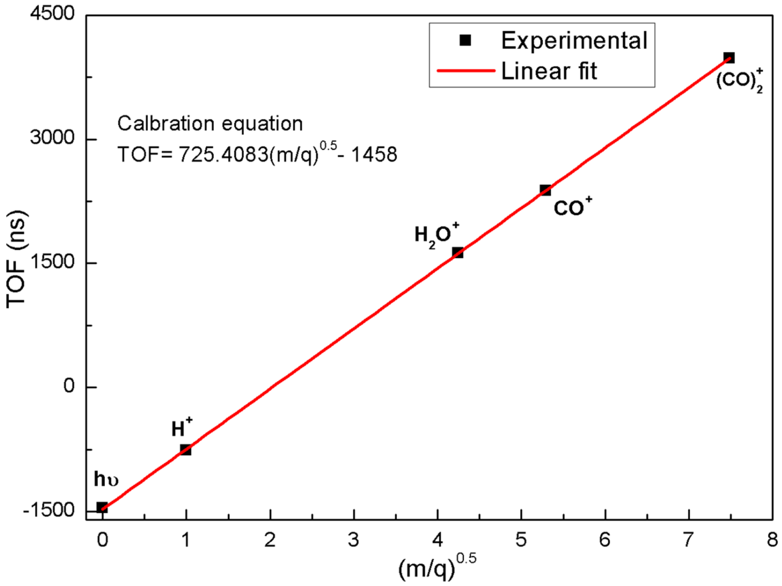

Figure 3.7.2 : *Graph showing the linear relation between TOF and* $\sqrt{\frac{m}{q}}$ *as well as the result of a linear fit using equation 3.7.1.*

to $A = 7.122\text{x}10^{-3}\ s\sqrt{C/kg}$ in SI (International system of units) units. The little difference between the theoretical value and the experimental value is mainly due to inconsideration of post acceleration region. The corrected value of A accounting for the post acceleration region is detailed in annex A. This corrected value is found to be A'= 7.125x10^{-3} $s\sqrt{C/kg}$ which is in very good agreement with the experimental value. Using the experimental value of A the homogeneous electric field E= 3945 V/m for an extraction length of L_{0c}= 100 mm is determined.

3.7.2 Position calibration

Since the output from delay line anodes is a timing signal, which is the propagation time from the impact position to the respective ends of the wire, the position is defined as the difference between these two timing signal. As explained in section 3.5.1, this propagation time is to be converted from ns to mm, for which a coefficient C_{DLD} is used. The value of C_{DLD} has to be measured precisely as it has a large contribution to the uncertainty on KER measurement.

A first approximate value of C_{DLD} can be obtained using the image of the recoil ion detector from the collision of system $(CO)_n + Ar^{9+}$ and knowing the active diameter of the MCP. The active diameter of ion MCP detector is around 81.25 mm [84]. Then we use the projection of slices on Y and Z axis to measure the corresponding propagation time (see figure 3.7.3).

$$C_{DLD} = \frac{81.25}{156} mm/ns = 0.52 mm/ns \tag{3.7.2}$$

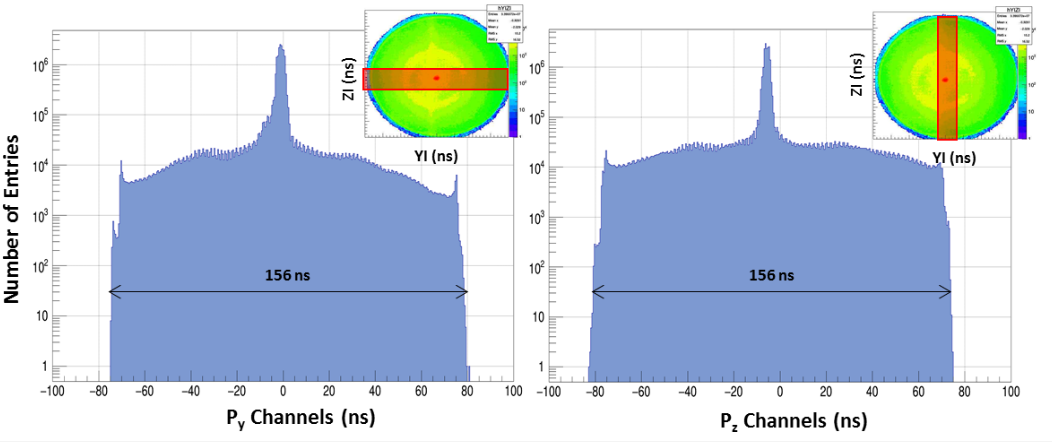

Figure 3.7.3 : *Projection of the time difference between each end of the wires* T_Y=$T_{Y2}-T_{Y1}$ *and* T_Z=$T_{Z2}-T_{Z1}$ *position from ion detector image. Slices for both projections on the detector image are shown in the upper right corner of respective graphs.*

Although the above mentioned method gives an approximate value of C_{DLD}, we will describe a more precise calibration method discussed further.

This second method for calculating the coefficient uses the grid placed in front of the ion MCP (refer figure 3.5.2). The presence of this grid is clearly visible on the image of the ion detector (see figure 3.7.4). Then a projection of both Y and Z axis of the ion detector image are plotted. It results in a sequence of intense peaks corresponding to the hole between two consecutive wires of the grid.

Figure 3.7.4 shows the projection on Z axis of the image of the ion detector, the data points are represented in blue and all the fitted peaks are in red. For fitting the peaks a set of Gaussian functions with same FWHM of 0.28 ns have been used. Then we calculate the difference between the central position of each peak.

In figure 3.7.5 the corresponding distribution is shown and the centroid of this distribution at 0.69 ns corresponds to the mean propagation time between two grid wires. The difference ΔT varies from 0.55-0.85 ns. This variation from the mean value shows that distance between adjacent wires is not constant and varies around 22%. Gaussian fitting of this distribution give the standard deviation around ΔT_{mean} ($\sigma_{\Delta T}$) equal to 0.045 ns. The relative deviation is around: $\dfrac{\sigma_{\Delta T}}{\Delta T_{mean}} = 6.5\%$. We will later discuss the origin of such a large distribution.

The physical distance between two wires has been determined by taking a picture of the entire grid with a standard camera. The grid was still mounted and fixed on its electrode and we used the inner diameter of this electrode for an absolute calibration of the picture. The inner diameter of this electrode is equal to 80 mm ± 0.1 mm. Using imageJ software a profile along the Z axis is performed and the position of each wires is fitted using Gaussian functions. The figure 3.7.6 (top) shows the Z axis profile of this grid. This X-axis of this profile is in the

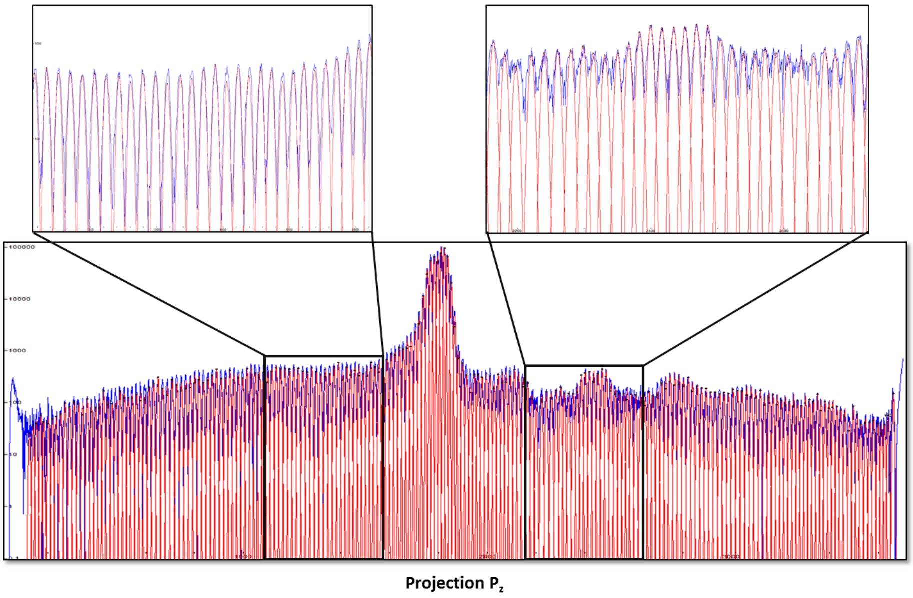

Figure 3.7.4 : *Projection of Z axis of ion detector. On the top, two zooms from different part of the detector are shown and a small distortion can be observed in the right side of image as compared to the left side of the image. The red curve are adjustments using the Gaussian functions.*

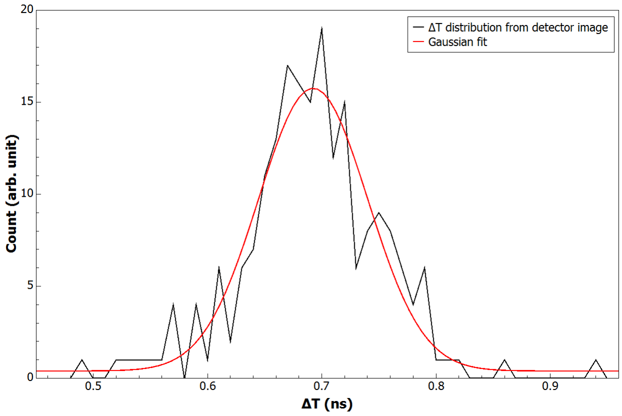

Figure 3.7.5 : *Frequency distribution of time difference between adjacent peaks in the projection of Z position of ion detector.*

pixels, the inner diameter corresponds to 2730 pixels. Using this relation we get our conversion factor for converting pixels in mm i.e. 0.029304 mm/pixels.

All the peaks in this distribution correspond to the physical distance between adjacent grid wires. The frequency distribution of the distance between the centroid of adjacent peaks is shown in figure 3.7.6 (bottom). The mean value is found to be around 0.365 mm and a standard deviation $\sigma_{\Delta d} \simeq 0.0055$ mm. Using these parameters the relative deviation is: $\frac{\sigma_{\Delta d}}{\Delta d} = 1.5\%$.

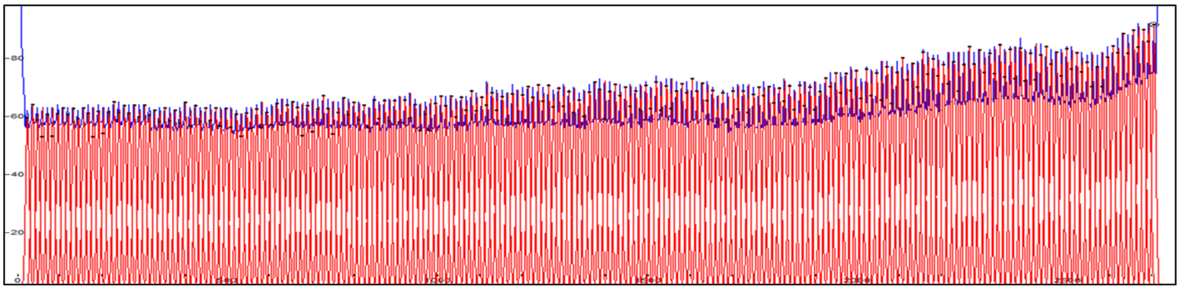

Z axis profile of grid

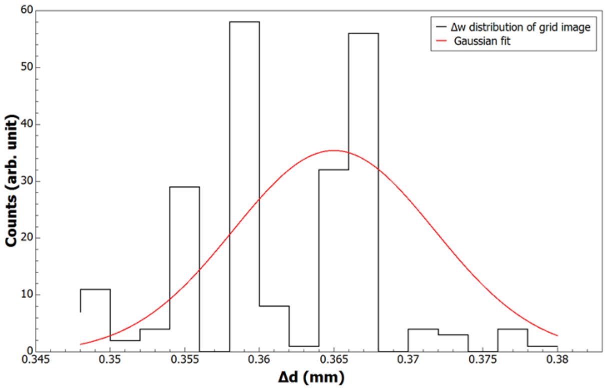

Figure 3.7.6 : *Top: Profile of grid wires from a picture of ion grid, and all the peaks have been fitted with a Gaussian function. Bottom: Frequency distribution of distance between adjacent wires* (Δd) *is presented.*

This value is significantly lower than the relative deviation on the propagation time $\frac{\sigma_{\Delta T}}{\Delta T_{mean}} = 6.5\%$. This more probably come from a non linearity of the position reconstruction because of a non constant spacing between the wires of the delay line anodes. This can be seen in figure 3.7.4, the peaks are distorted on the right side of the projection as compared to the left side. The Y position of Grid wire also had been studied similarly and the conclusion is similar for both the Y and Z anode wires.

Finally for calculating the position calibration coefficient C_{DLDZ} for Z position, we have used the mean value of both ΔT and Δd. Therefore, $C_{DLDZ} = \frac{0.365}{0.69} = 0.5298 \pm 0.006 mm/ns$. Similarly, $C_{DLDY} = 0.53 \pm 0.0055 mm/ns$. Note that these values are in agreement with the previously determined value using the global size of the detector.

3.7.3 Comparative calibration through the role of electric field, extraction length and C_{DLD}

From the previous two sections, we detemined the value of E= 3945 V/m , L_{0c}= 100 mm and C_{DLD} = 0.53 mm/ns using TOF and position calibration respectively. Primarily the analysis has been performed using these parameters. For precision in measurements a comparative method is employed where, the KER spectra for $CO^{2+} \rightarrow C^{+} + O^{+}$ after collision with Ar^{9+} is compared to previous KER measurement by Lundquist [39]. This reference KER spectra was measured using a coincidence detection of C^{+} and O^{+} ions with a TOF experiment. They used a 200 eV pulsed electron beam with adjustable pulse length of 5-1000 ns as ionizing beam. Inside a differential pumped gas cell, the target CO is ionized with an electron beam. Two MCP detectors are placed $180°$ from each other inside a field free 50 cm long TOF tube for collecting both ions in coincidence. For accurate identification of vibrational states they performed calibration using the deuterium peak. The kinetic energy peak from the dissociation of D_2^{2+} can be measured with an uncertainty of $\pm 50 meV$. Since the ionizing particle in this reference work (electron) and our experiment (LE-HCI) are different, henceforth position of the KER peaks are expected to be similar but the relative intensities are not equal. We use this KER spectra as a reference and compare with our experimental data.

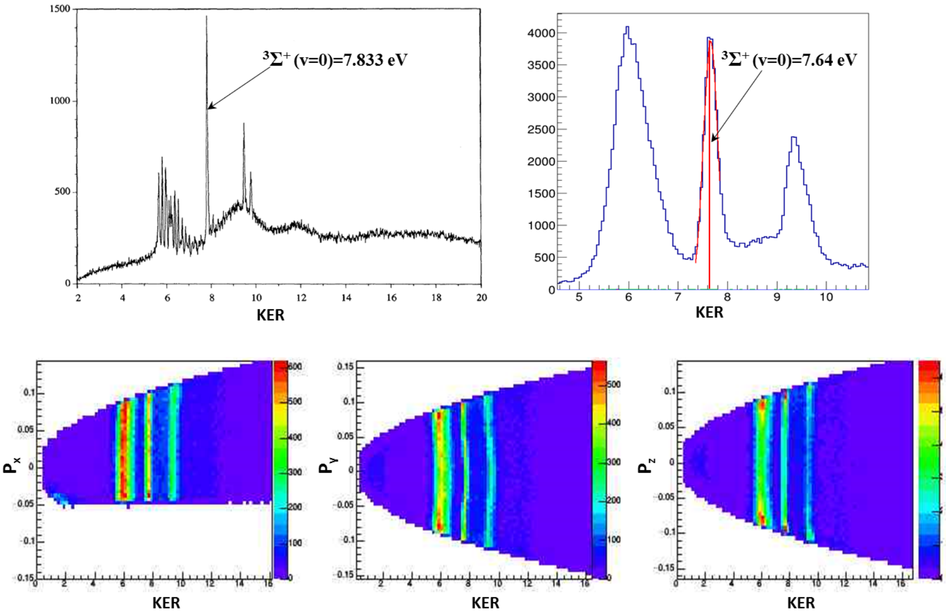

Figure 3.7.7 : *KER of CO^{2+} from Lundquist et al. (Top left) [39], KER of CO^{2+} using the E , L_{0c} and C_{DLD} from calibration (Top right). Three graphs bottom shows the correlation between KER and 3D momentum of fragments.*

In the KER spectrum from Lundquist et al. the peak at 7.833 eV corresponding to the $^3\Sigma^+(v = 0)$ state is used as the reference because it contains only one vibrational level $(v = 0)$. With our experimental resolution, the two other peaks (around 6 eV and 9.5 eV) is the superposition of several vibrational levels and the direct comparison is difficult. From our primary analysis we obtained the KER spectra in figure 3.7.7 (top right) and the mean position of the peak corresponding to $^3\Sigma^+(v = 0)$ is at 7.64 eV. The deviation from the reference peak is 7.83-7.64 = 0.19 eV = 190 meV with the relative error of about 2.5%, which is upto 4 times the uncertainty defined by Lundquist et al. In figure 3.7.7, the bottom three graphs showing the correlation between KER of CO^{2+} and 3D momentum of fragments are used to verify calibration parameters. As the KER is not expected to depend on the initial orientation of the target, straight vertical lines is the signature of a optimal TOF and position calibration. Here the vertical lines are slightly curved showing that the calibration can still be improved.

Following the calibration parameter A=$\sqrt{\frac{2L_{0c}}{E}}$ in equation 3.7.1, the value of E and L_{0c} are adjusted as well as the position calibration parameters for both Y and Z axis. While tuning all these parameters we compare the peak position and qualitatively improve the shape of the straight lines in KER vs 3D momentum graphs.

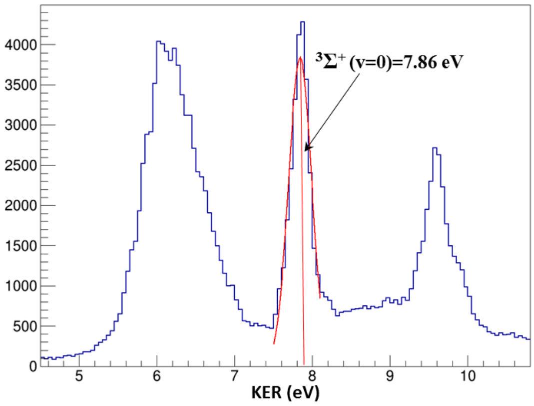

Figure 3.7.8 : *KER of CO^{2+} after the using the finally tuned energy calibration parameters.*

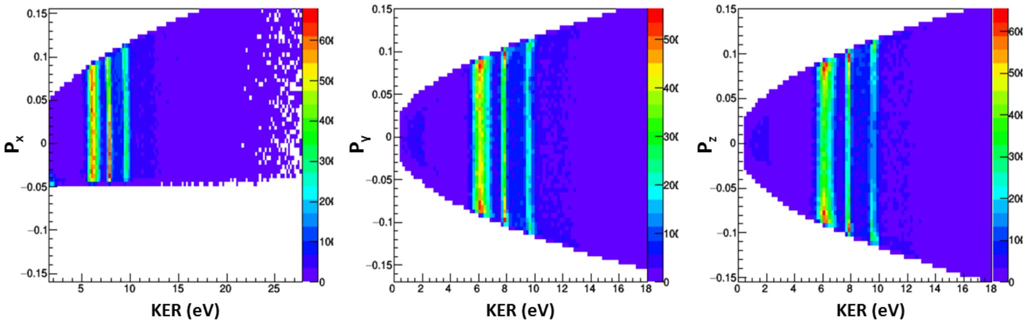

Figure 3.7.9 : *Correlation between the KER and the 3D momentum vector of the fragments in dissociation of CO^{2+}, Straight line in the graph indicates that the KER is not dependent on the initial orientation of the target.*

The optimal parameters have been found to be: E=3925 V/m, (L_{0c}) =99.65 mm, C_{DLDY} = 0.544 mm/ns and C_{DLDZ} = 0.536 mm/ns. The figure 3.7.8 and 3.7.9 show the corresponding spectra obtained using these parameters. The position of $^3\Sigma^+(\upsilon = 0)$ peak at 7.86 eV (relative error $\simeq$ 0.4%) in figure 3.7.8 is close to the reference KER spectra and it is in the range of uncertainty defined in Lundquist et al.. The three 2D graphs representing correlation between KER and 3D momentum in figure 3.7.9, shows now "straighter" lines than with previous parameters.

The tuning of these calibration parameters does help in improving our absolute KER calibrations, but on the other hand it also highlights the limitation of the spectrometer. The remaining slight distortion in the KER vs 3D momentum spectra mainly originates from small inhomogeneity of the extraction field. This inhomogeneity is probably due to an irregular spacing between spectrometer plates. As a conclusion, we show that our calibration procedure ensure an absolute KER calibration better than 2%. Such a good absolute KER precision will allow the identification of several predicted intermolecular distances in N_2 and CO clusters.

Fragmentation Dynamics of N_2 and CO dimers

4

Contents

Atomic and molecular clusters fragmentation has been of a great interest in the recent years along with improvement in imaging techniques. This chapter is mainly devoted to the discussion of 2-body and 3-body fragmentation of N_2 and CO dimer's from the collision with 15 qkeV Ar^{9+} projectile. We will focus on the fragmentation of the dimer's trications: $(N_2)_2^{3+} \rightarrow N^+ + N^+ + N_2^+$ and $(CO)_2^{3+} \rightarrow C^+ + O^+ + CO^+$. However, a quantitative description of the 3-body fragmentation dynamics requires the knowledge of the intermolecular distance because this distance fixes the strength of the electric field experienced by the molecular dication due to the presence of the other singly ionized neighbour molecule. Thus the first section is devoted to the measurement of the dimer bond length using the 2-body channels.

4.1 2-Body Coulomb explosion of $(N_2)_2^{2+}$ and $(CO)_2^{2+}$ dication

In this section the kinetic energy release (KER) in the dissociation of $(N_2)_2^{2+}$ and $(CO)_2^{2+}$ is discussed. The 2-body channels from $(N_2)_2^{2+} \rightarrow N_2^+ + N_2^+$ and $(CO)_2^{2+} \rightarrow CO^+ + CO^+$ results from single electron capture on each site of the dimer. The inter molecular distance in the dimer is derived from these KER values and it fixes the strength of electric field in the dimer's 3-body dissociation channel [110].

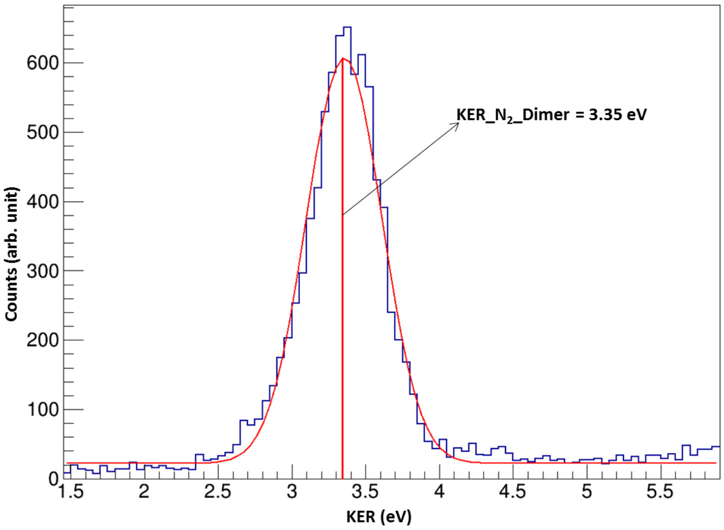

Figure 4.1.1 : *KER spectra of $(N_2)_2^{2+}$ from collision with 15 qkeV Ar^{9+}*

The KER (sum of kinetic energy of each fragment) spectrum of $(N_2)_2^{2+} \rightarrow N_2^+ + N_2^+$ is shown in figure 4.1.1. Here we use the KER spectra of the 2-body channel to deduce the intermolecular distance $R_{(N_2)_2}$ of the N_2 neutral dimer. This distance is of the order of 4Å and the potential energy curve of this dissociative state can be approximated by a pure Coulomb

curve. The KER and the $R_{(N_2)_2}$ follow the relation:
$KER = \frac{1}{4\pi\varepsilon_0} \cdot \frac{q_1 q_2}{R_{(N_2)_2}}$.
Figure 4.1.1 shows the KER spectra of the 2-body dissociation channel (A), here we found an average KER value 3.35 eV from this distribution. Using the above relation, the equilibrium $R_{(N_2)_2}$ is determined to be 4.29 Å. The width of this distribution σ_{KER} is measured around 0.3 eV which is about 10% of average KER value. As $KER \propto \frac{1}{R}$ the width of the $R_{(N_2)_2}$ distribution ($\sigma_{R_{(N_2)_2}}$) is also about 10% of 4.29Å i.e. 0.4 Å. The value of $\sigma_{R_{(N_2)_2}}$ results mainly from the vibrations along the Van der Waals bond of dimer. The events occurring in the higher and lower part of the KER distribution in figure 4.1.1 are part of background from false coincidence. This background has been subtracted during curve fitting of our KER peak.

Similar to the case of $(N_2)_2^{2+}$, the KER of $(CO)_2^{2+} \rightarrow CO^+ + CO^+$ is shown in the figure 4.1.2 below. The average KER from this channel is measured to be 3.18 eV. This energy is similarly shared between both fragments equally as in the case of $(N_2)_2^{2+}$ dication. Assuming a pure Coulomb explosion, the inter molecular distance of $(CO)_2^{2+}$ is about $R_{(CO)_2} \simeq$ 4.52 Å. With the calibration of previous chapter we are confident in the measured KER values for $(CO)_2^{2+}$. From the previous theoretical and experimental work on the geometry of CO dimers, the $R_{(CO)_2}$ values corresponding to C-bonded slipped anti-parallel (4.4 Å) and C-bonded T-shaped (4.42 Å) are the one close to our measurement. Further discussion about the geometry is done in the next chapter.

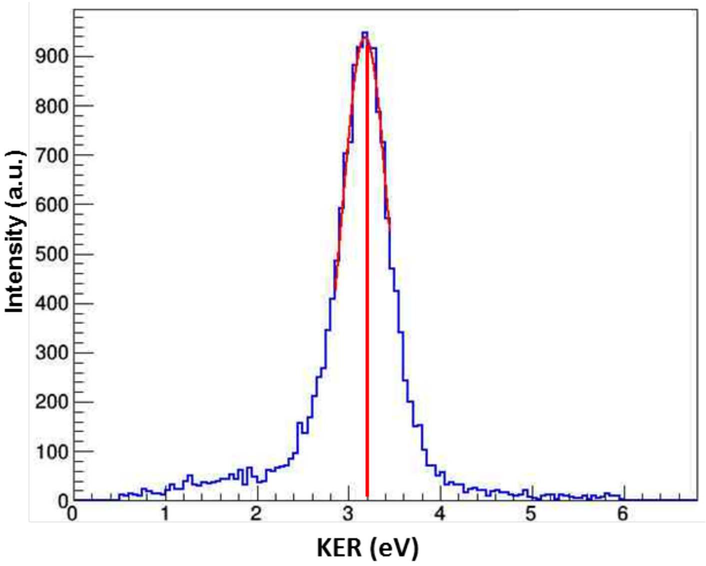

Figure 4.1.2 : *KER spectra of $(CO)_2^{2+}$ from collision with 15 qkeV Ar^{9+}*

Using these equilibrium intermolecular distances of the N_2 and CO dimers, we will now discuss the fragmentation dynamics of their trication's in 3-body channel. In this chapter we will only use these inter molecular distances to study and compare with 3-body dissociation;

further discussions about geometry are done in the next chapter.

4.2 3-body Fragmentation of $(N_2)_2^{3+}$ and $(CO)_2^{3+}$ trication

The analysis of the 3-body dissociation channel of both $(N_2)_2^{3+}$ and $(CO)_2^{3+}$ will be discussed in this section. Firstly we will look into the fragmentation channel $(N_2)_2^{3+} \rightarrow N_2^+ + N^+ + N^+$ highlighting the features of this dissociation mechanism. A specific role of ionic environment in this 3-body dissociation will be introduced and discussed later in this section. In the second part the fragmentation dynamics of 3-body channel $(CO)_2^{3+} \rightarrow CO^+ + C^+ + O^+$ is discussed.

4.2.1 3-body dissociation of $(N_2)_2^{3+}$

4.2.1.1 Dissociation mechanism

Dissociation mechanism in a 3-body channel could be identified by looking at the kinetic energy shared between all the fragments. Identifying the pathway involved in the dissociation can be done through the kinetic energy of the non dissociating N_2^+. The figure 4.2.1 shows the kinetic energy spectrum of N_2^+, the distribution is maximum between 0 and 2.5 eV. Most of the events correspond to a direct fragmentation in which all the three fragment are emitted simultaneously. The total initial potential energy is shared as kinetic energy among the N^+ ions and non dissociating N_2^+ molecular ion. The distance between the non dissociating N_2^+ and both N^+ is relatively larger than the covalent bond length. This is the reason why the N_2^+ spends a relatively short amount of time inside the electric field of N_2^{2+} dication thus acquiring a smaller amount of kinetic energy. This qualitative explanation depends on the initial three dimensional geometry of the dimer and seems to show that the molecules are not aligned with the dimer axis (see more details in the next chapter).

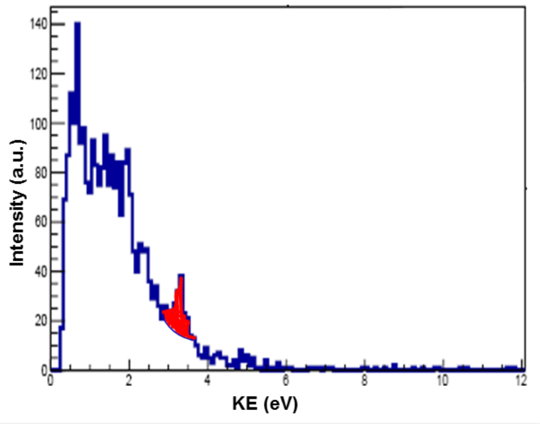

Figure 4.2.1 : *kinetic energy spectra of N_2^+ from $N_2^+ + N^+ + N^+$ channel after $(N_2)_2$ collision with 15 qkeV Ar^{9+}*

In the above spectra a small relatively narrow peak around 3.35 eV is observed. This peak correspond to a sequential process where the weak bond or van der Waals bond breaks before the covalent bond. This sequential process will be discussed more in detail in the case of CO dimer. Since this contribution is less than 5%, the direct fragmentation is by far the dominant dissociation process for this channel proving that there are not many metastable states involved in this system as the peak at the position of pure sequential process is very low in intensity.

4.2.1.2 Effect of a charged environment on the dissociation of N_2^{2+} dication

This is the case of the direct 3-body fragmentation channel in $(N_2)_2^{3+} \rightarrow N_2^+ + N^+ + N^+$ trication, where both inter and intra molecular bonds are exploding. The dissociation consists in the cleavage of one covalent bond in N_2^{2+} molecular dication and Van der Waals bond between both molecules. For comparing the dissociation of N_2^{2+} from a monomer and inside a dimer we used the KER spectrum from both channels. In figure 4.2.2 (top) the KER spectrum of $(N_2)^{2+} \rightarrow N^+ + N^+$ dication is observed showing various transient states. We compared this spectra with the work of Lundqvist to compare and identify these transient states from nitrogen dication [41]. Two major peaks (peak no. 2 and 3) at 7.8 eV and 10.3 eV are identified as corresponding to $D^3\Pi_g$ and $D^1\Sigma_u^+$ molecular orbital. In the beginning of the peak 2 there is a shoulder peak which corresponds to $A^1\Pi_u$ and peak 4 corresponds to other various high excited states.

For the 3-body channel from $(N_2)_2^{3+}$ trication the KER spectrum is shown in figure 4.2.2 (bottom). The peak for this channel starts to appear after 10 eV and several peaks are observed corresponding to various excited states. Comparing the peak position and shape of both spectra, it is clear that there is an additional energy which shifts the KER spectra of $(N_2)_2^{3+}$ but the shapes are almost the same as for $(N_2)^{2+}$. The difference in the relative intensities with respect to peak 2 in both KER spectra can be explained because of the presence of non dissociating N_2^+ inside a dimer. Due to thermal agitation (from vibrational motion of the two molecules) the FWHM of the peaks in dimers trication channel is increased by around 0.125 eV. The energy shift between KER spectra of $(N_2)_2^{3+}$ and $(N_2)^{2+}$ is found to be around 6.7 eV. The dissociation of a monomer inside a dimer experience the Coulomb repulsive potential from the neighboring ion N_2^+ which leads to this shift in the KER. The measured shift (ΔKER) in the KER is explained as an additional potential energy provided to the monomer by the neighboring quasi-independent N_2^+ [110]. Assuming the N_2^+ as a point charge located at its centre of mass, then the additional kinetic energy is the repulsive Coulomb energy between N_2^+ and both respective N^+ (see figure 4.2.2 (bottom)). It can be expressed using the equation 4.2.1 below:

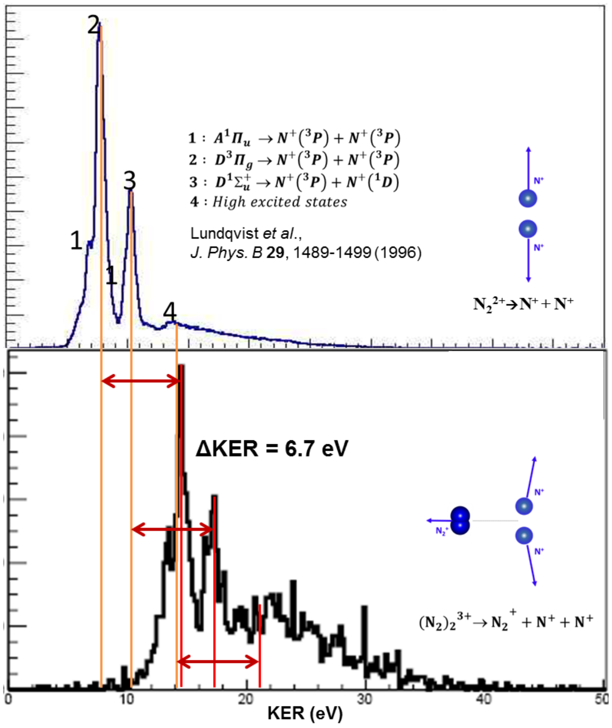

Figure 4.2.2 : *KER spectra of 2-body dissociation of the N_2^{2+} molecular dication and 3-body dissociation of $(N_2)_2^{3+}$ from collision with 15 qkeV Ar^{9+}*

$$\Delta KER = \frac{e^2}{4\pi\varepsilon_0}\left[\frac{m}{R_{N_2^+-N^{m+}}} + \frac{n}{R_{N_2^+-N^{n+}}}\right] \tag{4.2.1}$$

where m=1 and n=1 are the respective charge states of each N^+ ion. For calculating the distances $R_{N_2^+-N^{m+}}$ and $R_{N_2^+-N^{n+}}$, we assume the dissociating molecule to be perpendicular to the dimer bond axis. Using equilibrium bond length of N_2 i.e. $R_{N-N} = 1.1$ Åand $R_{e\_N_2} = 4.3$ Å (see section 4.1);

$$\Delta KER \cong 3.32 * (m+n) = 6.64 eV. \tag{4.2.2}$$

The theoretical additional KER value is closely in agreement with the observed experimental value of 6.7 eV. This shift in the kinetic energy or additional potential energy is shared between all the three ions in this channel. From figure 4.2.1 we see that a small portion of energy is transfered to N_2^+ ion and the rest of it is shared among the N^+ ions [110].

4.2.2 3-body dissociation of $(CO)_2^{3+}$

In this section we will focus on the heteronuclear diatomic CO dimers. Earlier in this chapter we have already discussed the KER spectra of $(CO)_2^{2+}$ dication to give an average inter molecular distance. Capturing one more electron from one site of the dimer dication will leave $(CO)_2^{3+}$ trication to undergo 3-body fragmentation via the $(CO)_2^{3+} \rightarrow C^+ + O^+ + CO^+$ channel. Firstly the dissociation mechanism for this channel will be discussed and evidence of different pathways will be explained using the Newton diagrams. Post to this discussion, an identification of short lived and long lived states of the CO^{2+} dication by different dissociation pathways is performed.

4.2.2.1 Dissociation mechanism

The channels required to study different dissociation mechanisms are:
1) $(CO)_2^{2+} \rightarrow CO^+ + CO^+$ and
2) $(CO)_2^{3+} \rightarrow CO^+ + C^+ + O^+$.
We employ the same method as for N_2 dimers by looking at the kinetic energy of the non dissociating CO^+ in channel 2. The figure 4.2.3 shows the kinetic energy spectrum obtained for CO^+ and unlike the case of N_2 dimer, two different contributions can be seen corresponding to two very well defined peaks. The first one with low energy is because of instantaneous 3-body dissociation of all the three ions which we already saw in previous dimer $((N_2)_2)$. This process is referred to as "direct fragmentation". The second peak centered around 3.2 eV correspond to a pure Coulomb dissociation of $CO^+ + CO^{2+}$ channel followed by a second step where the CO^{2+} dissociates. This is called sequential fragmentation. The two steps of sequential fragmentation are as follows:
step 1: $(CO)_2^{3+} \rightarrow CO^+ + CO^{2+}$,
step 2: $CO^+ + CO^{2+} \rightarrow CO^+ + C^+ + O^+$.
This is indicative of the presence of various long lived metastable states in the $(CO)^{2+}$ molecular dication. In our experimental conditions the ratio of sequential to direct events is almost equal to 1.

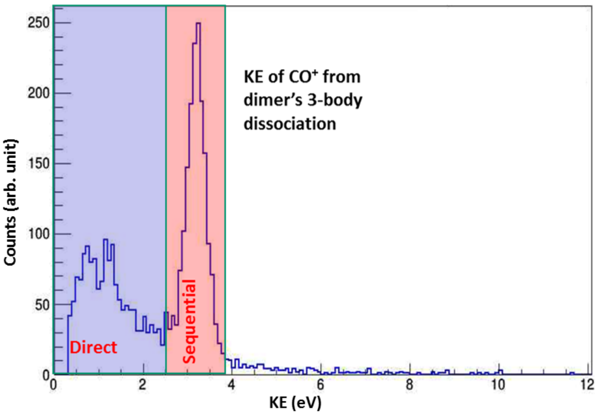

Figure 4.2.3 : *Kinetic energy of CO^+ in the 3-body dissociation of the $(CO)_2^{3+}$ trication from collision with 15 qkeV Ar^{9+}*

In the case of channel 1, both molecular ions share equal energy after fragmentation.

Therefore the kinetic energy of each $(CO)^+$ is half of 3.18 eV (see section 4.1) which is equal around 1.59 eV. Removing one extra electron from one site of the dimer followed by pure Coulomb explosion will give twice the energy to the singly charged $(CO)^+$. The energy gained during step 1 from the repulsive interaction between both singly and doubly charged CO can be verified theoretically using:

$$KE_{CO^+} = \frac{1}{2} \cdot \frac{e^2}{4\pi\varepsilon_0} \cdot \frac{q_1 q_2}{R_{(CO)_2}}.$$

q_1=1 and q_2=2 are the charges on the corresponding CO^+ and CO^{2+}ions with $R_{(CO)_2}$ is 4.52 Å (see section 4.1). From above we get the kinetic energy gained by $(CO)^+ = 3.18$ eV. This is exactly where we have our sequential peak for channel 1. To look further in both the dissociation mechanisms Newton diagram comparisons are done below.

4.2.2.2 Direct and sequential: Newton diagram comparison

Both pathways can be easily separated by a selection on the kinetic of the non-dissociating CO^+ (see figure 4.2.3). The whole low energy part where 0.3 eV $\leq$ kinetic energy $\leq$ 2.5 eV belongs to the events occurred in case of direct fragmentation. We restrict the kinetic energy of CO^+ from 3-body channel below 0.3 eV to avoid the false coincidence caused by ionization of monomer targets. For sequential fragmentation all the events under the peak from 2.8 eV $<$ kinetic energy $<$ 3.8 eV are classified as sequential fragmentation. Even if there are few direct events which fall under the sequential peak as background, we used these filters and then plotted Newton diagram to show the evidence of both processes.

Newton diagram is the representation of the correlated momenta of the fragment ions in the dimer frame of reference. Different dissociation mechanisms produce distinct features in the Newton diagram. In this plot, the momenta of the C^+ and O^+ fragments are plotted with respect to the CO^+. The latter is represented as a vector along the x-axis, while the momenta of other fragments are represented in the x,y plane. We arbitrary choose to place the momentum of O^+ in the upper part of the graph (y>0) and similarly the momentum of C^+ in the lower part of the graph (y<0).

The Newton diagrams associated to the direct and sequential processes are shown in figure 4.2.4 for the 3-body dissociation of the $C^+ + O^+ + CO^+$ channel. Here, the direction of the momentum of the non dissociating CO^+ is taken as the reference.

For direct fragmentation (figure 4.2.4a), two bright red spots can be seen representing the momenta of both atomic ions, these point represent the instantaneous dissociation of CO^{2+} dication along with the breakup of the van der Waals bond. The position of these intense spots depends on the initial geometry of the CO dimer and indicates that the angle between dissociating covalent and van der Waals bonds is close to 90° (see next chapter). In this case, as we have discussed before (see section 4.2.1.1) the maximum energy is being shared between the atomic ions since they are closer to each other than the neighboring non dissociating CO^+.

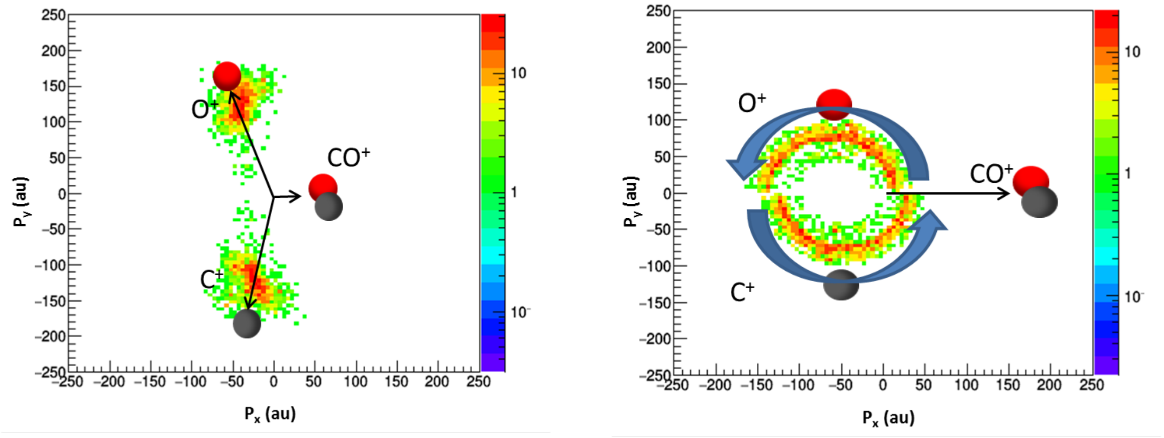

(a) *Direct fragmentation*

(b) *Sequential fragmentation*

Figure 4.2.4 : *Newton Diagram for $C^+ + O^+ + CO^+$ channel with CO^+ as reference*

Therefore, the CO^+ stays for a minimum time in the potential field of O^+ and C^+ ions. This is the reason why the peak in the low energy part of kinetic energy of CO^+ corresponds to direct fragmentation. In figure 4.2.4b, an almost round (consisting two semi circular arcs) is observed which is a pictorial representation of sequential fragmentation. Note that it is only valid if the CO molecule are not obliged with the dimer axis. In the step 1 the pure Coulomb explosion occurs, where both the molecular ions propagate away from each other minimizing the effect of the Coulomb potential. During this step the non dissociating CO^+ gains an average kinetic energy of 3.2 eV ranging from 2.8 - 3.8 eV. In the step 1 the CO^{2+} dication has time to rotate randomly in the space depending upon the corresponding lifetime before breaking up via step 2. This random orientation gives the semi circle shaped distribution for both atomic ions which we see in Newton diagram. With both these diagrams we have a clear signature of both mechanisms. In the following section, we will see how we can identify the states involved in the respective mechanism using the KER of this 3-body channel.

4.2.3 Identification of short and long lived states of CO^{2+}

From the previous sections, our data from $(N_2)_2$ and $(CO)_2$ dimers show that upon collision with same projectile both $(CO)_2$ and $(N_2)_2$ trications show distinct respective dissociation mechanism. While in $(N_2)_2^{3+}$ the direct fragmentation is prominent, the $(CO)_2^{3+}$ experience a new pathway through sequential fragmentation. In most of the previous work on the CO^{2+} dication from a monomer, various lower excited states have been identified [36, 39, 42, 49, 51]. Most of these low excited states are metastable with corresponding lifetime varying from few picoseconds (ps) to seconds (s). All these reference work has been performed on the monomer dication only, this gives us an opportunity to compare the proposed states of the monomer dication inside a dimer. To begin with we will present whether the effect of a charged molecular ion in proximity of a dissociating CO^{2+} dication, is similar to the case of $(N_2)_2^{3+}$. Following this, the KER of CO^{2+} dication from monomer in our experiment is compared to the existing data from the literature in [36, 39, 42, 49, 51]. Secondly the states involved in the direct and sequential fragmentation of dimer's trication will be discussed. Finally we will try to categorize the lifetime range of the states involved in both dissociation mechanisms.

4.2.3.1 Role of a neighbouring ion on molecular fragmentation

As in the case of the 3-body channel of $(N_2)_2^{3+}$ a small shift in the total KER from the N_2^{2+} dication's KER is observed, resulting from the additional kinetic energy provided from the Coulomb repulsive interaction between the atomic and molecular ions [110]. Similar effect in the 3-body channel of $(CO)_2^{3+}$ has been observed.

Figure 4.2.5 shows the KER spectra of $(CO)_2^{3+} \rightarrow C^+ + O^+ + CO^+$ from dimer targets (black) and $CO^{2+} \rightarrow C^+ + O^+$ (blue) from monomer targets overlapping each other.

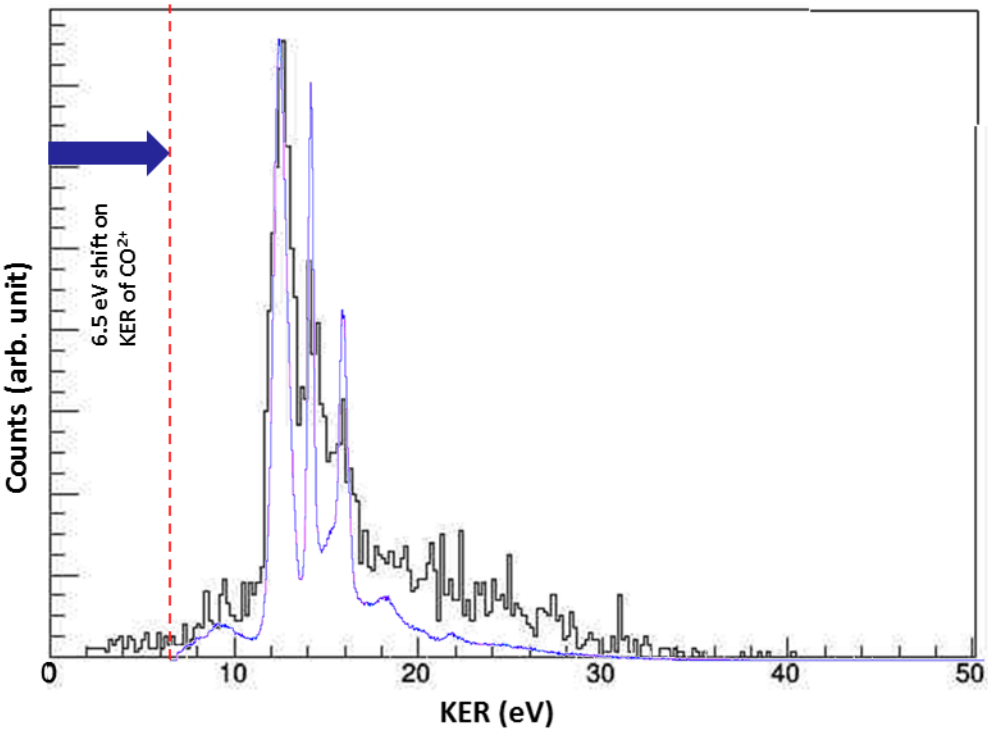

Figure 4.2.5 : *KER spectra of the $CO^{2+} \rightarrow C^+ + O^+$ channel from the monomer dication shifted and overlapped with the KER of $(CO)_2^{3+} \rightarrow C^+ + O^+ + CO^+$ channel from dimer targets in collision with 15 qkeV Ar^{9+}*

The KER of the monomer dication is shifted by a value 6.5 eV to fit with the total KER of dimer trication. The peak positions and shapes are mostly corresponding to each other. The difference in the relative intensities of the peak in KER of $(CO)_2^{3+}$ has decreased, which maybe arises due to the presence of CO^+ modifying few populated states. We measured this shift from experimental data and verify it theoretically using equation 4.2.3, which calculates the kinetic energy gained from the Coulomb repulsion interaction between the CO^+ and the respective C^+ and O^+ atomic ions.

$$\Delta KER = \frac{e^2}{4\pi\varepsilon_0}\Big[\frac{m}{R_{CO^+-O^{m+}}} + \frac{n}{R_{CO^+-C^{n+}}}\Big], \tag{4.2.3}$$

where m and n equals to 1. $R_{CO^+-O^{m+}}$ and $R_{CO^+-C^{n+}}$ are calculated with the assumption of CO^+ being a point charge and the dissociating molecule perpendicular to dimer axis. Using the equilibrium bond length of CO i.e. R_{C-O} = 1.128 Å and $R_{(CO)_2}$ = 4.52 Å (see section 4.1), the theoretical value of ΔKER is found to be 6.32 eV. This theoretical value agrees with our experimental value of 6.5 eV within an error margin of less than 3%. This confirms that the additional kinetic energy contribution to a molecular dication from the presence of a molecular ion inside a dimer is independent of the dissociation mechanism of the 3-body channel. Moreover, the populated states of an isolated monomer dication or in a dimer remain mostly the same in collision with highly charged ions.

4.2.3.2 Direct and sequential fragmentation

In figure 4.2.6 (upper) the KER spectrum of the CO^{2+} dication from monomer is shown. Peak 1 is located around 6 eV, this is an envelop for three lowest energy states $X^3\Pi$, $^1\Sigma^+$ and $^1\Pi$. The peak 2 at 7.86 eV and 3 at 9.53 eV correspond to $^1\Sigma^+$ and $2^1\Sigma^+$ states repectively [39]. Under peak 4 are several higher excited repulsive states. Inside the monomer the major contribution of dissociation for the low lying states ($^1\Pi$, $^3\Pi$, $1^3\Sigma^+$, $1^1\Sigma^+$ and $2^1\Sigma^+$) is through the predissociation via $^3\Sigma^-$ repulsive state and results in relatively long life times (from 1 ps to several seconds) [42].

Most of these lower electronic levels are metastable and the higher vibrational levels are the one which dissociate through tunneling. In the work of Lundqvist and Penent, they have attributed lifetimes to almost all the above mentioned states with maximum of $>$3.8 s to $X^3\Pi$, $\upsilon = 0$. The other states under peaks 1, 2 and 3 are in the range of few ps to ms [36, 39, 49]. However around 30 levels have been mentioned to have a short lifetime of 10^{-14} s range and all these levels lie 4.5 eV above the ground state and could partially correspond to peaks 3 and 4 [36]. As a brief summary that qualitatively, the lower part of the KER spectrum of CO^{2+} is associated to long lived metastable states, where the high energy part corresponds to highly excited state that dissociated very promptly. Clearly, the direct or sequential aspect of 3-body fragmentation in a dimer is governed by the life time of the transient CO^{2+} cation.

Moving from monomer dications to dimers we now consider the KER spectra of $(CO)_2^{3+}$ 3-body channel. The graph in figure 4.2.6 (lower) shows the total KER (black) of this channel. We use the filter from the kinetic energy of the non dissociating CO^+ in figure 4.2.3 to select

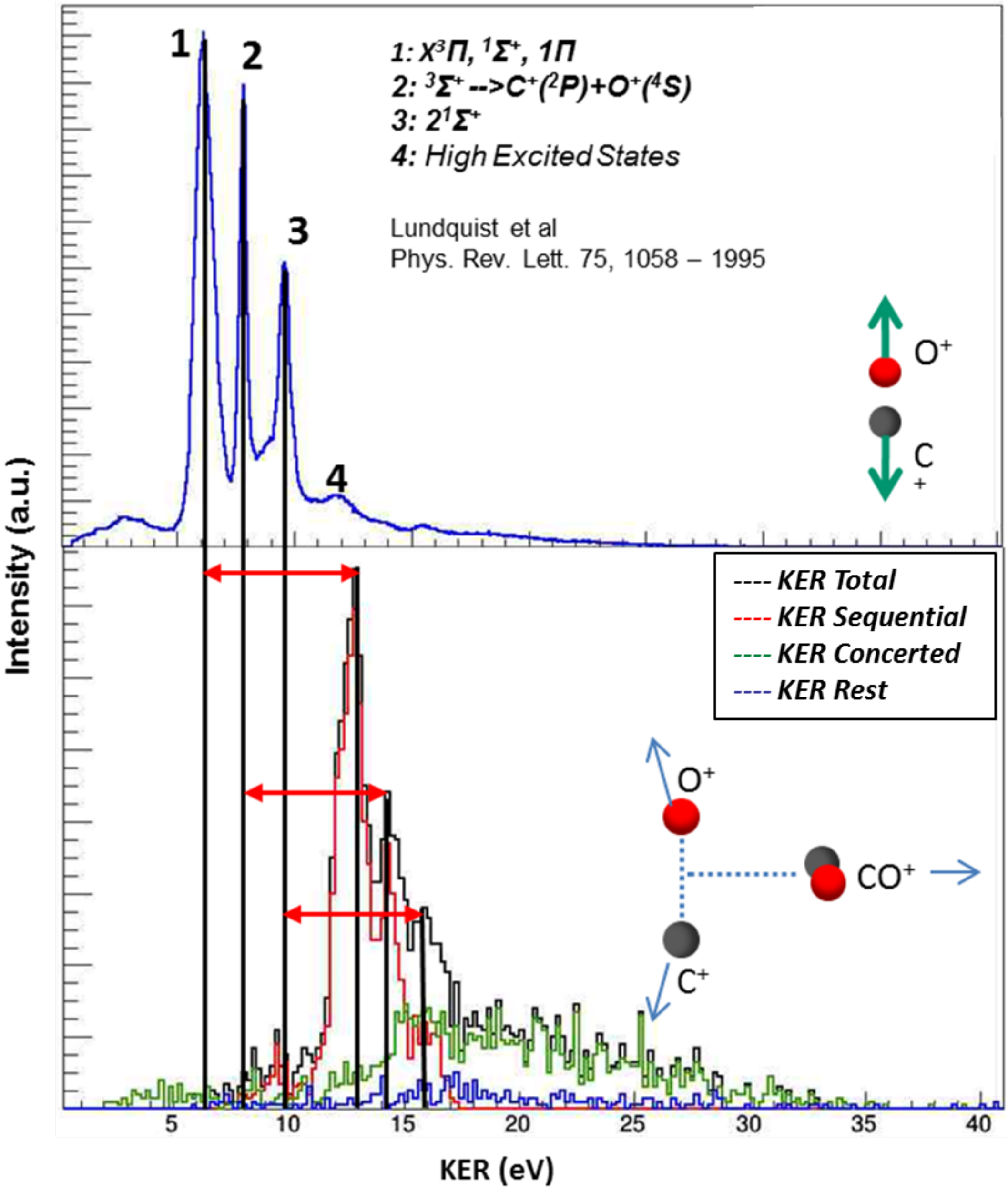

Figure 4.2.6 : *KER spectra of* CO *molecular dication and* $(CO)_2^{3+}$ *from collision with 15 qkeV* Ar^{9+}

the direct and sequential events.

The red line represents the sequential where the green one is the contribution from the direct mechanism. As expected, the sequential fragmentation process is associated to the lower part of the KER spectrum which is known to correspond to long lived metastable states of CO^{2+}. This stipulates that the states involved are long lived within the time range of few ps to around 1 μs, since we are not sensitive to fragments having lifetime more than around 1 μs because of experimental limitations. A numerical calculation has been done for this channel considering two point charges (with charge equals 1 and 2) separated with $R_{(CO)_2}$ (4.52 Å). Assuming a pure Coulomb dissociation the time required for converting 99% of the Coulomb potential energy into kinetic energy is about 1 ps. This indicates that all states with lifetimes larger than 1 ps will contribute to sequential fragmentation. Moving towards the third peak, the contribution from direct mechanism starts to increase along with a noticeable contribution from sequential mechanism as well. The ratio between direct and sequential under this peak is almost similar. After 18 eV the contribution is from the direct fragmentation only. Now looking at this high energy part, they partially correspond to peak 3 and 4 of KER of the monomer CO^{+} dication. As mentioned in Penent's work these peaks consist of around 30 levels with lifetime of about 10^{-14} s range (which is much smaller than 1 ps). As expected, such short lived states are found to contribute to the direct fragmentation in which the CO^{2+} and the dimer bond break at the same time.

As we have seen in previous section that the initial populated states of CO^{2+} are mostly conserved inside a dimer therefore the states contributing to sequential peak are $X^3\Pi$, $^1\Sigma^+$, $^1\Pi$, $^3\Sigma^+$ and $2^1\Sigma^+$. The lifetime for all these states is in the intermediate range of few ps to 1 μs. All the long lived metastable states (lifetime $> 1\mu s$) cannot be detected under this channel. Whereas for the direct fragmentation the states involved are highly excited repulsive states mentioned in Penent's work. These short lived high excited states are under peak 3 of figure 4.2.6 (upper) which correspond to the third peak in KER of $(CO)_2^{3+}$. This peak also contains a contribution of sequential events which are associated to the $2^1\Sigma^+$ state.

4.3 Conclusion

Using the low energy ion-induced recoil ion coincidence measurements, we report on the 3-body fragmentation dynamics of $(N_2)_2$ and $(CO)_2$ dimers.

1) For the $(N_2)_2^{3+} \rightarrow N^+ + N^+ + N_2^+$ channel, the dominant dissociation process is found to be direct fragmentation with only a weak contribution from sequential fragmentation of less than 5%. Secondly, the states involved in the fragmentation of N_2^{2+} dication are weakly affected, by the proximity of a non-dissociating N_2^+ inside a dimer. However there is an additional energy provided to the monomer dication system because of the presence of neighboring ion. This energy is the result of the Coulomb repulsion interaction between the charged fragments. The resulting energy shift of the KER spectra of the 3-body channel is very well reproduced thanks to a simple Coulomb model and including the initial geometry of the dimer.

2) On the other hand, in the 3-body channel $(CO)_2^{3+} \rightarrow C^+ + O^+ + CO^+$, we have found a delayed dissociation mechanism (i.e. sequential) in addition to the fast/direct dissociation mechanism. The presence of these two mechanisms can be identified directly on the kinetic

energy of the non dissociating CO^+. Inside this dimer also we observe the similar effect of the neighboring cation on the dissociation of molecular dication. The KER has been used to distinguish the states involved in the fast (direct) and intermediately delayed (sequential) fragmentation processes. It turns out that higher excited states have shorter lifetimes and mainly contribute to the direct fragmentation. In contrast, only the low lying states with life time larger than 1 ps are found to contribute to the sequential process.

These results show how molecular dimers can be efficiently used as a tool to access the life time of molecular ions produced in collision with highly charged ions.

Geometrical analysis of N_2 and CO dimers

5

Contents

After investigating the fragmentation dynamics for both the N_2 and CO dimers, now we will focus on the 3-D geometry of these two dimers. As already discussed, this geometry could be fully defined using the four coordinates: inter molecular distance (R_{Dimer}), orientation of molecule along the dimer axis (θ_a, θ_b), and torsional angle or angle between both molecular bonds (ϕ)(see figure 5.1.1 (1)). The experimental determination of these coordinates would require the coincident measurement of the 4-body channel in which the dimer fully dissociates into four atomic fragments. However, this particular channel has a very low cross section and the measured yield is even lower due to the low detection efficiency of the four fragments. Thus, this channel has very low statistics and low signal-to-noise ratio. Due to these shortcomings, we will show how a partial 3-D geometry of the dimers can be deduced from the 2-body and 3-body channels which have significantly larger statistics. Shortly, the 2-body channel allows a direct measurement of the inter molecular distance from the position of the total kinetic energy release (KER) peak. Moreover, the orientation of the molecules with respect to the dimer axis (θ_a or θ_b) can be deduced from the 3-body channels. Note that the calculation of the orientation angle theta from the experimental measurements is not straight forward, therefore a numerical simulation of the 3-body dissociation has been performed in order to have a better interpretation of the experimental findings. Note also that for the 3-body channels, the measurement is not sensitive to the torsional angle (ϕ) and that only a partial determination of the geometry is accessible (see figure 5.1.1 (2)). As described in the chapter 2 the interaction with Ar^{9+} ions is faster than the nuclear motion of both molecules so our experimental method allows the determination of the geometry of neutral dimer.
The objective of this chapter is to give the first experimental measurement of the 3-dimensional structure of the N_2 and CO dimers using the Coulomb explosion imaging technique. These experimental findings will be compared to existing theoretical calculations and few experimental measurements performed for both dimers.

5.1 Geometry of the N_2 dimer

We focus on doubly and triply charged dimers leading to 2 and 3-body dissociation channels
(A) $(N_2)_2^{2+} \rightarrow N_2^+ + N_2^+$,
(B) $(N_2)_2^{3+} \rightarrow N_2^+ + N^+ + N^+$.

As discussed in chapter 2, the geometry of N_2 dimers has been investigated through ab-initio calculations with the support of few cross section measurements as well as through photoelectron spectroscopy. It has been shown that several isomeric states (corresponding to different geometries) exist for the ground state of the neutral N_2 dimer. The five most favorable geometrical propositions from the previous studies are summarized in table 5.1.1 below. Table includes the 3-D parameters (see figure 5.1.1) of these geometries which include inter molecular distance and orientation of a molecule.

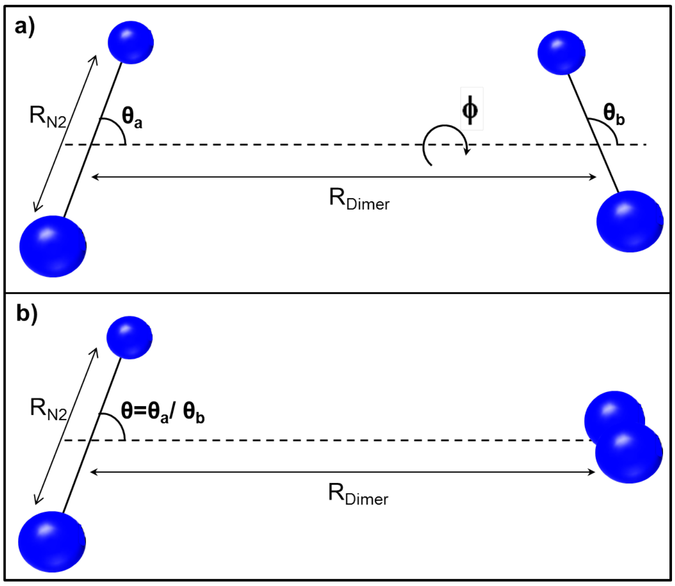

Figure 5.1.1 : *Definition of the dimer geometry using the $(R_{Dimer}, \theta_a, \theta_b, (\phi)$ coordinates. The N_2 molecular bond length is fixed to R_{N_2}=1.1 Å. a): complete three dimensional geometry. b): Partial geometry accessible through the 2-body and 3-body explosion of the dimer. The non-dissociating N_2^+ molecular ion is considered as a point-like particle located at its center of mass and the measurement is not sensitive to the ϕ coordinate.*

Table 5.1.1 : *Three dimensional parameters for $(N_2)_2$ structures proposed theoretically [26].*

Configuration	R_{Dimer}(Å)	θ_a°	θ_b°	ϕ°
H	3.81	90	90	0
X	3.87	90	90	90
T(T_a+T_b)	4.03	0	90	0
Z	4.30	45	45	0
L	4.65	0	0	0

To summarize we have two geometries H and X where both θ_a and θ_b are equal to 90°. The next geometry T is a special case where one molecule in the dimer is parallel to dimer axis and the other is perpendicular to theT_a and T_b which are part of same configuration T, however they can be distinguished as θ_a and θ_b while discussing triple electron capture of $(N_2)_2$ dimer. Then we have the only canted configuration Z with θ_a and θ_b as 45°. At the end we have a linear configuration L where the two molecules are aligned with the dimer axis.

5.1.1 2-body dissociation channel: Inter molecular distance

As already described in chapter 4, the bond length is measured from the position of the KER peak in channel A. We have found an average KER value of 3.35 eV from its distribution (refer to figure 4.1.1), which correspond to 4.29 Å as the equilibrium bond length $R_{(N_2)_2}$ of $(N_2)_2$ dimer. Our measured KER value agrees well with that obtained from the core excitation using synchrotron radiation followed by intermolecular coulombic decay process by Trinter et al [111]. They have found 4.03 Å as the intermolecular distance however the relaxation process was different in their case as they were observed KER peak for interatomic coulombic decay process. Comparing to ab-initio calculation, our $R_{(N_2)_2}$ value is in fair agreement with the theoretical predictions of T and Z shapes [20, 26]. However, the predicted bond length differs only by 10% for the different geometry. For this reason, no definitive conclusion can be made only from the R_{Dimer} value. Now we will discuss the 3-body channel in order to understand the partial geometry of this dimer by accessing the variable θ.

5.1.2 3-body dissociation channel: Molecular orientation in the dimer

As already mentioned, the initial orientation θ (θ_a or θ_b) can not be directly deduced from the experimental observable. Here we will use a comparison to a Monte Carlo simulation of the 3-body break up to indirectly infer the initial angle θ from our data. In fact, the distribution of the momentum of the 3 fragment depends on:
i) the intermolecular distance of dimer $R_{(N_2)_2}$,
ii) the orientation of the dissociating molecule with respect to the dimer axis i.e. θ and
iii) the shape of the potential energy curve of the dissociative $N^+ + N^+$ state.

From our experimental observation the equilibrium intermolecular distance $R_{(N_2)_2}$=4.29 Å. In the following we will use different experimental observables: kinetic energy of each fragment, KER of the N_2 monomer dication and also the angle ψ which is defined in figure 5.1.2.

The 3-body model in figure 5.1.2 explains the reconstruction of the angle ψ which is dependent on the initial angle θ but also on the KER of N_2 molecule. The angle ψ is constructed using the momentum of both atomic ions from the dissociating N_2^{2+} molecular ion. The momentum of the second fragment $\overrightarrow{P}_2$ to reach the detector is subtracted from the momentum of the first fragment $\overrightarrow{P}_1$ which gives the resultant vector $\overrightarrow{P}_1 - \overrightarrow{P}_2$. The angle between this resultant vector and the momentum vector of non-dissociating molecular ion N_2^+ is called as ψ. The angle ψ is in general not equal to θ. However, ψ is equal θ=90° and if both atomic fragments have same mass and same charge.

As we discussed in the chapter 4 about the sharing of the kinetic energy among the 3 fragments in case of channel (B), the kinetic energy spectra of N_2^+ is shown in figure 4.2.1. As most of the events in the channel (B) correspond to fast synchronous direct fragmentation

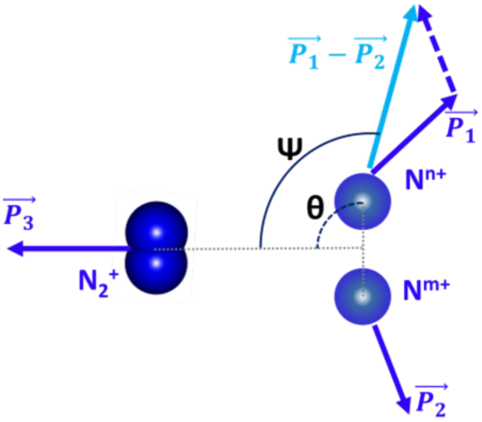

Figure 5.1.2 : *2D representation of 3-body* N_2 *dimer showing the angle* ψ *deduced from the coincident measurement of the momenta of the three fragments in the* $N_2^+ + N^+ + N^+$ *channel*

the kinetic energy of the non dissociating N_2^+ is low because of the fast repulsion of the two atomic ions. This kinetic energy depends on the angle θ as well as on the KER of the N_2 monomer dication. The desired information about the geometry of the dimer can only be accessed through these synchronous direct events therefore we will use them in the following discussion. Although, due to their prominence over sequential events there is no filter on the kinetic energy of N_2^+ to avoid these events.

5.1.2.1 Numerical simulation of 3-body dissociation

The distribution of the momentum among the fragments following a 3-body fast synchronous dissociation has been investigated using a classical model. Here we will present a simple model used to determine the final momenta of three charged point like particles after dissociation as a function of the initial geometry.

Description

In a 3-body channel we only have access to θ which limits our input parameters for simulation. A schematic representation of 3-body dissociation of $(N_2)_2^{3+}$ through the channel $N^+ + N^+ + N_2^+$ is described in the figure 5.1.1 b). Few assumptions and initial geometrical conditions have been used to mimic the the 3-body dissociation. All the three fragments are considered as point like charges situated at their center of mass initially at rest. The simulation is initialized with an initial configuration resembling the geometry of the neutral cluster by positioning ions at their atomic positions (see figure 5.1.1 b)). The equilibrium R_{N_2} is set to 1.1 Å and the $R_{(N_2)_2}$ or R_{Dimer} and θ values for different configurations of $(N_2)_2$ are provided in table 5.1.2.

The model assumes a fast synchronous direct fragmentation where both the van der Waals and covalent bond break at the same time. Therefore forces on all the three ions start acting

Table 5.1.2 : *Updated geometrical parameters in accordance to 3-body dissociation experimental observable in figure5.1.1 b). Here we only account the average R_{Dimer} along with the orientation of the dissociating molecule i.e. θ. We take an average of all the theoretical R_{Dimer} values to use the categorize the five geometry just with their orientation angle θ.*

Configuration	R_{Dimer}(Å)	$\theta(\theta_a/\theta_b)$
H,X,T$_a$	4.23	90
Z	4.23	45
L,T$_b$	4.23	0

at the same time. Each force consists of two components from two neighboring ions as shown in equation 5.1.1. In equations 1, 2 and 3 are the identifiers for N^+, N^+ and N_2^+.

$$\vec{F}_i(i = 1, 2, 3) = \sum_{j=1,2,3}^{i \neq j} \vec{F}_{ji} \tag{5.1.1}$$

The forces on the each ion are calculated using an electrostatic repulsive forces induced due to coulombic repulsion from the force fields of neighboring ions. Although, the assumption of such Coulomb potential is only true for the case of force on 1 and 2 due to 3 and vice-versa. On the other hand, the potential between atomic ions 1 and 2 of dissociating molecule is not purely coulombic as it can be evidenced from the wide KER distribution of $N_2^{2+} \rightarrow N^+ + N^+$ channel. To account for this KER distribution instead of the ab-initio based potential energy curves in our model, we used a "corrected" Coulomb potential shown in equation 5.1.2.

$$V_{12} = \frac{q_1 q_2}{4\pi\varepsilon_0} \cdot \frac{A_{12}}{r_{21}} \tag{5.1.2}$$

where r_{21}=R_{N_2} and q_1, q_2=1. An additional unit less parameter A_{12} is used to define the potential between both 1 and 2 ions in equation 5.1.2 which helps in shaping the potential curve for 2-body dissociation of monomer. Using the above potential, we will get a KER for 2-body breakup of a monomer at an interatomic separation of R_{N_2}=1.1Å, which is described in equation 5.1.3.

$$KER_{12} = \frac{1}{4\pi\varepsilon_0} \cdot \frac{A_{12}}{R_{N_2}} = \frac{14.4}{1.1} \times A_{12} \simeq A_{12} \times 13.1eV \tag{5.1.3}$$

Here 13.1 eV is the total kinetic energy released assuming a pure Coulomb dissociation of N_2 dication. In our model this parameter is calculated using the relation below

$$A_{12} = \frac{KER_{N_2}\_Experimental}{13.1}, \tag{5.1.4}$$

thus, as the KER varies from 5 to 50 eV, it corresponds to A_{12} varying from 0.38 to 3.8. Using the above potentials the forces acting between each ion are deduced below in equation

5.1.5, 5.1.6 and 5.1.7.

$$\vec{F}_{13} = \frac{q_1 q_3}{4\pi\varepsilon_0} \times \frac{1}{r_{31}^2}\hat{u}_{31} \tag{5.1.5}$$

$$\vec{F}_{23} = \frac{q_2 q_3}{4\pi\varepsilon_0} \times \frac{1}{r_{32}^2}\hat{u}_{32} \tag{5.1.6}$$

$$\vec{F}_{12} = \frac{q_1 q_2}{4\pi\varepsilon_0} \times \frac{A_{12}}{r_{21}^2}\hat{u}_{21} \tag{5.1.7}$$

Now using equation 5.1.1, we will have the coupled differential equation (DE) of the three interacting particles using the equation of motion of the particle labelled "i".

$$\vec{v}_i = \frac{d\vec{r}_i}{dt} \tag{5.1.8}$$

$$m_i \frac{d\vec{v}_i}{dt} = \sum_{i=1,2,3} \vec{F}_i = \sum_{j \neq i} \vec{F}_i \tag{5.1.9}$$

where $\vec{v}_i$ is the velocity of the particle, $\vec{r}_i$ is its position vector and t is time (t=0 is the instance of collision). These coupled DE's are integrated over a time period of 1 ns using a sub routine of Runge-Kutta ODE solver. We use 1 ns as interval for this integration since this is a sufficient time to reach the asymptotic momentum limit for all the 3 ions. A sample case of 3-body dissociation of channel (B) is shown in figure 5.1.3 using the $A_{12} \approx 1$.

The figure 5.1.3 a), c) and d) shows the ion trajectories for the three geometries with θ=0°, 45° and 90°. In figure 5.1.3 b) the evolution of kinetic energy of each ion and the total KER for channel are shown as a function of the time. All the three ions reach the kinetic energy asymptotic limit after about 1 ps.

Dependence of experimental observable on initial parameters

Once we obtained the momentum vectors after the integration time of 1 ns we will use them to state the dependence of theoretical parameters (θ, $KER\_N_2^{2+}$) on the experimental observable (ψ, $KE\_N_2^+$). We used the KER of N_2^{2+} ranging from 5 to 50 eV (A_{12} = 0.38 to 3.8). Figure 5.1.4 shows the evolution of the kinetic energy of non dissociating N_2^+ with the initial θ and the $KER\_N_2^{2+}$. For values of θ ranging from 20°-90° the kinetic energy acquired by N_2^+ is relatively low and decreases when the $KER\_N_2^{2+}$ is high. The high $KER\_N_2^{2+}$ implies a fast dissociation of both N^+ ions which results in less time for N_2^+ to be affected by their repulsive electric field, thus resulting in a small final kinetic energy of the N_2^+ ion. Whereas in the case of θ ranging from 0° to 20°, it is totally opposite i.e., for the high $KER\_N_2^{2+}$ values the kinetic energy of N_2^+ is higher because of the additional kinetic energy from one of the N^+ fragment is directed towards the N_2^+.

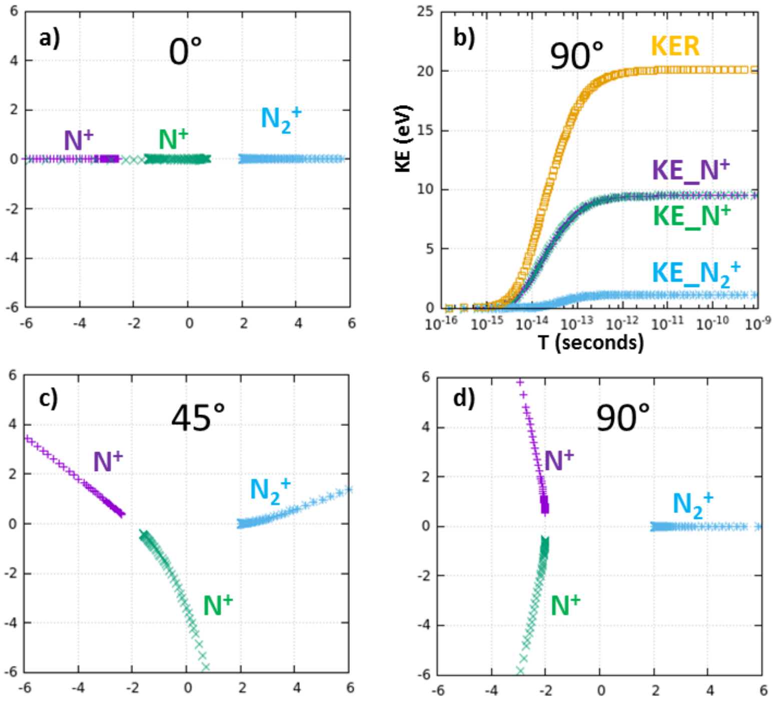

Figure 5.1.3 : *a), c) and d): calculated ion trajectories of the 3-body dissociation of the channel (B) for θ=0°, 45° and 90°. b): Evolution of the kinetic energy and total KER as a function of time for θ=90°.*

Using figure 5.1.4 we can distinguish between geometries with θ= 0° and θ= 45° or 90 °. Although, the kinetic energy of N_2^+ is poorly sensitive to θ over the 30° to 90° range. Due to this only a little difference is observed between the geometries with θ= 45° and θ= 90°.
Now using the momentum vectors of three ions we accessed the angle ψ and its dependence with the initial angle θ and $KER\_N_2^{2+}$ is shown in the figure 5.1.5. As we stated earlier, for symmetry reasons ψ is equal to 90° if θ= 90° for this channel. It is because, obviously the two N^+ atomic ions have similar masses and charges.

For θ ranging from 45° and to 90° the angle ψ is only poorly sensitive to θ and results in ψ from 90° to 100° range. As we move to lower values of angle θ (less than 40°) the sensitivity of $KER\_N_2^{2+}$ on the angle ψ is highly increased. This high sensitivity on $KER\_N_2^{2+}$ makes it difficult to deduce the initial angle θ from ψ. Although when we reach toward θ= 0° this high sensitivity is minimized and ψ is equal to 180°. For this configuration, the ψ is independent of the value $KER\_N_2^{2+}$ because the three ion propagates along the horizontal axis.

Convolution with experimental conditions

To achieve better understanding and comparison of simulation with experimental results we added few experimental conditions in our simulation. The orientation of the dimer target is chosen according to an isotropic distribution. This orientation is in respect to the laboratory

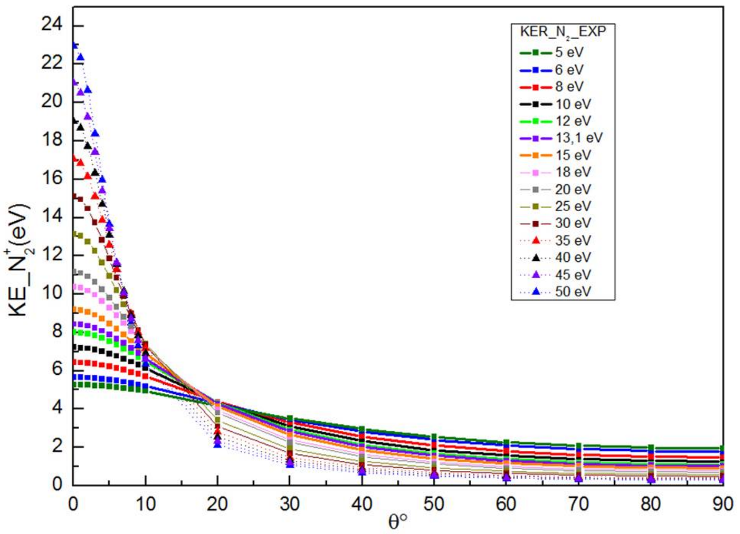

Figure 5.1.4 : *Correlation graph showing the dependence of measured kinetic energy of non-dissociating N_2^+ from 3-body dissociation with initial θ and $KER\_N_2^{2+}$.*

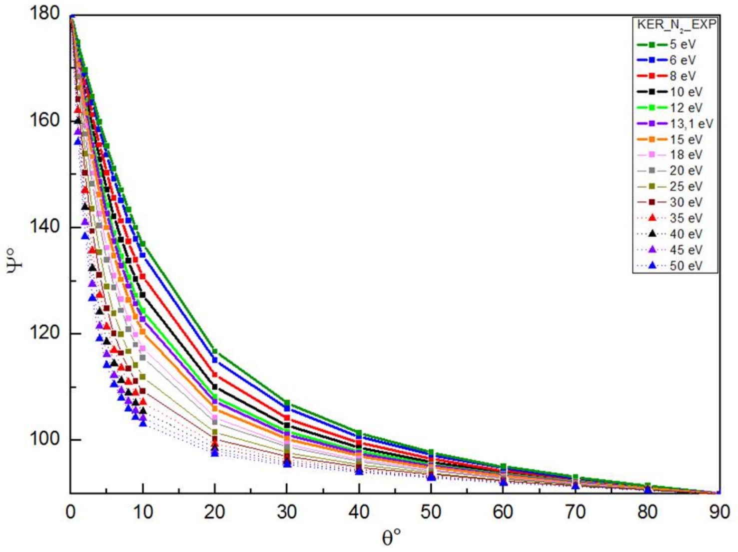

Figure 5.1.5 : *Correlation graph showing the dependence of initial θ and $KER\_N_2^{2+}$ on the measurement of angle ψ from 3-body dissociation.*

frame. We neglect any angular dependence of the electron capture process with the dimer orientation leading to an isotropic initial orientation of the dimer. The molecules inside a dimer have thermal agitation due to vibrational and rotational motion which causes the large experimental distributions. We accounted this vibration of the molecules along molecular axis in a dimer and it is denoted by using $d\theta = \pm 20°$. The initial values of θ are chosen as a gaussian distribution centered at θ= 0, 45 or 90° in figure figure 5.1.1 b) and with a standard deviation $d\theta = 20°$. The vibrations of these molecule inside the dimer also result in stretching and compression of intermolecular bond/van der Waals bond. This bond is variable for different configurations so to account the fluctuation in bond length, we measure the standard deviation (σ_{KER}) of the kinetic energy release (KER) distribution for pure 2-body Coulombic dissociation of a dimer. The fluctuation is around 10% of the peak value i.e. 10% on the R_{Dimer} (see chapter 4). Here we use $R_{(N_2)_2}$=4.3 Å and $\sigma_{R_{(N_2)_2}}$=0.43Å.

In our experimental setup, the collision region for the overlap of the projectile and target supersonic jet of 600 μm and 1.5 mm in diameter respectively. The size of this beam collision region is estimated and initialized to be a sphere of 300 μm radius. The initial position vectors for center of mass of the three ions in this dimer are randomly generated using a Gaussian distributions with standard deviation of $\sigma_x, \sigma_y, \sigma_z = 300\mu$m. Calculating the velocity of the supersonic jet (v_{jet}) theoretically and from our experimental data (chapter 2); this is initialized to be 700 m/s. During collision the transverse momentum is exchanged between projectile and target, which contributes to experimental resolution. This means we need to account the initial velocity from experimental data sets with standard deviation of about σ_{vx}, σ_{vy} and $\sigma_{vz} =$ 300 m/s. With v_{jet} as mean initial velocity of supersonic jet target, momentum exchange with projectile contributes to distribution of initial velocity of target in center of mass frame (v_{cm}).

To reproduce the simulation close to experimental conditions now we consider an homogeneous extraction field (E_{ext}) of 4000 V/m for the recoil ion spectrometer. Thus we also add an additional force due this homogeneous electric field in equation 5.1.1, new equation will be 5.1.10

$$\vec{F}_i(i = 1, 2, 3) = q_i\vec{E}_{ext} + \sum_{j=1,2,3}^{i\neq j} \vec{F}_{ji} \tag{5.1.10}$$

with $\vec{E}_{ext} = E_{ext}\hat{u}_x$. Once the ions are far enough from each neighbor ions(see figure), we stop using Coulomb potential for their migration and let them get extracted upto the detector using only the extraction field. This propagation is calculated using the equation of motion in 5.1.11, where $\vec{u}$ and $\vec{a}$ are velocity vector after 1 ns and acceleration due to the extraction field respectively.

$$\vec{S} = \vec{u}t + \frac{1}{2}\vec{a}t^2 \tag{5.1.11}$$

Once we determine the time t as the TOF of ions from above equation we can get the position coordinates of ions on the detector using; $Y = Y_0 + v_y \times TOF$ and $Z = Z_0 + v_z \times TOF$. Then position and the TOF parameters are convoluted with the spatial and temporal detector resolution ($\Delta t, \Delta y, \Delta z$). The resolution of TOF, Y and Z are fixed to 1 ns and 0.1 mm for both Y and Z position coordinates. Once we have (TOF, Y, Z) for all events, we transform this data set into 3D momentum vectors (P_x, P_y, P_z) for each particle using the same data analysis program as for experimental data.

5.1.3 Results: Experimental vs Simulation

Using the above explained simulation we performed the simulation for three main geometries that are summarized in table 5.1.2. In figure 5.1.6 a) we have the distribution of ψ from the simulation along with the experimentally observed ψ distribution in figure 5.1.6 b). In simulated spectra of ψ distribution for geometry with θ=90° there is one peak centered around 90°. For the next geometry with θ= 45°, we observed two peaks around 83° and 97°. This peak distribution is wider because of the higher sensitivity of ψ on the $KER\_N_2^{2+}$. Finally for linear geometries with θ=0°, a widely spread distribution on both sides of 90° is observed. The ψ reproduces a valley at 90°.

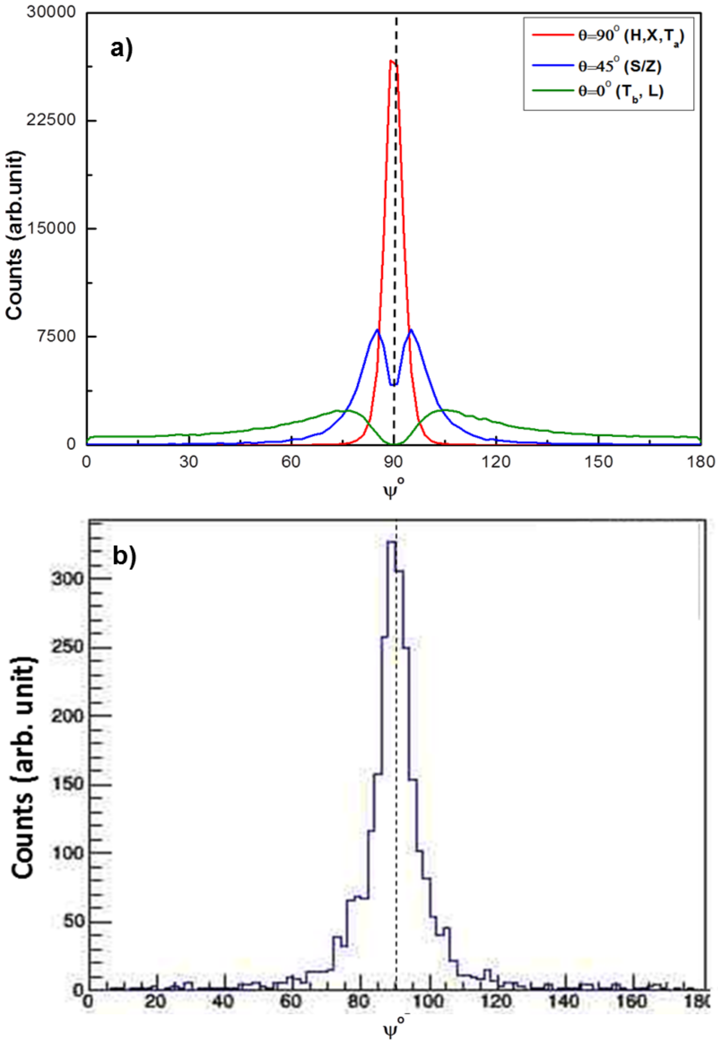

Figure 5.1.6 : *a): ψ distribution obtained from the simulation for the configuration accounted in table 5.1.2, b): Experimentally observed ψ distribution for the channel (B).*

In figure 5.1.6 b) the measured experimental ψ distribution from 3-body channel (B) is shown. For this channel the distribution is well centered around 90° and is in agreement with the simulated spectra for θ=90° dimer in figure above (red curve). Unlike in the simulated spectra for θ=45° (blue curve) there is no evidence of the two contributions centered around 83° and 97° in our experimental ψ distribution. Similarly there is also no evidence for the geometries with θ=0°. Henceforth, with the agreement over θ=90°, only the H, X or T_a shape are possible candidates as initial geometry of the N_2 dimer. Note that the T-shape geometry would result in two contribution depending on either the dissociating N_2^{2+} is the one perpendicular or aligned with the dimer axis. Since the electron capture process is not expected to be favoring one molecular configuration inside the dimer therefore the T-shape geometry is supposed to give rise to two contributions corresponding to θ= 0° and θ= 90° with relative intensities of about 50%. Therefore, the T-shape can be excluded from predicted geometry. Thus we can conclude that using the comparison between experimental and simulated ψ distributions geometrical configuration of $(N_2)_2$ dimer is either H or X shape.

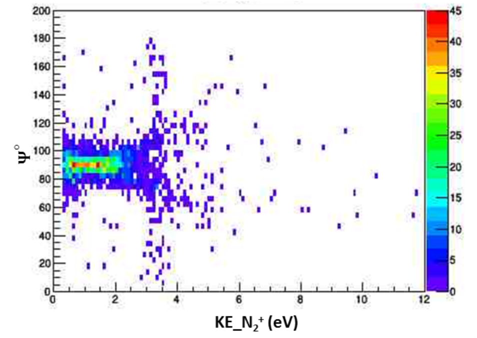

Figure 5.1.7 : *Two dimensional correlation between the measured angle ψ deduced from $N_2^+ + N^+ + N^+$ channel as a function of kinetic energy of N_2^+.*

In figure 5.1.7 a correlation between the experimental ψ distribution as a function of kinetic energy of non dissociating N_2^+ is shown. As explained before we can see that the angular information is preserved in the fast synchronous direct events. The high intensity region below 3 eV correspond to those events. No dependence of ψ with kinetic energy of non dissociating N_2^+ is observed which confirms the molecular orientation to be θ=90°. A slight vertical straight line around 3.35 eV is due to few long lived metastable states showing signs of sequential fragmentation. This two dimensional graph can also be used to differentiate between direct and sequential fragmentation as it will be discussed for CO dimers.

5.2 Geometry of the CO dimer

To discuss the geometry of CO dimer we will use exactly the same analysis as in the case of N_2 dimer. Since the late 90's there had been a lot of theoretical calculations done to determine the structure of CO dimer [14,28,30,32–35,112–114]. There were a few infrared (IR) spectrometer experiments by various collaborative groups [28, 30, 32, 34, 113–115]. In almost all of the calculations and IR experiment the predictions are coherent for C-bonded (T-shaped or anti parallel) with bond length of 4.4 Å and O-bonded (T-shaped or anti parallel) with bond length approximately 4 Å. Although, for a complete investigation we use all configurations from previous calculation and measurements which are mentioned in Nxumalo's paper [30]. Table 5.2.1 below accounts the five proposed configuration of CO dimer with corresponding three dimensional geometry parameters. The three dimensional and two dimensional structure for CO dimer are exactly the same as shown in figure 5.1.1, apart from the measurement of the angle θ is chosen to be with respect to the oxygen atom in the CO molecule.

Table 5.2.1 : *Theoretically proposed 3-dimensional parameters for $(CO)_2$ structures*

Configuration	R_{Dimer}(Å)	θ°_a	θ°_b	ϕ°
C-Bonded antiparallel	4.4	135	45	180
O-Bonded antiparallel	3.96	45	135	180
T shape C-CO	4.42	90	0	0
T shape O-CO	3.88	0	90	0
Linear O-O	4.62	0	0	0

As in the case of N_2 dimers we will focus only on doubly and triply charged CO dimers leading to
(C) $(CO)_2^{2+} \rightarrow CO^+ + CO^+$ and
(D) $(CO)_2^{3+} \rightarrow CO^+ + C^+ + O^+$
2 and 3-body dissociation channel respectively.

5.2.1 2-body dissociation channel: Inter molecular distance

The intermolecular distance inside a dimer is deduced from the KER spectra of the 2-body channel (C) with single charge on each CO molecule inside the dimer. In figure 4.1.2 we have the KER spectra for channel (C) (see chapter 4). The peak is centered at the mean value of 3.18 eV. This value is consistent with the one reported by Ding et al in [46] obtained using a similar Coulomb imaging technique where they used an ultrashort intense laser pulses to achieve multiple excitation of CO dimer target. Although the main objective of there work was to study the fragmentation dynamics. Assuming a pure Coulomb dissociation for the 2-body channel (C) the equilibrium intermolecular distance $R_{(CO)_2}$ is found to be 4.52 Å.

The $R_{(CO)_2}$ is very close to the intermolecular distances predicted for C-bonded antiparallel,C-bonded T-shaped and the O-bonded configurations. Furthermore, in various ab-initio calculations it is found that the global minimum of the potential energy surface of CO dimer are for antiparallel C-bonded configuration (θ=135°), with the intermolecular distance predicted around 4.4 Å. Therefore the geometry is more likely to correspond to the C-bonded structure. For further investigation of these geometrical configurations, the analysis of the 3-body dissociation channel will be used along with the simulation results.

5.2.2 3-body dissociation channel: Molecular orientation in the dimer

As we discussed in previous chapter the fragmentation dynamics of CO dimer is different from the N_2 dimer, with two prominent pathways: fast synchronous direct and sequential. These two mechanisms are easily separable using the KE of non-dissociating CO^+ from channel (D)(see figure 4.2.3). The peak for sequential events is around 3.2 eV which can be calculated by using the Coulomb dissociation approximation in the first step of $CO^+ + CO^{2+}$.
For channel (D), the sequential pathways is a two step process where the first step is a pure Coulomb explosion of the dimer into $CO^+ + CO^{2+}$. Then the longlived CO^{2+} randomly rotates in space before dissociating further into atomic ions. This is why only fast synchronous direct events are used for determination of initial molecular orientation θ. A filter on the kinetic energy of the non-dissociating CO^+ i.e. events below 2.5 eV (see figure 4.2.3) is used to separate these events.

As we have already discussed the torsional angle (ϕ) is not accessible from the 3-body channel. Therefore for partial geometry we will update the table 5.2.1 to table 5.2.2, on the basis of initial angle θ and R_{Dimer} (depending on C-bonded or O-bonded). Using the configurations in the table 5.2.2 we performed a 3-body dissociation simulation similar to the one described in the case of N_2 dimer.

Table 5.2.2 : *Updated geometrical parameters in terms of initial angle θ. Here we choose two average R_{Dimer} values. One corresponding to C-bonded (4.4 Å) and the other one O-bonded (4 Å).*

Configuration	R_{Dimer}(Å)	$\theta(\theta_a/\theta_b)$
Slipped anti parallel (C-C)	4.4	135
Slipped anti parallel (O-O)	4	45
T$_a$ (CO-C/CO-O)	4.4	90
L, T$_b$(CO-O)	4	0
T$_b$(CO-C)	4.4	180

Since, CO is heteronuclear we can not compare to the results of the N_2 dimer directly. We adapted the simulation accordingly by changing the interatomic distance (R_{CO}=1.128Å), similarly the KER of CO^{2+} from monomer is used to shape the potential curve for CO^{2+} inside a dimer. The jitter on θ is 20° and the jitter on R_{Dimer} or $R_{(CO)_2}$ is 0.4 Å as for N_2 dimers. The ψ distributions obtained from simulation for the five configurations in table 5.2.2 are shown in figure 5.2.1 a). For the initial θ=135° (C-bonded) there is one peak centered at 80°. Secondly, for θ=45° (O-bonded) the ψ distribution is much wider than in the case of θ=135° and is centered around 98°. Now the case with θ=90° is slightly different from the case of N_2 dimer as masses of C and O are not equal. The ψ distribution for this case is centered around 86.5°.

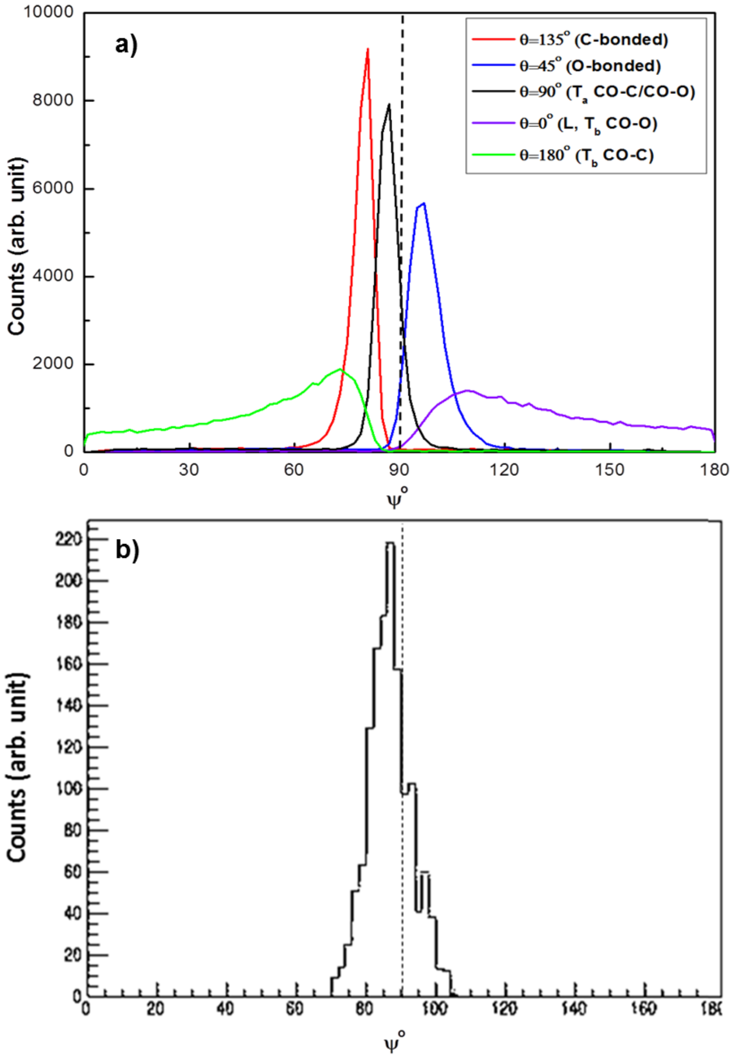

Figure 5.2.1 : *a): ψ distribution obtained from the simulation for the configurations accounted in table 5.2.2, b): Experimentally observed ψ distribution for the channel (D).*

Lastly, for configurations with θ=0° and 180° the ψ distributions are spread from 90°-180° and 0°-90° respectively. The figure 5.2.1 b) shows the experimental distribution of the angle ψ from direct events channel (D). There is a single peak centered at 86.1°. The experimental spectra fits perfectly with the simulated spectra for θ=90°. All the other configurations does not able to reproduce the experimental data henceforth they all can be excluded.

As in the case of N_2 dimers, a T-shape geometry would result in two distinct contribution corresponding to θ=0° and θ=90°. The experimental spectrum does not show any evidence for a θ=0° geometry. Therefore the T-shape geometry for both the C and O-bonded can be excluded. This however generates the possibility of introducing propositions for the geometry of CO dimer, there is a possibility of having a planar H or non planar X configuration similar to the case of N_2 dimer. To investigate more about these structures we need to be susceptible to the torsional angle ϕ which would require the analysis of the 4-body channel.

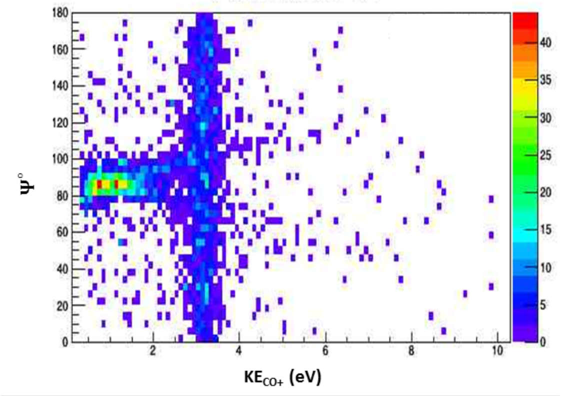

Figure 5.2.2 : *Two dimensional correlation between the measured angle* ψ *deduced from* $CO^+ + C^+ + O^+$ *channel as a function of kinetic energy of* CO^+.

In the end, a correlation graph between the angle ψ with KE of CO^+ is presented in figure 5.2.2. Both the synchronous direct and sequential process can be seen separately. The high density contribution in region below 2.5 eV and 86.1° corresponds to the event involved in synchronous direct process. Whereas a straight vertical line centered around 3.2 eV and distributed along 0°-180° results from the 2-step sequential process. This isotropic distribution of ψ for these events confirms that the fragmentation time of the CO^{2+} is much larger than its rotational period in the first step $CO^+ + CO^{2+}$.

5.3 Conclusion

We used the 2 and 3-body dissociation channels of N_2 and CO to determine the three dimensional structure of these molecular dimers. The intermolecular distance has been deduced from the KER distribution of the 2-body dissociation channels while we used a comparison to Monte-Carlo simulation of the 3-body break up to derive the molecular orientation θ from the experimental observable.

1) From the experimental measurement using the 2-body channel the equilibrium intermolecular distance for N_2 dimer is 4.3Å. The orientation of the dissociating molecule inside the dimer is deduced using ψ to be around θ=90°. Using the Monte-Carlo simulation the value of this initial angle θ is in agreement with H or X shapes. The measured intermolecular distance is in agreement with measurements done in Trinter's work using the Coulomb imaging

technique [111]. Although, the predicted intermolecular distances calculated theoretically for H and X configurations are not in agreement. On the contrary the Z configuration agrees perfectly with our measurement of intermolecular distance.

2) For CO dimer using the KER from 2-body channel the equilibrium intermolecular distance is measured around 4.52 Å. The orientation of the dissociating molecule inside the dimer is found to be 90°. The experimental ψ distribution is a single peak centered at 86.1° which correspond to θ=90° configurations. Using the simulation none of the proposed theoretical configurations fits with our experimental measurement of angle ψ. Therefore we propose the geometry for CO dimer could be a C-bonded H shaped parallel/anti-parallel or X shaped crossed with torsional angle ϕ = 90°. For this heteronuclear complex we have options between C or O-bonded configurations. Since the uncertainty in our KER measurement is much lower than 10%, therefore comparing with theoretical and infrared measurements from the previous work the CO dimer is more likely to be C-bonded. Our measured intermolecular distance are consistent with the Ding's work using the the similar Coulomb imaging technique [46].

For both N_2 and CO dimer the analysis of multiply charged $(N_2)_2^{q+} \rightarrow N_2^+ + N^{m+} + N^{n+}$ and $(CO)_2^{q+} \rightarrow CO^+ + C^{m+} + O^{n+}$ channels with $m \geq 1$, has been done and the conclusion is same for both geometries. The Coulomb imaging technique has been the most significant technique to provide answers regarding intermolecular distance and partial geometry of dimers. However, for further discrimination between the H or X geometry we need to be measure the three dimensional parameter ϕ and it will be possible with the 4-body dissociation channel only.

Geometrical Analysis of N_2 and CO trimers

6

Contents

In this chapter we increase the cluster size from dimer to trimer. As explained in Chapter 3 the production of trimers at room temperature is possible with a high inlet pressure of about 20 bars. Coulomb explosion of triply ionized trimers of both N_2 and CO are discussed in this chapter with the objective of determining the geometrical structure of these trimers. Upto our knowledge, there are no previous experimental results using imaging technique investigating molecular trimers. Note that such equilateral triangle geometries have already been measured for Ar_3 and Ne_3 using a similar Coulomb imaging explosion technique [85, 87]. There had been few theoretical calculations done along with Raman spectra to find the low energy configurations of weakly bound $(N_2)_n$ (n=2-6) complexes [116]. In this work they have proposed an equilateral geometry for $(N_2)_3$ trimer. Similarly for $(CO)_3$ trimer a theoretical and IR spectroscopy has been performed to comment over the geometrical configurations of this trimer [117]. For $(CO)_3$ as well an equilateral planar geometry has been proposed which is claimed to be C-bonded.

6.1 3-body fragmentation of N_2 trimers

The fragmentation of $(N_2)_3^{3+}$ trication if one electron is captured of each molecule is via the $(N_2)_3^{3+} \rightarrow N_2^+ + N_2^+ + N_2^+$ channel. Depending upon the trimer geometry the total energy will be shared differently among all the fragments. Similar to the case of dimer we will use KER and Newton Diagram to identify the geometry. In addition, for further analysis we will also use Dalitz plots to describe the momentum sharing between each fragment corresponding to a certain geometry. Moreover, the equilibrium inter molecular distance $R_{(N_2)_3}$ can be deduced from the KER measurement.

6.1.1 KER Spectra of $(N_2)_3^{3+}$

In figure 6.1.1 the total KER for the 3-body channel of $(N_2)_3^{3+} \rightarrow N_2^+ + N_2^+ + N_2^+$ is shown. The KER peak starts to build up from around 5 eV, from here it goes until the most probable value of the distribution at 9.75 eV. The KER peak is clearly asymmetric (with left skewed shape) and the fast drop on the high energy side may be due to the minimal intermolecular distances in the trimer.

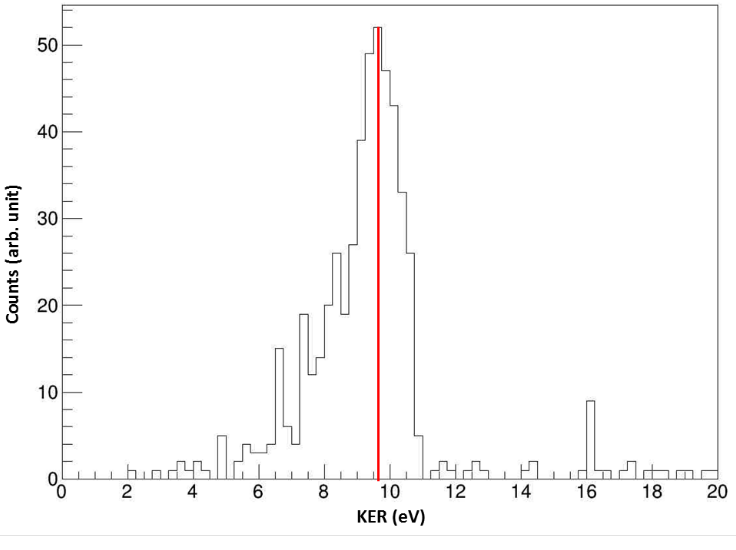

Figure 6.1.1 : *KER spectra for $(N_2)_3^{3+}$ 3-body channel from the collision with 15 qkeV Ar^{9+}*

Along with the total KER of the 3-body channel, the energy distribution among the 3 fragments is also observed. Figure 6.1.2 shows the kinetic energy of all three N_2^+ ions in order of their arrival on the ion detector. These peaks look very similar to the shape of the total KER spectra having a long tail at low energy part and a sudden drop in high energy. The maximum kinetic energy for all the three fragments is almost the same i.e around 3.25 eV.

The equally shared energy between all the three fragments indicates a symmetrical arrangement of the $(N_2)_3$ trimer where the three molecules sits at the "corner" of an equilateral

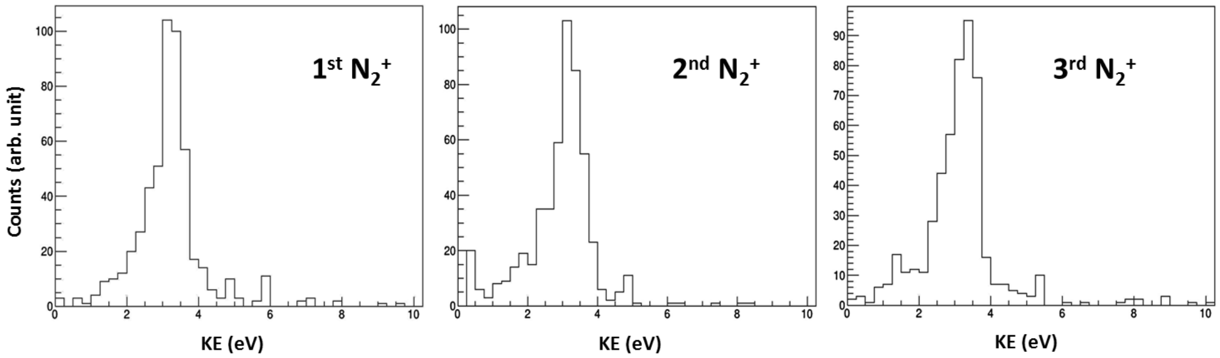

Figure 6.1.2 : *Kinetic energy spectra for all the three N_2^+ from $(N_2)_3^{3+}$ trication. First, second and third are assigned according to their time of arrival on the ion detector.*

triangle. The very small contribution in the low energy part (close to 0 eV) of the kinetic energy of the second N_2^+ is due to the false coincidences in our data. Although it has no significant effect on our total KER as the statistics of these events are quite low. Such a contribution is also observed for $(CO)_3$ trimers and will be discussed more in detail later. Now, we will see in the next section how the symmetry in kinetic energy distribution can be explained by using the Newton diagram.

6.1.2 Newton Diagram

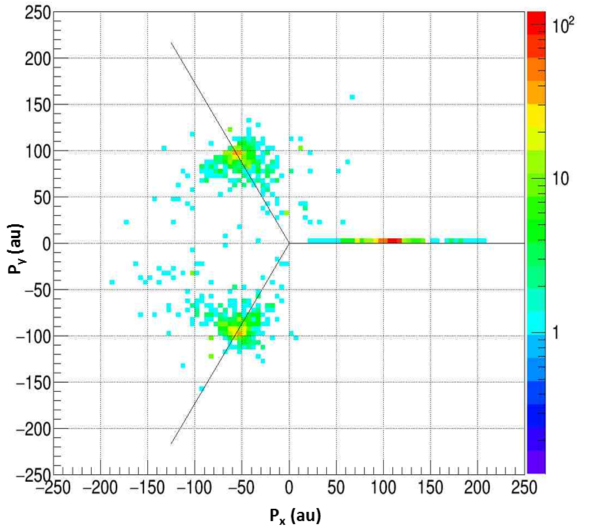

Figure 6.1.3 : *Newton diagram showing the 3-body pure coulomb dissociation of $(N_2)_3^{3+}$, the second fragment to arrive on detector is taken as the reference. Momentum are in atomic units (a.u.).*

Figure 6.1.3 shows the Newton diagram of the $(N_2)_3^{3+} \rightarrow N_2^+ + N_2^+ + N_2^+$ channel. Here, we choose the second N_2^+ fragment as a reference on the X-axis. The momentum of the first fragment is plotted in the lower part of the spectrum while the third fragment appears in the upper part. We observe two contributions centered around P_x= -55 au and P_y= ±95 au. The corresponding momentum strength is $P = \sqrt{(\pm 95)^2 + (-55)^2} \simeq$ 110 au, which is also strength of momentum vector of the reference N_2^+ fragment. This results in the kinetic energies of about 3.25 eV for all the three fragments as already shown in figure 6.1.2.

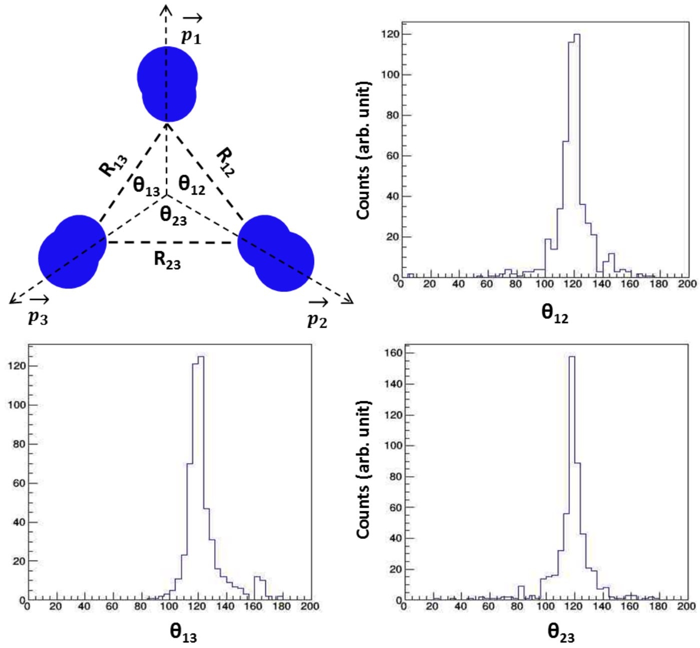

Figure 6.1.4 : *Angle between the momentum vectors of two adjacent fragments.*

The Newton diagram also shows that all van der Waals bonds dissociate simultaneously because any sequential fragmentation process would result in a circular shape of the first and third fragment momentum distribution. Considering all the three fragments as point charge, it is clear that $(N_2)_3^{3+}$ trication have a equilateral triangular shaped geometry. This interpretation of triangular geometry is fully consistent with the equal energy sharing between all the three fragments which dissociates via Coulomb explosion. To support this interpretation we have also measured the angle between the momentum vectors of any two N_2^+ fragments. In figure 6.1.4 (top) a triangular geometry for $(N_2)_3^{3+}$ has been represented where the $\vec{p}_1$, $\vec{p}_2$ and $\vec{p}_3$ are the momentum vectors of the corresponding N_2^+ fragment. The angle θ_{12} is the angle between $\vec{p}_1$ and $\vec{p}_2$ and θ_{23}, θ_{13} are defined similarly. In figure 6.1.4 (bottom) all these 3 angles have been plotted.

A sharp peak centered around 120° is observed for all the three angles in figure 6.1.4. Considering an equilateral triangle geometry, the angle between the momenta is expected to be equal to 120°. Note that due to the high symmetry of the equilateral trimer and as all the fragments have similar masses and charges, the angle $\theta_{ij}(i \neq j)$ = 120° correspond both to the initial geometry of the trimer but also to the final angle between the momentum vectors of each ion. Therefore the geometry of $(N_2)_3$ is determined to be an equilateral triangle. The widely spread distribution on the bottom of these angle peaks represents the stretching of the van der Waals bonds inside the trimer.

Bond length

Now after the analysis of KER distribution and Newton diagram, assuming an equilateral triangular geometry of $(N_2)_3$ trimer, the KER value at 9.75 eV (see figure 6.1.1) can be used to compute the equilibrium bond length $R_{(N_2)_3}$. For an equilateral triangle configuration assuming a pure Coulomb repulsion between the three fragments, one find:

$$R_{(N_2)_3} = 3 \times \frac{1}{4\pi\varepsilon_0} \cdot \frac{1}{KER}$$

.

where KER is of the 3-body dissociation channel of $(N_2)_3^{3+}$ trication. The KER peak at 9.75 eV thus correspond to a bond length $R_{(N_2)_3}$= 4.43 Å. This value is very close to the equilibrium bond length in dimer $R_{(N_2)_2}$ = 4.3 Å as measured and detailed in chapter 4.

The work done by Li using the theoretical calculations and Raman spectra predicted an equilateral triangle geometry of $(N_2)_3$ which is in agreement with our experimental results [116]. Aforementioned, there had been no experimental data on $(N_2)_3$ trimer geometry, yet rare gas trimers had been of interest lately [85,87]. In the recent studies on Argon and Neon trimers using the similar imaging techniques, it has been found that both these trimers have the equilateral triangular geometry. Moreover, the equilibrium bond length in Ar_3 and Ne_3 is close to what was measured from dimer dications of respective atoms. In our measurements as well the bond length of the N_2 dimer is similar to the bond length in N_2 trimer with a highly symmetric equilateral triangular geometry. Molecular N_2 trimer, as well as rare gas trimers result from induced dipole interaction between non polar molecules or atoms. Interestingly, it turns out that all these van der Waals clusters exhibit the similar geometrical features.

6.1.3 Dalitz plot

Another approach to confirm the previous geometrical investigation in above sections can be done using a Dalitz plot [118]. Dalitz plot is a probability density plot which allows the visualization of the reduced correlated momenta in a 3-body fragmentation. These reduced momentum are calculated using the equation below:

$$e_i = \frac{p_i^2}{\sum_{i=1,2,3} \vec{p}_i^2}$$

Using e_i the energy correlation can be represented in a 2-D Cartesian system by defining the following coordinates:
$x_D = \dfrac{e_2 - e_3}{\sqrt{3}}$ and $y_D = e_1 - \dfrac{1}{3}$. x_D and y_D are the coordinates for the Dalitz plot. Figure 6.1.5 shows the correlation between the initial geometry of the trimer and the position inside the Dalitz plot. The configuration at the coordinates (0,0) i.e. point 'O' corresponds to the case where the energy is equally distributed among three fragments. In this case all the molecular ions inside trimer are equidistant from each other and correspond to an equilateral triangle geometry. Events located on bisectors AB, CD and EF correspond to isosceles triangular geometries. These triangles can be either elongated or flattened depending on their position along the bisectors. Rest of the location inside the circle represent any other asymmetric geometries.

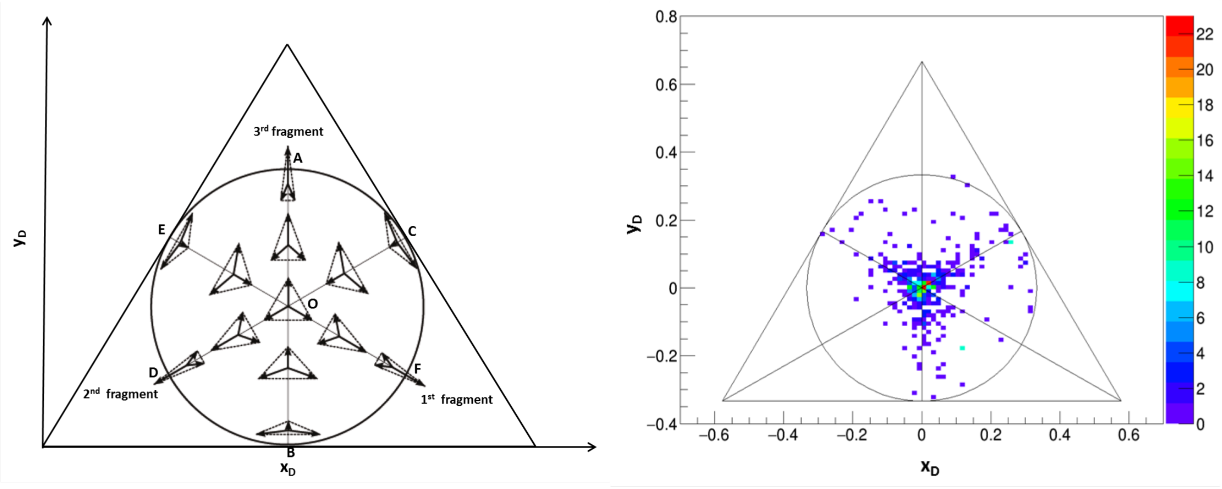

(a) **(b)**

Figure 6.1.5 : *a) Example of a Dalitz plot for representing a 3-body dissociation of symmetric system (same mass and same charge). See explanation in the text. b) Dalitz plot obtained experimentally from the 3-body dissociation of* $(N_2)_3^{3+}$.

The Dalitz plot for 3-body channel of $(N_2)_3^{3+}$ is shown in figure 6.1.5b. The highly dense red spot centered at (0,0) confirms the equilateral triangular geometry. Additionally three "wing" like distributions can be seen along the bisectors which move from the center O to the low energy part of the fragment (see OB, OC and OE in figure 6.1.5, arrow shortening along the line represent energy decrements in corresponding fragment). Such contributions of slightly flattened isosceles geometries as already been reported for rare gas Ar_3 and Ne_3 trimers [85]. They result from some specific vibrational modes of the trimer. The relative intensity of these "wings" also gives information on the floppiness of the structure and will be later compared to the case of $(CO)_3$ trimers.

6.2 3-body fragmentation of CO trimers

By contrast to N_2, the CO molecule has a small dipole moment (about 0.12 D) and we will study if this tiny dipole moment has a significant impact on the geometry of the neutral $(CO)_3$ trimer. Another question regarding the geometry CO trimer is whether the molecules are C-bonded or O-bonded. In figure 6.2.1 a planar C-bonded cyclic geometry has been deduced from IR spectroscopy in the work of Rezaei recently [117]. After investigating the homonuclear molecular trimer we update our target to heteronuclear molecular trimers i.e. $(CO)_3$. After triple ionization by 15 qkeV Ar^{9+} projectile, the fragmentation of $(CO)_3^{3+}$ trication is via, $(CO)_3^{3+} \rightarrow CO^+ + CO^+ + CO^+$ channel. The geometrical analysis in this section is similar to the one already presented for $(N_2)_3^{3+}$ trication.

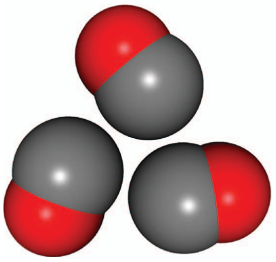

Figure 6.2.1 : *Using the hybrid potential surfaces from Vissers [14] and the IR spectra of $(CO)_3$ it is proposed by Rezaei [117] that, the CO trimer exhibits a C-bonded in plane cyclic geometry with an inter molecular separation of 4.42 Å.*

6.2.1 KER Spectrum of $(CO)_3^{3+}$

Firstly the KER spectra of this 3-body channel is presented in figure 6.2.2. The KER distribution appears to have the similar shape as of $(N_2)_3^{3+}$ but here the reaction peak for CO trimer's 3-body channel begins at around 3 eV and suddenly drops at 11 eV. The distribution is left skewed with the KER peak reaching to its most probable value at 9.2 eV. Such asymmetric KER distributions have also been observed for Ar_3 and Ne_3 trimers and may come from specific vibrational modes of the triangle. The events ranging from 11 eV to 20 eV most probably result from false coincidences not filtered out in our analysis procedure.

To investigate further, the kinetic energy shared by the three fragments is shown in figure 6.2.3. All the three spectra show a similar distribution apart from a peak very close to 0 eV in kinetic energy of second CO^+ fragment (blue part in the figure 6.2.3(center)). This contribution is likely to arise either from: a linear shape of $(CO)_3$ where the central CO molecule acquires a small amount of kinetic energy or due to false coincidences where an independent monomer cation arrive in a random coincidence window. To verify whether it is a contribution from a linear geometry or false coincidences we look into the KER distribution and add a selection on the kinetic energy of the second detected fragments (KE$_2$). It divide the events in two sets:

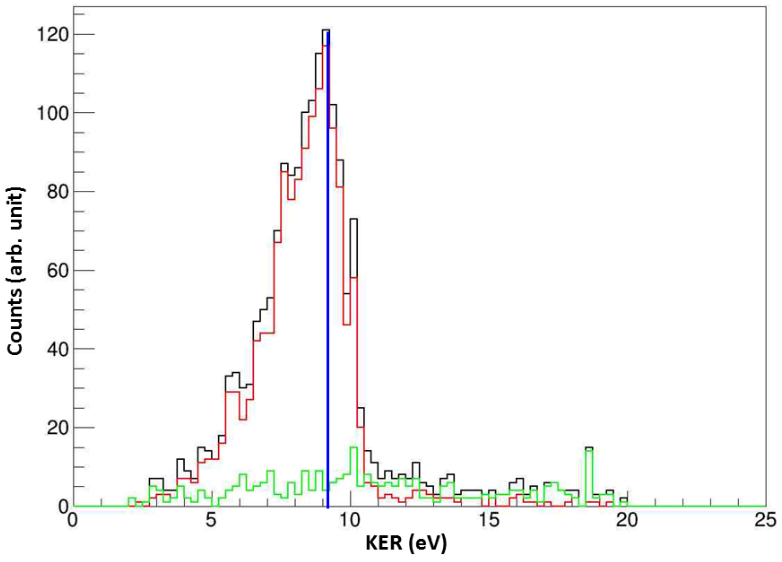

Figure 6.2.2 : *KER spectra for the* $(CO)_3^{3+}$ *3-body channel from the collision with 15 qkeV* Ar^{9+}*. The spectra in black is from all the events and spectra in red and green is with condition on kinetic energy of second* CO^+ *(see discussion in text).*

$KE_2 \geq 0.25$ eV and $KE_2 < 0.25$ eV.

The KER distributions associated to these two sets of events are plotted in red and green on figure 6.2.2. Events with $KE_2 < 0.25$ eV (green line) result in an almost flat KER distribution ranging from about 0 eV to 20 eV. Where as events with $KE_2 \geq 0.25$ eV (red line) seem to correspond to a triangular shape. Assuming a pure the Coulomb dissociation for a linear geometry of $(CO)_3$ we can calculate the expected KER associated to three exactly aligned molecules using the equation:

$$KER_{Linear} = \frac{1}{4\pi\varepsilon_0}\left(\frac{q_1q_2}{R_{12}} + \frac{q_2q_3}{R_{23}} + \frac{q_1q_3}{R_{13}}\right)$$

.
For calculation we assume the average C-bonded inter molecular distance of 4.4 Å, therefore $R_{12} = R_{23} = 4.4$ Å, $R_{13} = 2\times4.4 = 8.8$ Å and q_1, q_2, $q_3 = 1$. This gives $KER_{Linear} \simeq 8.15$ eV. Note that in such asymmetric linear geometry, the central CO^+ ion is emitted with exactly zero kinetic energy. Consequently, the central CO^+ is expected to have a time of flight equal to the central position of the TOF peak at $\frac{m}{q} = 28$. Thus, this fragment is expected to be the second to reach the detector.

While comparing with KER distribution from $KE_2 < 0.25$ eV (green line) in figure 6.2.2 there is no sign of such a peak around 8.15 eV. On the contrary this distribution is spread along the total KER spectra in black as a consistent background. Therefore we can affirm that the contribution corresponding the kinetic energy of second detected fragment below 0.25 eV are due to false coincidences and that it does not result from a linear shape.

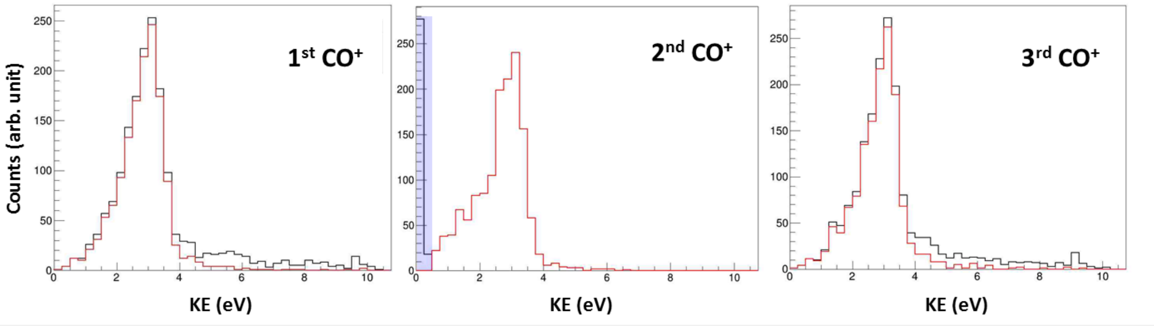

Figure 6.2.3 : *Kinetic energy spectra for all the three* CO^+ *from* $(CO)_3^{3+}$ *trication. First, second and third are assigned according to their time of arrival on the ion detector.*

In figure 6.2.3 the kinetic energy distribution in red corresponds to the events with $KE_2 \geq 0.25$ eV and only these will be used. In the kinetic energy distribution of all the three fragments the maximum is observed around 3.06 eV in all the three spectra, inferring to the symmetry in the geometry of $(CO)_3$ trimer. As we observed in the case of kinetic energy of N_2^+ fragment we again see a long tail in the low energy part and a sudden drop at the end. The equal sharing of energy between all the fragments hints a triangular geometry. Nevertheless further confirmation using Newton and Dalitz plot are done in following sections.

6.2.2 Newton diagram and Dalitz plot

The Newton diagram for the $(CO)_3^{3+}$ 3-body channel is presented below in figure 6.2.4. The plot is in the frame of reference of second CO^+ fragment and its momentum is fixed along positive x-axis at y=0. The momenta of first and third fragments are plotted in upper and lower part of y-axis respectively.

These features are very similar to what was observed in the $(N_2)_3^{3+}$ trication. Looking from the evidences of the Newton diagram and the equally distributed kinetic energy between three fragments, it is quite evident that the geometry of $(CO)_3$ is equilateral triangular. In the figure 6.2.5, the angular distributions between the momenta of any two CO^+ fragments are shown. All the three angles are centered around 120° which is also consistent with the geometry of $(CO)_3$ to be an equilateral triangle. The broadening in the bottom of each peak is from the vibrations in the weak van der Waals bond as already observed for $(N_2)_3$ trimers and Ar_3 and Ne_3 [85].

Finally, another evidence for our interpretation equilateral triangular geometry can be observed in the Dalitz plot. Figure 6.2.6 shows the Dalitz plot for $(CO)_3^{3+}$ 3-body channel. The high intensity distribution around the (0,0) coordinates of the Dalitz represent an equilateral triangular geometry of this trication.

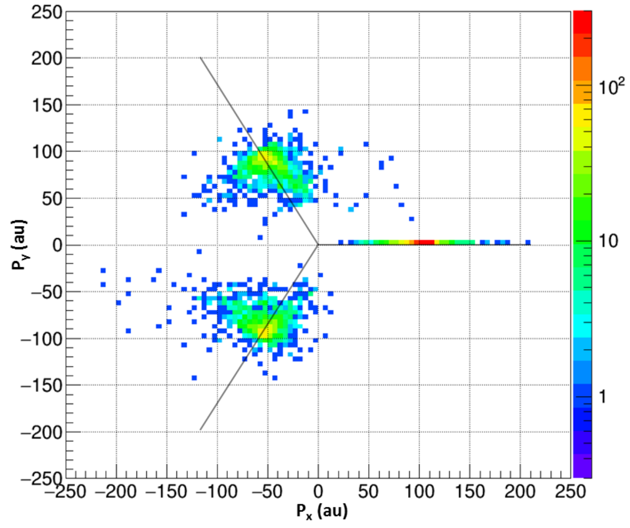

Figure 6.2.4 : *Newton diagram showing the 3-body pure coulomb dissociation of* $(CO)_3^{3+}$.

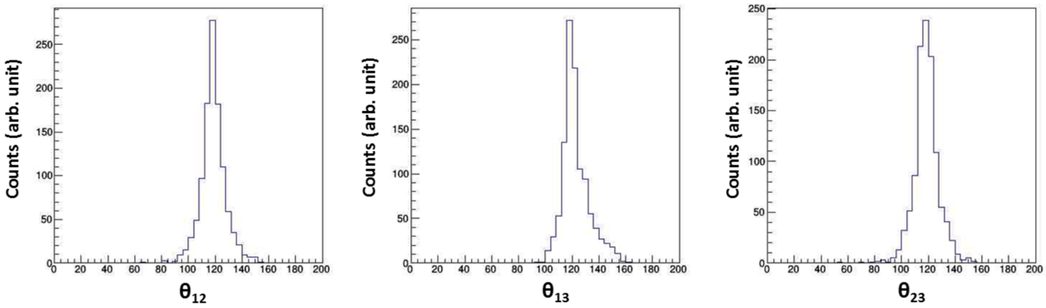

Figure 6.2.5 : *Angle between the momentum vectors of two adjacent fragments.*

Rest of the events along the bisectors show the similar behavior as in the N_2 trimer. A quantitative comparison of Dalitz from N_2 and CO suggest that the "wing" like distribution is more spread in case of CO trimer. All these events along the bisectors represents a large variety of triangular configurations available for this trimer due to the floppiness of its structure.

In the Coulomb imaging experiment from Ulrich et al about the geometry of Ne_3 and Ar_3 trimers, they observe the similar wide distributions in the case of Ne_3 in comparision to Ar_3 [85]. They found that besides the dominant equilateral triangular geometry (≈ 31.5%) there are various other triangular configuration such as isosceles (≈ 45%) and scalene(≈ 23.5%) present for Ne_3 [13]. The wide "wing" distribution in the case of $(CO)_3$ trimer seems to have similarly wide range of triangular configuration. Thus, the vibration motion inside the $(CO)_3$ trimers seems to be significantly more pronounced than the N_2 trimer.

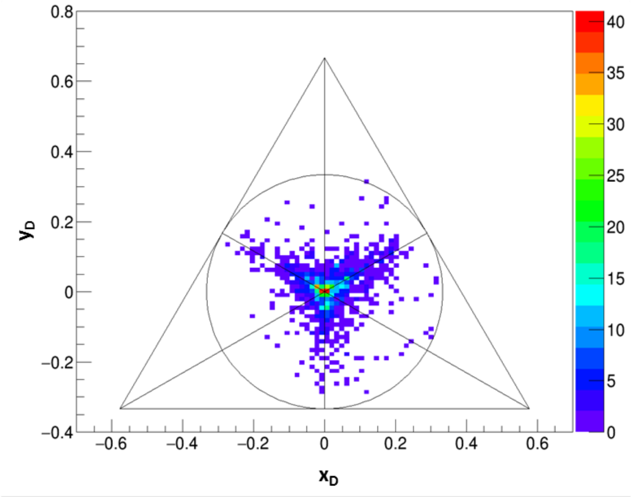

Figure 6.2.6 : *Dalitz plot obtained experimentally from the 3-body dissociation of* $(CO)_3^{3+}$

Bond length

From our analysis we are sure that the CO trimer exhibit a equilateral triangular geometry. Similar to the case of N_2 trimer we used the most probable value from the KER of the 3-body dissociation of $(CO)_3^{3+}$ to calculate the inter molecular distance ($R_{(CO)_3}$). The $R_{(CO)_3}$ is measured around 4.69 Å which is also close to our measured equilibrium bond length of CO dimer i.e. 4.52 Å. As for the N_2 clusters, we find the trimer bond length to be slightly larger (about 3%) than the dimers bond length. Alongside the structural agreement with Rezaei's work we also have the nearly equal inter molecular distances between CO dimer and trimer which agrees with the case rare gas trimers studied in Ulrich's work [85].

In previous chapter we concluded that CO dimer geometry is C-bonded. Since the value of $R_{(CO)_3}$ is close to CO dimer bond length it seems that for an equilateral triangular geometry of CO trimer may also be C-bonded. Also from the calculations and FTIR measurements done in the reference work of Rezaei et al, the CO trimers are found to have a C_{3h} symmetry for a cyclic planar geometry [117]. Our measurements and the theoretical calculations evidence that CO trimer have a C-bonded equilateral triangular geometry with an equilibrium $R_{(CO)_3}$ of 4.69 Å.

6.3 Conclusion

Using imaging technique low energy ion-induced recoil ion coincidence measurements, we perform a direct measurement of the structure of $(N_2)_3$ and $(CO)_3$ trimers thanks to their respective 3-body fragmentation channels. To the best of our knowledge, no previous research has investigated the geometry of $(N_2)_3$ and $(CO)_3$ using similar experimental technique. We can state that both of these complex systems exhibit a similar geometry. $(N_2)_3$ and $(CO)_3$ exhibit an equilateral triangular geometry with $R_{(N_2)_3}$ = 4.43 Å and $R_{(CO)_3}$ = 4.69 Å. However the bond length between the dimer and trimers of respective targets are very close to each other. This may indicate that CO trimer's geometry is most probably equilateral triangular C-bonded. The geometries obtained are in agreement with the work of Li's and Rezaei's done on (N_2) and CO trimer respectively. Although the Dalitz comparison shows that the structure of the CO trimer might be a little floppier than N_2 trimer. Such asymmetry in the emission energy of the molecular N_2^+ or CO^+ ions may also be interpreted as a signature of some indirect decay processes such as Intermolecular Coulomb Decay (ICD).

Until recently only the rare gas atomic trimers (Ne_3 and Ar_3) had been studied using imaging technique and they were both found to have a equilateral triangular geometry. The inter molecular separation in dimer and trimer are also very close to each other. As N_2 is a non polar molecule it is not surprising that it exhibit a high agreement with the findings of rare gas trimers. More surprisingly, even if CO has a small permanent dipole moment, we found that the CO trimer also exhibit a equilateral triangular geometry.

Conclusion

7

In this thesis, a detailed discussion on the main experimental results explaining the fragmentation dynamics of diatomic molecular dimers $((N_2)_2$ and $(CO)_2)$ is presented. The three dimensional geometry of dimers and trimers of both these diatomic molecules have also been investigated using Coulomb explosion imaging technique. The experiments were conducted using low energy highly charged ions in collision with diatomic molecular dimer/trimer $((N_2)_2$ and $(CO)_2)$. The low energy of the projectile favors the electron capture as the dominant process and the interaction time is shorter in comparison with the timescale of nuclear motion. Thus both sites of the cluster are considered as frozen aiding in determination of the fragmentation dynamics and geometry. Such a detailed analysis is only possible with a kinematically complete experimental setup, COLd Target Recoil Ion Momentum Spectrometer (COLTRIMS) technique in our case. The coincident detection of the position and the time of flight of all ionic fragments allow us to identify the fragmentation channels and reconstruct the three dimensional momentum vectors of each particle. A detailed analysis of the data provide details about the fragmentation dynamics and partial geometry of N_2 and CO clusters.

In both $(N_2)_2^{3+}$ and $(CO)_2^{3+}$ dimers trication, using the 3-body fragmentation channels we find two distinct dissociation pathways depending on the presence of the metastable states in the molecular dication. For the case of $(N_2)_2^{3+}$, there is essentially a synchronous direct fragmentation with both the covalent and van der Waals bonds exploding at the same time. However, in $(CO)_2^{3+}$ there is an additional delayed pathway available, known as sequential fragmentation. In sequential fragmentation the first step is the cleavage of the weak van der Waals bond via pure 2-body Coulombic dissociation followed by the cleavage of the covalent bond of the recoiling molecular dication. These pathways can be separated using the kinetic energy of the non dissociating molecule. Irrespective of the dissociation pathway it has been found that the states involved in the fragmentation of both molecular dication are weakly affected by the proximity of the non dissociating molecular cation. The presence of the non dissociating ion however contribute to a global shift of the potential energy curves of the molecular dication, establishing that the influence of neibhouring molecule is only coulombic. Additionally, the kinetic energy release corresponding to both pathways helps in distinguishing the states involved in the direct and sequential processes. Sequential dissociation is found to be due to the existence of various metastable states in the molecular dication with lifetime above 1 ps. Here we have demonstrated that molecular dimers are an effective tool to access the lifetimes of molecular ions produced in collision with low energy highly charged ions.

In another study, we used the 2 and 3-body fragmentation channels along with a Monte Carlo numerical simulations to determine the geometry of $(N_2)_2$ and $(CO)_2$ dimers. The three dimensional geometry of a diatomic molecular dimer can be represented using "internal" coordinates: intermolecular distance (R), orientation of molecules along dimer axis (θ_1 or θ_2) and the dihedral angle (ϕ) between both molecules. Using the pure coulombic 2-body fragmentation channel we found the intermolecular distances of $(N_2)_2$ and $(CO)_2$ to be 4.3 Å and 4.52 Å respectively. The orientation of the molecules (θ) inside the dimer is inferred from the 3-body channels. As θ can not be accessed directly through experimental observables therefore, we used the experimental angle ψ to deduce θ. Note that to access the orientation of molecule we only use the events associated to the direct fragmentation as the initial orientation of the dissociating molecule is lost in sequential fragmentation. We found that for $(N_2)_2$ dimers the distribution of the angle ψ is centered around 90° which, when compared to simulations, correspond to configurations with θ equals 90°. The angle ψ is equal to θ only when the dissociating molecule is perpendicular to dimer axis and both the atomic ions from the dissociating molecule have equal mass and charge. Thus, for the case of $(CO)_2$ dimer as C and O have different masses we obtained the angle ψ around 86.1° which also correspond to the configuration θ equals 90°. In both cases, the value of θ could correspond to H or X shaped geometries of the $(N_2)_2$ and $(CO)_2$ dimers. Being heteronuclear the CO dimer could be either C-bonded or O-bonded. Comparing to the intermolecular distance for these two geometries, our value $R_{(CO)_2} = 4.52$ Å would rather correspond to a C-bonded structure (proposed theoretically and by infrared measurements). Therefore, $(CO)_2$ dimer is found to have a C-bonded H shaped parallel/anti-parallel or X shaped geometry. However, for further discrimination between the H or X shaped geometry requires the measurement of the dihedral angle ϕ which is accessible only through the 4-body dissociation channel. Due to the low production cross section and the low absolute detection efficiency, our data does not contain enough statistics to investigate such 4-body channels.

In the same experiment, we also investigate the geometry of $(N_2)_3$ and $(CO)_3$ trimers, using the respective 3-body fragmentation channel in which one electron is captured on each molecular site. Here, only the van der Waals bond dissociate and only the position of the center of mass of each molecule inside the trimer is investigated. Using kinetic energy release, Newton and Dalitz diagrams, we measured that both of these complexes has a similar equilateral triangular geometry. The intermolecular bond length of $(N_2)_3$ and $(CO)_3$ are deduced to be 4.43 Å and 4.69 Å respectively. These bond lengths are observed to be close to the bond length of their respective dimers. This comparable bond length in dimer and trimer of CO may indicate that $(CO)_3$ trimer also exhibit a C-bonded equilateral triangular geometry. Finally, we found the structure of the $(CO)_3$ to be more floppier than $(N_2)_3$. Such an apparent floppiness could also result from an indirect decay process such as intermolecular coulombic decay. A similar equilateral triangular geometry has also been recently measured in rare gas clusters with intermolecular distances similar to their respective dimers. Through all the similarities between rare gas clusters and diatomic molecular clusters (non-polar and polar) we can conclude that the nature of constituents plays a minor role in the geometry of clusters.

To summarize, the experimental results obtained in this thesis and their comparison with necessary numerical simulations confirms that the Coulomb explosion imaging technique is a very efficient technique to provide answers regarding fragmentation dynamics, intermolecular distances and partial geometry of diatomic clusters. During my thesis we have updated our experimental setup by replacing the standard microchannel plate by a new funnel type microchannel plate for the recoil ion detector. The aim is to increase the absolute detection efficiency of multiple fragment channels such as 4-body channels resulting from the full dissociation of $(N_2)_2^{4+}$ and $(CO)_2^{4+}$. A detailed analysis of these 4-body channels could allow the discrimination between the H and X shapes of the dimers.

The structure of the trimers could also be more deeply investigated using the 4-body dissociation of $(N_2)_2^{4+}$ and $(CO)_2^{4+}$. In such channels, one of the molecule also breaks and the direction of emmision of these atomic ions could give additional information on the orientation of the molecule with respect to the trimer plane.

Finally, similar studies could be extended to other diatomic or triatomic molecules, specifically to very polar molecules to investigate the effect of the dipole moment on the geometry of the clusters.

Bibliography

[1] Konrad Dennerl. Charge transfer reactions. *Space Science Reviews*, 157(1-4):57–91, 2010.

[2] Ugo Amaldi and Gerhard Kraft. Recent applications of Synchrotrons in cancer therapy with Carbon Ions. *Europhysics News*, 36(4):114–118, 2005.

[3] R Janev. ATOMIC COLLISIONS IN FUSION PLASMAS. *Journal de Physique*, 50, 1989.

[4] J. E. LENNARD-JONES. COHESION. *THE PROCEEDINGS OF THE PHYSICAL SOCIETY*, 43(240):461–482, 1931.

[5] Charles A. Long, Giles Henderson, and George E. Ewing. The infrared spectrum of the (N2)2 van der waals molecule. *Chemical Physics*, 2(4):485–489, 1973.

[6] K. T. Tang and J. P. Toennies. A simple theoretical model for the van der Waals potential at intermediate distances. I. Spherically symmetric potentials. *The Journal of Chemical Physics*, 66(4):1496–1506, 1977.

[7] D. Bassi, A. Boschetti, S. Marchetti, G. Scoles, and M. Zen. State resolved rotational relaxation of CO in the free jet expansion of He-CO mixtures. *The Journal of Chemical Physics*, 74(4):2221–2227, 1981.

[8] A. Ding. Ionization dynamics of van-der-Waals clusters. *Zeitschrift fur Physik D Atoms, Molecules and Clusters*, 12(1-4):253–261, 1989.

[9] T Nagata and T Kondow. Photofragmentation of cluster ions: the visible photoabsorption spectrum of Ar2N. *Atoms, Molecules and Clusters*, 20:153–155, 1991.

[10] F. A. Gianturco, E. Buonomo, G. Delgado-Barrio, S. Miret-Artés, and P. Villarreal. Fragmentation dynamics of ionized argon clusters: an effective potential model. *Zeitschrift für Physik D Atoms, Molecules and Clusters*, 35(2):115–124, 1995.

[11] Georg Jansen. The rovibrational spectrum of the ArCO complex calculated from a semiempirically extrapolated coupled pair functional potential energy surface. *Journal of Chemical Physics*, 105(1):89–103, 1996.

[12] Charusita Chakravarty, Robert J. Hinde, David M. Leitner, and David J. Wales. Effects of three-body (Axilrod-Teller) forces on the classical and quantum behavior of rare-gas trimers. *Physical Review E - Statistical Physics, Plasmas, Fluids, and Related Interdisciplinary Topics*, 56(1):363–377, 1997.

[13] T. Gonzalez-Lezana. Comparative configurational study for He, Ne, and Ar trimers. *Journal of Chemical Physics*, 110(18):9000–9010, 1999.

[14] G. W.M. Vissers, A. Hesselmann, G. Jansen, P. E.S. Wormer, and A. Van Der Avoird. New CO-CO interaction potential tested by rovibrational calculations. *Journal of Chemical Physics*, 122(5), 2005.

[15] Richard Dawes, Xiao Gang Wang, Ahren W. Jasper, and Tucker Carrington. Nitrous oxide dimer: A new potential energy surface and rovibrational spectrum of the nonpolar isomer. *Journal of Chemical Physics*, 133(13):1–14, 2010.

[16] Olivia Borrell-Grueiro, Maykel Marquez-Mijares, Pedro Pajon-Suarez, Ramon Hernandez-Lamoneda, and Jesus Rubayo-Soneira. Fragmentation dynamics of NO-NO dimer: A quasiclassical dynamics study. *Chemical Physics Letters*, 563:20–24, 2013.

[17] Wael Iskander. *Etude des Collisions a Basse Energie entre Ions Multicharges et Dimeres de Gaz Rare*. PhD thesis, 2015.

[18] Andrew D. Powell and Richard Dawes. Calculating potential energy curves with fixed-node diffusion Monte Carlo: CO and N 2. *Journal of Chemical Physics*, 145(22), 2016.

[19] K. T. Tang and J. P. Toennies. The van der Waals potentials between all the rare gas atoms from He to Rn. *Journal of Chemical Physics*, 118(11):4976–4983, 2003.

[20] L. Gomez, B. Bussery-Honvault, T. Cauchy, M. Bartolomei, D. Cappelletti, and F. Pirani. Global fits of new intermolecular ground state potential energy surfaces for N2-H2and N2-N2van der Waals dimers. *Chemical Physics Letters*, 445(4-6):99–107, 2007.

[21] Frank Carnovale, J. Barrie Peel, and Richard G. Rothwell. Photoelectron spectroscopy of the nitrogen dimer (N ₂) ₂ and clusters (N ₂) _{<i>n</i>} : N ₂ dimer revealed as the chromophore in photoionization of condensed nitrogen. *The Journal of Chemical Physics*, 88(2):642–650, 1988.

[22] O. Couronne and Y. Ellinger. An ab initio and DFT study of (N 2) 2 dimers. *Chemical Physics Letters*, 306(1-2):71–77, 1999.

[23] Rut M. Berns and Ad van der Avoird. (N2)2 interaction potential from ab initio calculations, with application to the structure of (N2)2. *The Journal of Chemical Physics*, 72(11):6107–6116, 1980.

[24] A. Van Der Avoird, P. E.S. Wormer, and A. P.J. Jansen. An improved intermolecular potential for nitrogen. *The Journal of Chemical Physics*, 84(3):1629–1635, 1986.

[25] Akira Wada, Hideto Kanamori, and Suehiro Iwata. Ab initio MO studies of van der Waals molecule (N2)2: Potential energy surface and internal motion. *Journal of Chemical Physics*, 109(21):9434–9438, 1998.

[26] V. Aquilanti, M. Bartolomei, D. Cappelletti, E. Carmona-Novillo, and F. Pirani. The N2-N2system: An experimental potential energy surface and calculated rotovibrational levels of the molecular nitrogen dimer. *Journal of Chemical Physics*, 117(2):615–627, 2002.

[27] Mohamad H.Karimi Jafari, Ali Maghari, and Shant Shahbazian. An improved ab initio potential energy surface for N2-N 2. *Chemical Physics*, 314(1-3):249–262, 2005.

[28] Matthew D. Brookes and A. R.W. McKellar. Infrared spectrum and energy levels of the CO dimer: Evidence for two almost isoenergetic isomers. *Journal of Chemical Physics*, 111(16):7321–7328, 1999.

[29] Thomas A. Ford. The structures of some trimers of carbon monoxide-An infrared matrix isolation spectroscopic and ab initio molecular orbital study. *Spectrochimica Acta - Part A: Molecular and Biomolecular Spectroscopy*, 64(5):1151–1155, 2006.

[30] L. M. Nxumalo, E. K. Ngidi, and T. A. Ford. The structures of some dimers of carbon monoxide-an infrared matrix isolation spectroscopic and ab initio molecular orbital study. *Journal of Molecular Structure*, 786(2-3 SPEC. ISS.):168–174, 2006.

[31] Mojtaba Rezaei, S. Sheybani-Deloui, N. Moazzen-Ahmadi, K. H. Michaelian, and A. R W McKellar. CO dimer: The infrared spectrum revisited. *Journal of Physical Chemistry A*, 117(39):9612–9620, 2013.

[32] L. A. Surin, D. N. Fourzikov, F. Lewen, B. S. Dumesh, G. Winnewisser, and A. R.W. McKellar. The CO dimer: New light on a mysterious molecule. *Journal of Molecular Spectroscopy*, 222(1):93–101, 2003.

[33] G. W M Vissers, P. E S Wormer, and A. Van Der Avoird. An ab initia CO dimer interaction potential and the computation of the rovibrational spectrum of (CO)2. *Physical Chemistry Chemical Physics*, 5(21):4767–4771, 2003.

[34] Leonid A. Surin, Dmitri N. Fourzikov, Thomas F. Giesen, Stephan Schlemmer, Gisbert Winnewisser, Victor A. Panfilov, Boris S. Dumesh, Ge W M Vissers, and Ad Van Der Avoird. Higher energy states in the CO dimer: Millimeter-wave spectra and rovibrational calculations. *Journal of Physical Chemistry A*, 111(49):12238–12247, 2007.

[35] Richard Dawes, Xiao Gang Wang, and Tucker Carrington. CO dimer: New potential energy surface and rovibrational calculations. *Journal of Physical Chemistry A*, 117(32):7612–7630, 2013.

[36] F. Penent, R. I. Hall, R. Panajotović, J. H.D. Eland, G. Chaplier, and P. Lablanquie. New method for the study of dissociation dynamics of state-selected doubly charged ions: Application to CO2+. *Physical Review Letters*, 81(17):3619–3622, 1998.

[37] Th Weber, O Jagutzki, M Hattass, A Staudte, A Nauert, L Schmidt, M H Prior, A L Landers, A Brauning-Demian, H Brauning, C L Cocke, T Osipov, I Ali, R Diez Muino, D Rolles, F J Garcia de Abajo, C S Fadley, M A Van Hove, A Cassimi, H Schmidt-Bocking, and R Dorner. K-shell photoionization of CO and N 2 : is there a link between the photoelectron angular distribution and the molecular decay dynamics? *Journal of Physics B: Atomic, Molecular and Optical Physics*, 34(18):3669–3678, 2001.

[38] Eckart Rühl. Core level excitation, ionization, relaxation, and fragmentation of free clusters. *International Journal of Mass Spectrometry*, 229(3):117–142, 2003.

[39] M. Lundqvist, P. Baltzer, D. Edvardsson, L. Karlsson, and B. Wannberg. Novel time of flight instrument for Doppler free kinetic energy release spectroscopy. *Physical Review Letters*, 75(6):1058–1061, 1995.

[40] D. Mathur, L. H. Andersen, P. Hvelplund, D. Kella, and C. P. Safvan. Long-lived, doubly charged diatomic and triatomic molecular ions. *Journal of Physics B: Atomic, Molecular and Optical Physics*, 28(15):3415–3426, 1995.

[41] M. Lundqvist, D. Edvardsson, P. Baltzer, and B. Wannberg. Doppler-free kinetic energy release spectrum of N 2. *Journal of Physics B: Atomic, Molecular and Optical Physics*, 29(8):1489–1499, 1996.

[42] A. Pandey, B. Bapat, and K. R. Shamasundar. Charge symmetric dissociation of doubly ionized N ₂ and CO molecules. *The Journal of Chemical Physics*, 140(3):034319, 2014.

[43] A. Pandey, P. Kumar, S. B. Banerjee, K. P. Subramanian, and B. Bapat. Electron-impact dissociative double ionization of N2 and CO: Dependence of transition probability on impact energy. *Physical Review A*, 93(4):1–6, 2016.

[44] S. De, M. Magrakvelidze, I. A. Bocharova, D. Ray, W. Cao, I. Znakovskaya, H. Li, Z. Wang, G. Laurent, U. Thumm, M. F. Kling, I. V. Litvinyuk, I. Ben-Itzhak, and C. L. Cocke. Following dynamic nuclear wave packets in N2,O2, and CO with few-cycle infrared pulses. *Physical Review A - Atomic, Molecular, and Optical Physics*, 84(4):1–13, 2011.

[45] X. Gong, M. Kunitski, L. Ph H. Schmidt, T. Jahnke, A. Czasch, R. Dörner, and J. Wu. Simultaneous probing of geometry and electronic orbital of ArCO by Coulomb-explosion imaging and angle-dependent tunneling rates. *Physical Review A - Atomic, Molecular, and Optical Physics*, 88(1):1–5, 2013.

[46] Xiaoyan Ding, M. Haertelt, S. Schlauderer, M. S. Schuurman, A. Yu Naumov, D. M. Villeneuve, A. R.W. McKellar, P. B. Corkum, and A. Staudte. Ultrafast Dissociation of Metastable CO2 in a Dimer. *Physical Review Letters*, 118(15):1–5, 2017.

[47] E. P. Kanter, P. J. Cooney, D. S. Gemmell, K. O. Groeneveld, W. J. Pietsch, A. J. Ratkowski, Z. Vager, and B. J. Zabransky. Role of excited electronic states in the interactions of fast (MeV) molecular ions with solids and gases. *Physical Review A*, 20(3):834–854, 1979.

[48] A. Cassimi, S. Duponchel, X. Flechard, P. Jardin, P. Sortais, D. Hennecart, and R. E. Olson. State-selective electron capture in low velocity multiply charged ion, helium collisions. *Physical Review Letters*, 76(20):3679–3682, 1996.

[49] H. O. Folkerts, T. Schlathölter, R. Hoekstra, and R. Morgenstern. Dissociation of CO induced by He2+ ions: II. Dissociation pathways and states. *Journal of Physics B: Atomic, Molecular and Optical Physics*, 30(24):5849–5860, 1997.

[50] L. Adoui, C. Caraby, A. Cassimi, D. Lelièvre, J. P. Grandin, and A. Dubois. Fast ion-induced CO molecule fragmentation in the strong interaction regime. *Journal of Physics B: Atomic, Molecular and Optical Physics*, 32(3):631–647, 1999.

[51] M. Tarisien, L. Adoui, F. Frémont, D. Lelièvre, L. Guillaume, J. Y. Chesnel, H. Zhang, A. Dubois, D. Mathur, Sanjay Kumar, M. Krishnamurthy, and A. Cassimi. Ion-induced molecular fragmentation: Beyond the Coulomb explosion picture. *Journal of Physics B: Atomic, Molecular and Optical Physics*, 33(1):11–20, 2000.

[52] M. Ehrich, U. Werner, H. O. Lutz, T. Kaneyasu, K. Ishii, K. Okuno, and U. Saalmann. Simultaneous charge polarization and fragmentation of [Formula Presented] molecules in slow keV collisions with [Formula Presented] ions. *Physical Review A - Atomic, Molecular, and Optical Physics*, 65(3):4, 2002.

[53] J. Matsumoto, A. Leredde, X. Flechard, K. Hayakawa, H. Shiromaru, J. Rangama, C. L. Zhou, S. Guillous, D. Hennecart, T. Muranaka, A. Mery, B. Gervais, and A. Cassimi. Asymmetry in multiple-electron capture revealed by radiative charge transfer in ar dimers. *Physical Review Letters*, 105(26):1–4, 2010.

[54] J. Matsumoto, A. Leredde, X. Flechard, K. Hayakawa, H. Shiromaru, J. Rangama, C. L. Zhou, S. Guillous, D. Hennecart, T. Muranaka, A. Mery, B. Gervais, and A. Cassimi.

Multiple-ionization and dissociation dynamics of a rare gas dimer induced by highly charged ion impact. *Physica Scripta T*, T144:0–5, 2011.

[55] W. Iskandar, J. Matsumoto, A. Leredde, X. Flechard, B. Gervais, S. Guillous, D. Hennecart, A. Mery, J. Rangama, C. L. Zhou, H. Shiromaru, and A. Cassimi. Atomic site-sensitive processes in low energy ion-dimer collisions. *Physical Review Letters*, 113(14):1–5, 2014.

[56] W. Iskandar, J. Matsumoto, A. Leredde, X. Fléchard, B. Gervais, S. Guillous, D. Hennecart, A. Méry, J. Rangama, C. L. Zhou, H. Shiromaru, and A. Cassimi. Interatomic coulombic decay as a new source of low energy electrons in slow ion-dimer collisions. *Physical Review Letters*, 114(3):1–5, 2015.

[57] C. P. Safvan and Jyoti Rajput. Orientation and alignment effects in ion-induced fragmentation of isolated water molecules. *Journal of Physics: Conference Series*, 635(3), 2015.

[58] Anthony C.K. Leung and Tom Kirchner. Radiative-emission analysis in charge-exchange collisions of O6+ with argon, water, and methane. *Physical Review A*, 95(4):1–10, 2017.

[59] X. Flechard, L. Adoui, G. Ban, P. Boduch, A. Cassimi, J. Y. Chesnel, D. Durand, F. Fremont, S. Guillous, J. P. Grandin, D. Hennecart, E. Jacquet, P. Jardin, E. Lamour, E. Lienard, D. Lelievre, L. Maunoury, A. Mery, O. Naviliat-Cuncic, C. Prigent, J. M. Ramillon, J. Rangama, J. P. Rozet, S. Steydli, M. Trassinelli, and D. Vernhet. Primary processes: From atoms to diatomic molecules and clusters. *Journal of Physics: Conference Series*, 629(1), 2015.

[60] F. Legare, Kevin F. Lee, I. V. Litvinyuk, P. W. Dooley, S. S. Wesolowski, P. R. Bunker, P. Dombi, F. Krausz, A. D. Bandrauk, D. M. Villeneuve, and P. B. Corkum. Laser Coulomb explosion imaging of small molecules. *Physical Review A*, 71(013415), 2005.

[61] J. Matsumoto, H. Tezuka, and H. Shiromaru. Charge-sharing in fragmentation of nitrogen molecules in collision with highly charged ions. *Journal of Physics: Conference Series*, 583:1–5, 2015.

[62] Hiroshi Ryufuku, Ken Sasaki, and Tsutomu Watanabe. Oscillatory behavior of charge transfer cross sections as a function of the charge of projectiles in low-energy collisions. *Physical Review A*, 21(3):745–750, 1980.

[63] R. Mann, F. Folkmann, and H. F. Beyer. Selective electron capture into highly stripped Ne and N target atoms after heavy-ion impact. *Journal of Physics B: Atomic and Molecular Physics*, 14(7):1161–1181, 1981.

[64] A. Barany, G. Astner, H. Cederquist, H. Danared, S. Huldt, P. Hvelplund, A. Johnson, H. Knudsen, L. Liljeby, and K. G. Rensfelt. Absolute cross sections for multi-electron processes in low energy Ar q+ -Ar collisions: Comparison with theory. *Nuclear Inst. and Methods in Physics Research, B*, 9(4):397–399, 1985.

[65] A. Niehaus. A classical model for multiple-electron capture in slow collisions of highly charged ions with atoms. *Journal of Physics B: Atomic and Molecular Physics*, 19(18):2925–2937, 1986.

[66] Tomoko Ohyama-Yamaguchi and Atsushi Ichimura. Analysis of charge-asymmetric Coulomb explosion of N2 molecules with slow Kr8+ ions. *Journal of Physics: Conference Series*, 163, 2009.

[67] W. Iskandar, X. Flechard, J. Matsumoto, A. Leredde, S. Guillous, D. Hennecart, J. Rangama, A. Mery, B. Gervais, H. Shiromaru, and A. Cassimi. Coulomb over-the-barrier Monte Carlo simulation to probe ion-dimer collision dynamics. *Physical Review A*, 98(1):14–17, 2018.

[68] D. F. Ye, J. Chen, and J. Liu. Classical trajectory perspective on double-ionization dynamics of diatomic molecules irradiated by ultrashort intense laser pulses. *Physical Review A - Atomic, Molecular, and Optical Physics*, 77(1):1–10, 2008.

[69] Qiying Song, Peifen Lu, Xiaochun Gong, Qinying Ji, Kang Lin, Wenbin Zhang, Junyang Ma, Heping Zeng, and Jian Wu. Dissociative double ionization of CO in orthogonal two-color laser fields. *Physical Review A*, 95(1):1–5, 2017.

[70] Felicja Mrugala. A computational study of metastable states of CO2+. *Journal of Chemical Physics*, 129(6):1–18, 2008.

[71] Sharad Medhe. Mass Spectrometry: Detectors Review. *Mass Spectrometry: Detectors Review Article in Annual Review of Chemical and Biomolecular Engineering*, 3(4):51–58, 2018.

[72] Donald S Gemmell. The "Coulomb-Explosion" Technique for determining geometrical structures of molecular ions. *Synthesis*, 191:425–431, 1981.

[73] Z. Vager, E. P. Kanter, G. Both, P. J. Cooney, A. Faibis, W. Koenig, B. J. Zabransky, and D. Zajfman. Direct determination of the stereochemical structure of CH4+. *Physical Review Letters*, 57(22):2793–2795, 1986.

[74] R. Dorner, J Ullrich, and R Moshammer. Cold Target Recoil Ion Momentum Spectroscopy a momentum microscop toview atomic collision dynamics. *Elsevier Physics Reports*, 330, 2000.

[75] J. Ullrich, R. Moshammer, A. Dorn, R. Dorner, L. Ph H. Schmidt, and H. Schmidt-Böcking. Recoil-ion and electron momentum spectroscopy: Reaction-microscopes. *Reports on Progress in Physics*, 66(9):1463–1545, 2003.

[76] J. Ulrich and H. Schimdt-Bocking. TIME-OF-FLIGHT SPECTROMETER FOR THE DETERMINATION OF MICRORADIAN PROJECTILE SCATTERING ANGLES IN ATOMIC COLLISIONS J. *Physics letters A*, 125(4):193–196, 1987.

[77] R. Ali, V. Frohne, C. L. Cocke, M. Stockli, S. Cheng, and M. L. A. Raphaelian. Q-Value Measurements in Charge-Transfer Collisions of Highly Charged Ions with Atoms by Recoil Longitudinal Momentum Spectroscopy R. *Physical Review Letters*, 69(17):2491–2495, 1992.

[78] Pascal Jardin. *Etude des mecanismes elementaires de transfert d'energie au cours d'une collision entre un ion lourd rapide multi-charge et un atom neutre*. PhD thesis, 1995.

[79] Akitaka Matsuda, Eiji J. Takahashi, and Akiyoshi Hishikawa. Dalitz plot analysis of Coulomb exploding O3 in ultrashort intense laser fields. *Journal of Chemical Physics*, 127(11):1–7, 2007.

[80] N. Neumann, D. Hant, L. Ph H Schmidt, J. Titze, T. Jahnke, A. Czasch, M. S. Schöffler, K. Kreidi, O. Jagutzki, H. Schmidt-Böcking, and R. Dörner. Fragmentation dynamics of CO23+ investigated by multiple electron capture in collisions with slow highly charged ions. *Physical Review Letters*, 104(10):1–4, 2010.

[81] Jyoti Rajput, T. Severt, Ben Berry, Bethany Jochim, Peyman Feizollah, Balram Kaderiya, M. Zohrabi, U. Ablikim, Farzaneh Ziaee, Kanaka P. Raju, D. Rolles, A. Rudenko, K. D. Carnes, B. D. Esry, and I. Ben-Itzhak. Native Frames: Disentangling Sequential from Concerted Three-Body Fragmentation. *Physical Review Letters*, 120(10):103001, 2018.

[82] Cong Wu, Chengyin Wu, Di Song, Hongmei Su, Yudong Yang, Zhifeng Wu, Xianrong Liu, Hong Liu, Min Li, Yongkai Deng, Yunquan Liu, Liang You Peng, Hongbing Jiang, and Qihuang Gong. Nonsequential and sequential fragmentation of CO23+ in intense laser fields. *Physical Review Letters*, 110(10):1–5, 2013.

[83] Mehdi Terisien. *Dynamique de la fragmentation de molecules simples induite par impact d'ion multicharge*. PhD thesis, University de Caen, 2003.

[84] Tomoko Muranaka. *Dynamique de la fragmentation de molecules tri-atomiques: contribution de la geometrie*. PhD thesis, 2007.

[85] B. Ulrich, A. Vredenborg, A. Malakzadeh, L. Ph H. Schmidt, T. Havermeier, M. Meckel, K. Cole, M. Smolarski, Z. Chang, T. Jahnke, and R. Dörner. Imaging of the structure

of the argon and neon dimer, trimer, and tetramer. *Journal of Physical Chemistry A*, 115(25):6936–6941, 2011.

[86] Xiguo Xie, Cong Wu, Yirong Liu, Wei Huang, Yongkai Deng, Yunquan Liu, Qihuang Gong, and Chengyin Wu. Identifying isomers of carbon-dioxide clusters by laser-driven Coulomb explosion. *Physical Review A - Atomic, Molecular, and Optical Physics*, 90(3):1–5, 2014.

[87] Xiguo Xie, Chengyin Wu, Ying Yuan, Xin Zheng Li, Cong Wu, Peng Wang, Yongkai Deng, Yunquan Liu, and Qihuang Gong. Structural determination of argon trimer. *AIP Advances*, 5(9), 2015.

[88] Enliang Wang, Xu Shan, Zhenjie Shen, Maomao Gong, Yaguo Tang, Yi Pan, Kai Chung Lau, and Xiangjun Chen. Pathways for nonsequential and sequential fragmentation of CO23+ investigated by electron collision. *Physical Review A - Atomic, Molecular, and Optical Physics*, 91(5):1–5, 2015.

[89] Chengyin Wu, Cong Wu, Di Song, Hongmei Su, Xiguo Xie, Min Li, Yongkai Deng, Yunquan Liu, and Qihuang Gong. Communication: Determining the structure of the N2Ar van der Waals complex with laser-based channel-selected Coulomb explosion. *The Journal of chemical physics*, 140(14):141101, 2014.

[90] G. W. Fraser. The ion detection efficiency of microchannel plates (MCPs). *International Journal of Mass Spectrometry*, 215(1-3):13–30, 2002.

[91] R. Campargue. NOZZLE BEAM TECHNIQUE. *International conference on molecular beams*, (April):18–22, 1977.

[92] R. Campargue. Progress in overexpanded supersonic jets and skimmed molecular beams in free-jet zones of silence. *Journal of Physical Chemistry*, 88(20):4466–4474, 1984.

[93] P. Raghuraman and P. Davidovits. Velocity slip of gas mixtures in free jet expansions. *Physics of Fluids*, 21(9):1485, 1978.

[94] P. K. Sharma, E. L. Knuth, and W. S. Young. Species enrichment due to Mach-number focusing in a molecular-beam mass-spectrometer sampling system. *The Journal of Chemical Physics*, 64(11):4345–4351, 1976.

[95] O. F. Hagena and W. Obert. Cluster formation in expanding supersonic jets: effect of pressure, temperature, nozzle size, and test gas. *The Journal of Chemical Physics*, 56(5):1793–1802, 1972.

[96] Kailash C. Gupta, Nandan Jha, Paramita Deb, D. R. Mishra, and Jayant K. Fuloria. Determining the mean size and density of clusters, formed in super sonic jets, by Rayleigh

scattering and Mach-Zehnder interferometer. *Journal of Applied Physics*, 118(11):1–11, 2015.

[97] Eldon L. Knuth. Dimer-formation rate coefficients from measurements of terminal dimer concentrations in free-jet expansions. *The Journal of Chemical Physics*, 66(8):3515–3525, 1977.

[98] A. A. Ilyukhin, R. L. Pykhov, V. V. Smirnov, and G. Marowsky. Rotational temperature behaviour in supersonic jet expansions of molecular nitrogen. *Applied Physics B Photophysics and Laser Chemistry*, 51(3):192–196, 1990.

[99] W. Kamke, J. de Vries, J. Krauss, E. Kaiser, B. Kamke, and I. V. Hertel. Photoionisation studies of homogeneous argon and krypton clusters using TPEPICO. *Zeitschrift fur Physik D Atoms, Molecules and Clusters*, 14(4):339–351, 1989.

[100] J Krauss, J De Vries, H Steger, E Kaiser, B Kamke, and W Kamke. Tpepico studies near ionization thresold of argon and kripton clusters. *Zeitschrift fur Physik D Atoms, Molecules and Clusters*, 20:29–32, 1991.

[101] M. Förstel, T. Arion, and U. Hergenhahn. Reprint of measuring the efficiency of interatomic coulombic decay in Ne clusters. *Journal of Electron Spectroscopy and Related Phenomena*, 196:54–57, 2014.

[102] M. Förstel, T. Arion, and U. Hergenhahn. Reprint of measuring the efficiency of interatomic coulombic decay in Ne clusters. *Journal of Electron Spectroscopy and Related Phenomena*, 196:54–57, 2014.

[103] J. M. Ramillon, G. Gaubert, L. Guillaume, L. Maunoury, R. Vicquelin, R. Leroy, The GANIL Ion Production Group, T. Been, V. Mouton, A. Lepoutre, D. Leclerc, and J. Y. Pacquet. LIMBE: A new facility for low energy beams. *Review of Scientific Instruments*, 73(2):561–563, 2002.

[104] Hamamatsu Photonics. MCP (Microchannel plate) and MCP Assembly. *Hamamatsu catalogue*, pages 1–20, 2016.

[105] Roentdek. MCP delay line detector manual11.0.1703.1. *Report*, 11.0.1703.1, 2015.

[106] Shiro Matoba, Ryota Takahashi, Chihiro Io, Tetsuo Koizumi, and Haruo Shiromaru. Absolute detection efficiency of a high-sensitivity microchannel plate with tapered pores. *Japanese Journal of Applied Physics*, 50(11 PART 1), 2011.

[107] S. Matoba, G. Ishikawa, S. Moriya, K. Takahashi, T. Koizumi, and H. Shiromaru. Note: Absolute detection efficiency of a tapered microchannel plate for Ne+ions. *Review of Scientific Instruments*, 85(8):14–17, 2014.

[108] M. Kunitski, K. Fehre, T. Jahnke, O. Jagutzki, J. Gatzke, L. Ph. H. Schmidt, D. Trojanowskaja, J. Stohner, M. S. Schöffler, A. Czasch, S. Zeller, R. Berger, R. Dörner, and F. Trinter. Absolute ion detection efficiencies of microchannel plates and funnel microchannel plates for multi-coincidence detection. *Review of Scientific Instruments*, 89(4):045112, 2018.

[109] LPC Caen. Fast acquisition system for nuclear research. `http://faster.in2p3.fr/`.

[110] A. Mery, A. N. Agnihotri, J. Douady, X. Flechard, B. Gervais, S. Guillous, W. Iskandar, E. Jacquet, J. Matsumoto, J. Rangama, F. Ropars, C. P. Safvan, H. Shiromaru, D. Zanuttini, and A. Cassimi. Role of a Neighbor Ion in the Fragmentation Dynamics of Covalent Molecules. *Physical Review Letters*, 118(23):1–5, 2017.

[111] F. Trinter, M. S. Schöffler, H. K. Kim, F. P. Sturm, K. Cole, N. Neumann, A. Vredenborg, J. Williams, I. Bocharova, R. Guillemin, M. Simon, A. Belkacem, A. L. Landers, Th Weber, H. Schmidt-Böcking, R. Dörner, and T. Jahnke. Resonant Auger decay driving intermolecular Coulombic decay in molecular dimers. *Nature*, 505(7485):664–666, 2014.

[112] Andrew W. Meredith and Anthony J. Stone. An ab Initio and Diffusion Monte Carlo Study of the Potential Energy Surface of the CO Dimer . *The Journal of Physical Chemistry A*, 102(2):434–445, 2002.

[113] Daniel A. Roth, Leonid A. Surin, Boris S. Dumesh, Gisbert Winnewisser, and Igor Pak. The CO dimer millimeter wave spectrum: Detection of tunneling transitions. *The Journal of Chemical Physics*, 113(8):3034–3038, 2002.

[114] Kaley A. Walker and A. R.W. McKellar. Millimeter-wave spectra of the CO dimer: Observation and assignment of 20 new transitions. *Journal of Molecular Spectroscopy*, 208(2):209–212, 2001.

[115] Mojtaba Rezaei, Sahar Sheybani-deloui, Kirk H Michaelian, Andrew Robert W Mckellar, Natural Resources Canada, Oil Patch Drive, and A Suite. CO Dimer : The Infrared Spectrum Revisited CO Dimer : The Infrared Spectrum Revisited. 2013.

[116] Qianshu Li, Penggang Yin, Yongdong Liu, Au Chin Tang, Hongxing Zhang, and Yanbo Sun. Ab initio and DFT studies of the weakly bound nitrogen molecule complexes (N2)n (n=3-6). *Chemical Physics Letters*, 375(5-6):470–476, 2003.

[117] Mojtaba Rezaei, S. Sheybani-Deloui, N. Moazzen-Ahmadi, K. H. Michaelian, and A. R W McKellar. Communication: Spectroscopic evidence for a planar cyclic CO trimer. *Journal of Chemical Physics*, 138(7), 2013.

[118] R. H. Dalitz. On the Analysis of r-Meson Data and the Nature of the T-Meson. *The London, Edinburgh, and Dublin Philosophical Magazine and Journal of Science*, 44(357):1068–1080, 1953.

[119] W. C. Wiley and I. H. McLaren. Time-of-flight mass spectrometer with improved resolution. *Review of Scientific Instruments*, 26(12):1150–1157, 1955.

[120] Cathy Fontbonne. *Acquisition multiparametrique de signaux de decroissance radioactive pour la correction des defauts instrumentaux : application a la mesure de la duree de vie du 19Ne*. PhD thesis, 2017.

[121] Cathy Fontbonne. *FASTER-QDC-TDC MODULE*. Number May. 2013.

Annexes